# Mechanical behavior of nanotwinned materials – experimental and computational approaches

by

**Hakan Yavas**

A dissertation submitted to the graduate faculty

in partial fulfillment of the requirements for the degree of

DOCTOR OF PHILOSOPHY

Major: Materials Science and Engineering

Program of Study Committee:
Richard A. LeSar, Major Professor
Krishna Rajan
Alexander H. King
Duane D. Johnson
Ashraf Bastawros

Iowa State University

Ames, Iowa

2016

*To my family…*

*Doktora tezimi aileme ithaf ediyorum…*

# TABLE OF CONTENTS

# ACKNOWLEDGMENTS

I am deeply thankful to my supervisor, Prof. Richard LeSar, for his guidance, patience, friendship and support throughout my research. His intuitive approaches to dealing with scientific challenges have inspired me. His vision, drive and work ethic have truly been inspirational. Overall, working with him has always made me felt privileged. I would also like to express my sincere gratitude to my co-supervisor, Prof. Krishna Rajan, for his comments and suggestions during my Ph.D. studies. I also thank to my committee members, Prof. Alexander King, Prof. Duane Johnson and Prof. Ashraf Bastawros, for their helpful comments and discussions.

I want to thank my collaborators from the Ames Laboratory, Prof. Peter Collins, Dr. Ryan Ott, Dr. Valery Borovikov, Dr. Mikhail Mendelev, Dr. Matthew Kramer and Matthew Besser for their direct contributions to this study.

I also would like to thank Dr. Irene Beyerlein and Dr. Abigail Hunter for their collaboration. I will never forget the experiences they provided me during my time in Los Alamos.

All my group members, John, Perry and Matt, deserve many thanks for their helpful discussions, comments and friendship. I would like to thank Onur R. Bingol for his help and scientific discussions on various computational problems related to twin boundaries.

I sincerely thank to Simge Cinar for her unfailing support, love, encouragement and patience.

Finally, I wish to express my appreciation to my family, Mehmet, Seküre, Elif and Serkan Yavas, for their moral support and encouragement. No words can actually express my deepest gratitude to my family members. Without their love, understanding and sacrifice, I would never have completed this study.

This work was supported by the U.S. Department of Energy (DOE), Office of Science, Basic Energy Sciences, Materials Science and Engineering Division. The research was performed at the Ames Laboratory, which is operated for the U.S. DOE by Iowa State University under contract # DE-AC02-07CH11358.

# ABSTRACT

Nanotwinned materials exhibit high strength combined with excellent thermal stability, making them potentially attractive for numerous applications. When deposited on cold substrates at high rates, for example, silver films can be prepared with a high-density of growth twins with an average twin boundary spacing of less than 10 nm. These films show a very strong {111} texture, with the twin boundaries being perpendicular to the growth direction. The origins of superior mechanical and thermal properties of nanotwinned materials, however, are not yet fully understood and need further improvements.

The aim of this dissertation is to develop a connected experimental and theoretical/modeling study to elucidate the fundamental mechanisms that control the strength and stability of nanotwinned materials. To that end, we employed in-situ high-temperature nanoindentation to examine the mechanical behavior of nanotwinned materials. The hardness and strain rate were determined as a function of temperature, from which activation energies, activation volumes and strain rate sensitivities –which are fingerprints of dominant deformation mechanism- were determined. Furthermore, to better understand the physical phenomena that leads to their high strength, we have used the phase field dislocation dynamics (PFDD) model to study the effect of twin boundary spacing, grain size, applied stress on the stress driven emission and interaction of leading/trailing partial dislocations from grain boundary. Understanding both the mechanical properties of nanotwinned materials as well as how to control their structures will allow us to design better materials with desired properties.

# CHAPTER I. INTRODUCTION

Polycrystalline metals with a grain size of less than 100 nanometers (nm), i.e., nanocrystalline (nc) metals, have been one of the driving research area in materials science community since late 1970's due to their superior mechanical properties: high yield points, hardness, improved wear, fatigue and friction resistance. These unique properties of nc metals, however, comes with the cost, that is poor thermal/microstructural stability and very limited ductility. For instance, grain coarsening (loss of nc structure) has been shown to occur even at room temperature [1], and ductility of nc metals can be significantly lower than their coarse-grained counterparts [2]. The microstructural instability of nc metals can lead to catastrophic failure during service and has prevented their use in critical applications. To overcome these limitations and the need for materials with high mechanical/thermal performance, researchers have proposed several approaches: bimodal grain size distribution [3,4], second-phase particle hardening [5–7][8–10] and introducing twins with nanoscale spacing in grains [8–10]. Among these approaches nanotwinned (NT) metals stand out with their superior mechanical properties and thermal stability. Recent studies have revealed that introducing high density of nanotwins into the pure face-centered cubic (fcc) metals can lead to superior strength – much greater than nc metals- and hardness while maintaining thermal stability [11] and ductility [10].

Twinning phenomena have been studied both experimentally and theoretically in the past, particularly in regards to deformation twins and annealing twins. Formation of

twins via bottom-up approaches, growth twins, however, is relatively new concepts with their unique formation kinetics. This type of material class can be fabricated easily through high-rate deposition techniques on cooled substrates, i.e. magnetron sputtering. Growth twins are very sensitive to deposition parameters thus one can easily manipulate microstructural properties of NT metals by tuning the processing variables. A very recent study has shown that deposition power could easily tune twin spacing, twin orientation and grain size and compared these properties with a simple descriptive metric: "texture parameter" [12]. This study demonstrated an efficient approach to study NT metals by a systematic way and allowed further studies by texture parameter and gave a brief description of controlling twin boundary orientations or twin density by processing conditions with their mechanical property correlations. The vast majority of the related literature has focused on Cu, while only a few limited studies looked at other metals. Therefore, this gap in the literature has left many questions still unanswered. For example, can the same level of strengthening be observed for different systems? Is there any difference in the deformation mechanisms under applied stress conditions for various NT metals? What are the optimum twin boundary density values? The current work served to address some of the above questions by deeply examining mechanical responses of various metals by a systematic approach.

Mechanical properties of NT metals have mostly been obtained using small scale testing techniques, such as nanoindentation. Nanoindentation has been a powerful method to study plasticity in small volumes for few decades [13–17]. The most common use of nanoindentation has been to measure mechanical properties, such as hardness, elastic modulus and creep compliance, from indentation hysteresis. The high resolution of load-

depth data makes nanoindentation suitable for further deformation analysis. Also, many studies have been mostly focused only on room temperature operations. Some instrumental upgrades, however, could make nanoindentation studies suitable up to 750˚C. This fascinating *in-situ* high-temperature testing capability of nanoindentation has come with a lot of challenges such as thermal drift, instrumental noise, etc., especially for thin films, has required additional procedural improvements for sensitive samples, i.e., NT metals [18–23]. This study has generated additional knowledge and testing protocol on high-temperature analyses with nanoindentation. The high-temperature testing and high sensitivity measurements of nanoindentation – nano-Newton (nN) level force readings combined with nano-meter (nm) level depth measurements- has opened new focus area: *calculation of apparent activation energy*. The very sensitive strain rate, force and depth measurements have revealed material properties at elevated temperatures that cannot be revealed at room temperature measurements [24]. Calculating activation energies at different temperatures could give insights on defining plausible temperature-dependent deformation mechanisms. From the point of interest of NT metals, none of the studies have been reported their *in-situ* high-temperature mechanical properties. Another focus area of this study was measuring mechanical properties and activation energies of NT metals as a function of texture parameter and temperature, then, predicting plausible deformation mechanisms at each temperature regime. That approach would allow us to define the critical temperature regimes where deformation mechanisms shift and to make direct measurements of the thermal stability of NT metals.

Nanoindentation load-displacement hysteresis demonstrated cumulative description of deformation mechanisms at different temperatures. To isolate what specific

mechanisms are responsible for the superior properties of NT metals, few computational studies have been done. In these studies, it has been found that at nanoscale (tens of nm) partial mediated slip [25,26], dislocation (partial or full) reactions at grain boundaries and/twin boundaries and concomitantly stacking faults become more prevalent [27–30]. Furthermore, molecular dynamics (MD) simulations proposed that not only intrinsic stacking fault energy, but also unstable stacking fault energy could favor partial dislocation nucleation and propagation at these length scales. Therefore, to study NT metals, a proposed model should account for these effects. A relatively new technique for predicting stacking fault behavior in NT metals is atomistic-based phase field dislocation dynamics (PFDD). The phase field approaches have been used to model some particular phase transformations. Koslowski *et al.* described an alternative way to use a phase field approach to model dislocation glide and interactions, then, the phase field term evolved to phase field dislocation dynamics [31–35]. Recently, another study by Hunter *et al.* presented an extended study of the PFDD approach by full resolution of material gamma surface parameters via atomistic calculations. They calculated partial dislocation nucleation and propagation kinetics in nanoscale grains. In the computational part of this thesis, we aim to carry the PFDD approach one step further by implementing twin boundaries. Particularly, the stress, grain size and twin boundary spacing conditions will be systematically tuned to reveal the net effect of twin boundaries on a dislocation motion.

In summary, the primary objective of this thesis is to develop a connected experimental and computational modeling study to elucidate the fundamental mechanisms that control the strength and stability of NT metals. By this study, we are

aiming to create a multiscale deformation atlas of NT metals starting from single dislocation reactions to cumulative mesoscale effect.

## 1.1 Strength vs Grain Size

One of the most critical observations on metals is the significance of microstructure. Microstructural elements of grains, grain boundaries, precipitates, etc. interact with the dislocations under applied stress conditions and have significant effects on the mechanical properties. In 1950's E. O. Hall and N. J. Petch independently wrote two groundbreaking papers on the correlation of strength with grain size. The Hall-Petch model is as follows:

$$\sigma_y = \sigma_0 + kd^{-n} \tag{1.1}$$

where $\sigma_y$ is the yield strength, $\sigma_0$ is the friction stress, $k$ is the Hall-Petch slope, $d$ is the grain size and $n$ is a constant [36]. It is empirically demonstrated that the grain size strengthening is a reliable phenomenon for engineering applications. The practical use of the Hall-Petch relationship arose from its $kd^{-1/2}$ dependence. Here, $k$ represents the resistance of grain boundaries to dislocation mobility (transmission through grain boundaries), and $d$ represents the density of grain boundaries that a dislocation faces during its movement. A high density of grain boundaries limits the length of dislocation pile-ups and, due to restricted dislocation motion, extraordinarily high yield stress values can be observed. However, the extraordinary mechanical properties of nc metals are limited by mechanisms related to the competing length scales. When the grain is too small, dislocation-mediated plasticity can be suppressed and leads to strain localization and a loss of ductility. At these length scales, unusual deformation mechanisms such as

grain boundary migration and grain rotation can be observed, and the Hall-Petch relationship is no longer active (i.e., Inverse Hall-Petch) [37]. Schematic representation of the crossover regime from Hall-Petch to Inverse Hall-Petch behavior is shown in Figure 1.1. In Figure 2.1, when grain size is reduced below 20-30 nm, a dramatic reduction in mechanical properties is observed. Moreover, there is one more main drawback for nc metals: creep resistance or thermal stability. The nanostructured grains can grow rapidly to decrease the energy of the material and caused a loss of strength, even at room temperature [38].

The increasing demand for high-strength metals with better thermal properties has driven researchers to attempt various approaches [39]. In the rest of this thesis, we will focus on the nanotwinned metals.

## 1.2 Twins and Twin Boundaries

A detailed description and fundamentals of twinning can be found in the *"International Tables for Crystallography, Volume D: Physical Properties of Crystals"*. Twins are described as a shifted portion of a crystal in grain boundaries where the crystal lattices on each side are related by mirror symmetry across imaginary twin plane [41]. As represented in Figure 1.2, the atoms in a lattice mirrored themselves across twin boundary (Fig 2.2b) rather than a random mismatch like a grain boundary (Fig 1.2a). The plane where shifting mechanism starts is considered as the twinning plane or twin boundary. Here, drawing a plane that is parallel to one of the habit planes by an angle of 70.53˚ can easily represent a twin plane. In fcc metals atoms can sit specified positions; A, B and C. In a perfect fcc crystal the defined atomic sequence is …ABCABCABC…

for the twinning case, the stacking fault sequence is shifted to …ABCACBABC… In this case twinning region represented as "ACBA" portion of the stacking sequence (Fig 1.2b).

In fcc metals, there are two important twin boundary types: i) Σ3 {111} coherent twin boundary (described above) and Σ3 {112} incoherent twin boundary. It is worth to mention that, depending on material, other types of twin boundaries may also become important. The Σ3 {112} incoherent twin boundary can be visualized by cleaving a crystal on a {111} plane, then 180˚ rotation along the <111> axis and finally rejoining. The configuration of this boundary is shown in Figure 1.3.

Both coherent and incoherent twin boundaries are energetically much different than grain boundaries. For example, in Cu, while twin boundary energies of the coherent and incoherent twin boundaries are in the range of 30 $mJ/m^2$ or lower (coherent twin boundary energy is much less than incoherent), the energy of a high angle grain boundary is around 700 $mJ/m^2$ [42].

According to the different geometric and energetic considerations of twin boundaries compared to grain boundaries, one can expect to see different dislocation reactions (nucleation and propagation). However, both boundaries behave in a similar fashion to some degree. Simply, both boundaries acts as an obstacle to dislocation motion/transmission at some degree. Perhaps, the easiest way to demonstrate the dislocation twin boundary interactions is using double Thompson tetrahedron (Figure 1.4). In Figure 2.4a the (ABC) plane represents the twin boundary and tetrahedrons are slip systems in fcc. Regarding dislocation reactions, Zhu *et al*. developed a very straightforward analytical model for all possible dislocation reactions with twin

boundaries in their recent study. The most striking observation of this study is the energy barriers reported for partial dislocations to interact with the twin boundary are much lower than the ones for full dislocation. Here, one should note that these calculations are valid for isotropic elasticity and there is no stacking fault effect [43]. A complimentary study is done by Ezaz *et al.* They studied the energetics of dislocation twin boundary reactions using generalized stacking fault energy by atomistic simulations and reported similar results [44]. Moreover, in the literature, there are some studies focused on twin boundaries on different systems, like twinned nanowires under mechanical deformation [45,46]. In this study, they showed that twin boundaries in a nanopillar can reduce the serrated flow and strengthen the material by Lomer-Cottrell locks.

## 1.3 Nanotwinned metals

NT metals are specific twinned materials with a twin boundary spacing of 10-20 nm. NT metals are firstly studied around 1970's with sputtered Cu films (growth twins) [47,48]. These studies are mostly focused on the fabrication without giving any explanation of underlying fundamental mechanisms. To fill out this intellectual gap and commercial interest on these superior materials; theoretical, computational and experimental studies are intensively employed. First modern trials were done with the sputtered NT-Cu and stainless steel [9]. Zhang and Misra reported a systematic study with NT, ultra fine-grained and nc Cu under same conditions, and showed a direct comparison between these materials. The results are very impressive: NT Cu showed nearly 1.5 times higher hardness compared to the nc counterpart, and this scale increased for ultra-fine grained case- reached to nearly two times greater values (Figure 1.5).

Few other experimental studies also showed that twin boundaries could stop or reduce dislocation motion somewhat similar to grain boundaries. Increased amount of the twin boundary density resulted in higher mechanical properties. Chen *et al.* conducted another complimentary study for the same Cu system. The strength and ductility variations with twin spacing are shown in Figure 1.6. It is clearly seen that for 4 nm twin spacing NT- Cu showed comparable ductility values with the coarse-grained Cu without losing strength.

Recently, Ott *et al.* demonstrated a complete systematic study of the effect of twin boundary orientation, twin spacing, grain size and processing conditions on NT Ag [12]. They reported a processing protocol of how to control NT structure and orientation by controlling deposition conditions. They fabricated two different sets of twin structures; one is randomly oriented NT's and another is the aligned on growth direction. They revealed that the strength and ductility were strongly dependent on the deposition rate. Figure 1.7 shows the tensile yield strength as a function of a texture parameter. Another outcome of this study is revealing microstructural reasons of relatively softer films.

Another important feature of NT metals is their improved fatigue resistance and improved microstructural stability under cyclic loads. Compared to conventional Cu, NT Cu shows better performance, especially for large stresses [50]. However, after reaching the critical stress level, crack nucleation is observed as a result of detwinning [51].

Microstructural stability of NT metals is tested for the high-temperature applications. Nc metals have indigent thermal stability. For nc Cu the grain growth temperature was reported at 0.35 $T_m$ [52] or lower for other metals, such as Ni very close

to room temperature. In the literature, there are limited number of papers focus on thermal stability, and among them in nearly all cases, *ex-situ* testing techniques are employed. Therefore, the *in-situ* high-temperature mechanical properties of NT metals are unknown. However, *ex-situ* measurements can give some insights about thermal properties. Only a few studies on NT Cu are revealed significant enhancement on thermal stability of NT sturucture at nearly 0.8 $T_m$. The size of a columnar grain increases almost factor of 10, while keeping the twin spacing and strength constant (only increased from 4 nm to 16 nm) [11]. Zhang *et al.* have done another critical and complimentary study. They observed dislocation nucleation and propagation reactions by high-temperature in-situ TEM at 285 ˚C and reported a critical temperature regime around 200 ˚C. Above that critical temperature, dislocation density dramatically decreased.

As stated above, the high temperature *in-situ* mechanical properties of NT metals are unknown. One of the research objectives of this thesis proposal is to investigate the high temperature *in-situ* mechanical properties of NT metals via high-temperature nanoindentation.

## 1.4 Nanoindentation Testing at Elevated Temperatures

The traditional description of hardness is a measure of a material resistance to deform of its surface. The standard types of hardness measurements are scratch hardness, impact hardness and indentation hardness. During the standard hardness testing, indented mark is analyzed with precise calculations according to the indenter geometry; the geometry can be Brinell, Rockwell, Vickers or Knoop. Nanoindentation, however, is a completely different technique with its unique sensing and analyzing capability. The well-established procedure of “Oliver and Pharr” can be applied to load-displacement

hysteresis to investigate the mechanical properties of a testing material [24]. During a nanoindentation experiment, the depth of penetration, the applied load and the elastic response of a material are simultaneously measured by ultra-sensitive sensors. A typical nanoindentation load-displacement curve is shown in Figure 1.8. Here, one of the most important parameter is the indenter geometry. It represents a critical parameter that should be normalized for every indentation by the indenter area function as it changes during measurements.

The high-temperature nanoindentation is very recent analysis technique and still requires lots of instrumental updates. Owing to being relatively complicated and hard experimentation technique, there are very limited number of high-temperature nanoindentation studies undertaken to date [18–20,22,53–56]. These efforts can be divided into two broad sub-categories depending on the heating capability of the instrument. The first group is only sample heating configuration. In this case, due to high thermal flux from sample environment, the maximum operation temperature is limited to around 100 ˚C. Schuh *et al.* verified experimentally a high level of thermal drift at higher temperatures [18]. Thermal drift refers to any change in depth or force measurement when no displacement is supposed to occur. The second group is both sample and tip heating. The degree of thermal drift can be minimized by this isothermal contact approach, thus much higher temperatures can be studied comparing to only sample heating configuration [57].

### 1.4.1 Challenges and Possible Error Sources of High Temperature Nanoindentation and Noise Reduction Method

High-temperature nanoindentation is a unique technique for obtaining mechanical properties from a very small portion of the material at desired temperatures. However, due to high sensitivity (both hardware and thermal flux) of the instrument, one should be aware of possible error sources. The primary sources of the error during high-temperature nanoindentation tests can be classified in the following sub-categories:

- The errors attributed to sensing accuracy of position sensors: initial depth penetration, machine compliance, zero load calibration, load calibration, vibrational noise from minus-k table (anti-vibration table), electrical noise, etc.
- The errors attributed to thermal drift and heating elements: Magnesium silicate cement is used to attach a sample on the sample holder. The thickness of cement might change the temperature distribution (thermal drift). Other possible noise sources are; indenters tip maintenance, diamond area function analysis, thermocouples, etc.
- Errors attributed to samples and sample preparation: surface roughness, sink/pile-up effects, and possible contaminations.

In this study, all system conditions, calibrations and maintenance issues were done periodically. Indenter geometry checked by diamond area function (DAF) analysis after each high-temperature experiment.

The origin of the noise is mostly defined as an unwanted perturbation to a detection signal. In particular for the nanoindentation, the detection signal is a mechanical

response of a material to the indenter tip. The major factors affecting the stability and reliability of the nanoindentation load-displacement curves are thermal drift and environmental/mechanical vibrations that is transmitted to the instrument. The focus of this section is to use informatics based methodology to remove noise from nanoindentation data by analyzing the load-displacement curves. A similar approach will be used as reported in [23] that is a dimensionality reduction approach –principal component analysis (PCA) to recognize mechanically important patterns from noise patterns. Figure 1.9 shows the logic of PCA and principal components of the detected signal.

PCA analysis reduces the dimensionality of the data while keeping the variation in the data set [51-53]. The reduction is performed by identification of the principal components (PC's) along the maximum variation of the data. The newly created PC's can be used to separate the information from the noise. The theoretical background of the PCA is described in detail [51-53].

At least 20 indentations, each with a maximum depth of 500 nm, were performed on the nt silver films with varying texture parameters. The loading and unloading rates were 2 mN/s each and peak load was held constant at maximum depth value of 800 nm (depending on experiment) for 120 s for the high-temperature measurements and 20 s for the room temperature experiments. An example of the load-displacement curves obtained for NT silver film is shown in Figure 1.10 as black hysteresis. It is clearly seen in this figure that especially during unloading, curves do not perfectly fit with the Oliver-Pharr treatment to precisely calculate elastic properties and require a noise removal procedure to obtain more reliable mechanical properties. The key idea of this section is to compare

the load-displacement curves of various indentations and to remove noise by keeping only the statistically significant signals from these indentations. One-by-one comparison of repeated indentations is a multivariate problem, thus, the spectral segments (the smallest segment is a depth value at particular load or vice versa) of the variations are used. First, the linear interpolation fitting is used to perform an interpolation on regular intervals of load-displacement data. The linear interpolation fits the data by successive points to a straight line. Then, load-displacement data converted into a matrix form that is composed of the depth and the load reading. Finally, PCA analysis is performed using Matlab calculation library. PCA converts these data into a series of PC's that can be defined as noise or other specific characteristic of the experiment. The calculated PC values are shown in the Table S1. The PC1 captures more than 99.5% variance that has the mechanical response of the data. On the other hand, the other PC's (PC2, PC3 and PC4) captures less significant statistical trends in the data. Using these PC values noise reduction can be achieved by removing lower PC's from the load-displacement data set. Figure 1.10 show a direct comparison between the raw nanoinentation load-displacement data (black) and the after PCA- noise reduction curve (red). The nanoindentation load-displacement hysteresis after PCA treatment has fewer perturbations without loss of a significant mechanical response.

## References

[1] Yamakov V, Wolf D, Phillpot SR, Mukherjee AK, Gleiter H. Philos Mag Lett 2003;83:385.

[2] Koch C. Scr Mater 2003;49:657.

[3] Han BO, Lavernia EJ, Lee Z, Nutt S, Witkin D. Metall Mater Trans A 2005;36:957.

[4] Wang Y, Chen M, Zhou F, Ma E. Nature 2002;419:912.

[5] Horita Z, Ohashi K, Fujita T, Kaneko K, Langdon TG. Adv Mater 2005;17:1599.

[6] Zhao YH, Liao XZ, Cheng S, Ma E, Zhu YT. Adv Mater 2006;18:2280.

[7] Zhao Y, Zhu Y, Lavernia EJ. Adv Eng Mater 2010;12:769.

[8] Lu K, Lu L, Suresh S. Science 2009;324:349.

[9] Lu L, Shen Y, Chen X, Qian L, Lu K. Science 2004;304:422.

[10] Lu L, Chen X, Huang X, Lu K. Science 2009;323:607.

[11] Anderoglu O, Misra A, Wang H, Zhang X. J Appl Phys 2008;103:094322.

[12] Ott RT, Geng J, Besser MF, Kramer MJ, Wang YM, Park ES, LeSar R, King AH. Acta Mater 2015;96:378.

[13] Oliver WC, Pharr GM. 1992.

[14] Oliver WC, Pharr GM. J Mater Res 2011;19:3.

[15] Oliver WC, Pharr GM. 2010;35.

[16] Pharr GM, Oliver WC. J Mater Res 2011;4:94.

[17] Schuh CA. Mater Today 2006;9:32.

[18] Trenkle JC, Packard CE, Schuh C a. Rev Sci Instrum 2010;81:073901.

[19] Yang B, Wadsworth J, Nieh T-G. Appl Phys Lett 2007;90:061911.

[20] Han YD, Jing HY, Nai SML, Xu LY, Tan CM, Wei J. J Electron Mater 2010;39:223

[21] Pharr GM. Mater Sci Eng A 1998;253:151.

[22] Trelewicz JR, Schuh C a. Scr Mater 2009;61:1056.

[23] Everitt NM, Davies MI, Smith JF. Philos Mag 2011;91:1221.

[24] Goodall R, Clyne TW. Acta Mater 2006;54:5489.

[25] Liu G, Xu G. J Mech Phys Solids 2009;57:1078.

[26] Wu ZX, Zhang YW, Srolovitz DJ. Acta Mater 2009;57:4508.

[27] Wu X, Zhu YT, Chen MW, Ma E. Scr Mater 2006;54:1685.

[28] Bahmanpour H, Kauffmann a., Khoshkhoo MS, Youssef KM, Mula S, Freudenberger J, Eckert J, Scattergood RO, Koch CC. Mater Sci Eng A 2011;529:230.

[29] Yang H, Wu X-X, San X-Y, Shen L, Zhu X-K. Procedia Eng 2012;36:307.

[30] Wang ZW, Wang YB, Liao XZ, Zhao YH, Lavernia EJ, Zhu YT, Horita Z, Langdon TG. Scr Mater 2009;60:52.

[31] Koslowski M, Cuitiño AM, Ortiz M. J Mech Phys Solids 2002;50:2597.

[32] Hunter A, Koslowski M. J Mech Phys Solids 2008;56:3181.

[33] Koslowski M. Phys Rev B 2010;82:1.

[34] Lei L, Koslowski M. Philos Mag 2011;91:865.

[35] Koslowski M. Philos Mag 2007;87:1175.

[36] Hall EO. Proc Phys Soc Sect B 2002;64:747.

[37] Meyers MA. A, Mishra A., Benson DJJ, Meyers M.A., Mishra A., D.J. B. Prog Mater Sci 2006;51:427.

[38] Upmanyu M, Srolovitz DJ, Lobkovsky A. E, Warren JA., Carter WC. Acta Mater 2006;54:1707.

[39] Greiner J, Schwarz R, Zharikov S, Orio M, Paradijs J Van, Klis M Van Der, Stars TN, Mchardy IM, Papadakis IE, Middleton M, Ward M, Done C, Mushotzky RF, Wagoner R V, Begelman MC, Lehr DE, Zhang SN, Chen W, Belloni T, Vietri M, Morsink SM, Tchekhovskoy A, Blandford RD, Quataert E, Heinz S, Markoff S, Koerding E, Knigge C, Uttley P, Fender RP, Mcclintock JE, Zhang B, Gao H, Krolik JH, Hawley JF. Science (80- ) 2012;337:951.

[40] Greer JR. Nat Mater 2013;12:689.

[41] Li N, Wang J, Misra A., Zhang X, Huang JY, Hirth JP. Acta Mater 2011;59:5989.

[42] Wang J, Anderoglu O, Hirth JP, Misra a., Zhang X. Appl Phys Lett 2009;95:1.

[43] Zhu YT, Wu XL, Liao XZ, Narayan J, Kecskés LJ, Mathaudhu SN. Acta Mater 2011;59:812.

[44] Ezaz T, Sangid MD, Sehitoglu H. Philos Mag 2011;91:1464.

[45] Sansoz F, Huang H, Warner DH. Jom 2008;60:79.

[46] Wang J, Huang H. Appl Phys Lett 2006;88:1.

[47] Dahlgren SD. J Vac Sci Technol 1974;11:832.

[48] Merz MD, Dahlgren SD. J Appl Phys 1975;46:3235.

[49] Zhang X, Misra A. Scr Mater 2012;66:860.

[50] Shute CJ, Myers BD, Xie S, Barbee TW, Hodge A. M, Weertman JR. Scr Mater 2009;60:1073.

[51] Shute CJ, Myers BD, Xie S, Li SY, Barbee TW, Hodge a. M, Weertman JR. Acta Mater 2011;59:4569.

[52] Islamgaliev RK. Mater Sci 1997;236:335.

[53] Lotfian S, Molina-Aldareguia JM, Yazzie KE, Llorca J, Chawla N. J Electron Mater 2013;42:1085.

[54] Byre T, Park WT. 2002.

[55] Wang CL, Zhang M, Nieh TG. J Phys D Appl Phys 2009;42:115405.

[56] Wang F, Xu K. Mater Lett 2004;58:2345.

[57] Franke O, Trenkle JC, Schuh CA. J Mater Res 2011;25:1225.

Table 1. Variance captured by PC's for the load-displacement curves of NT silver films.

| **Principal Component** | **Variance captured (%)** |
|---|---|
| 1 | 99.53 |
| 2 | 0.05 |
| 3 | 0.01 |
| 4 | 0.01 |
| 5 | 0.01 |
| 6 | 0.01 |

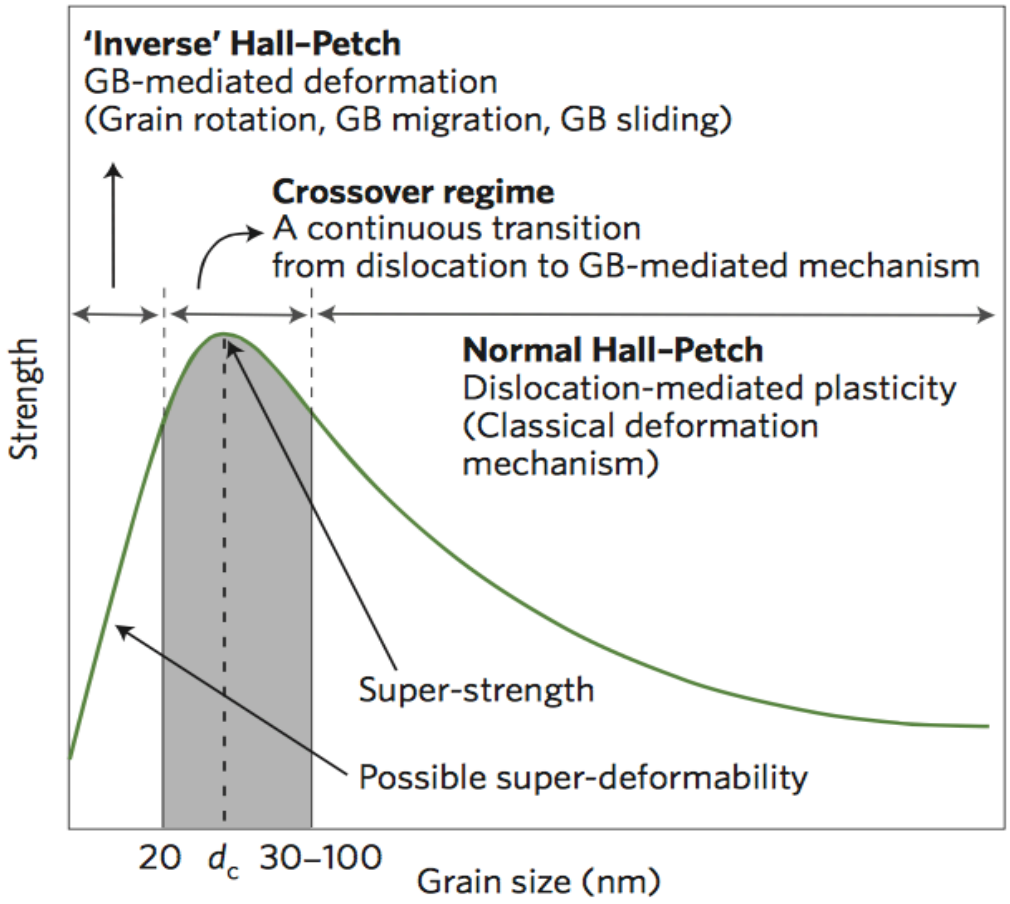


Figure 1.1 Hall-Petch relationship at different length scales [40].

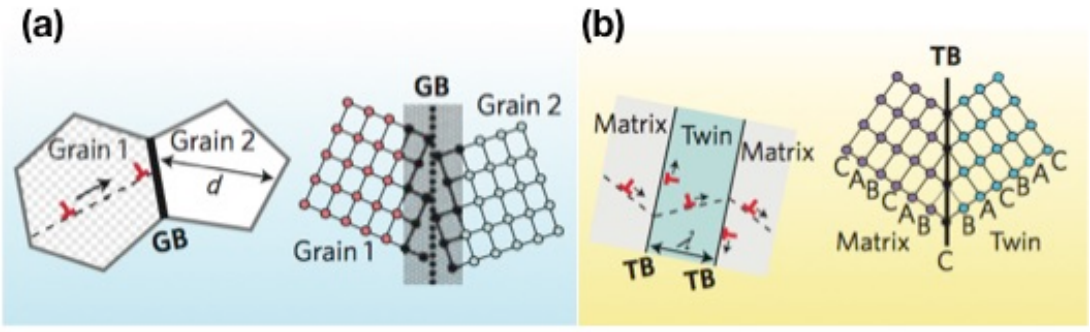


Figure 1.2 Schematic representation of (a) a grain boundary, (b) twin boundary [40].

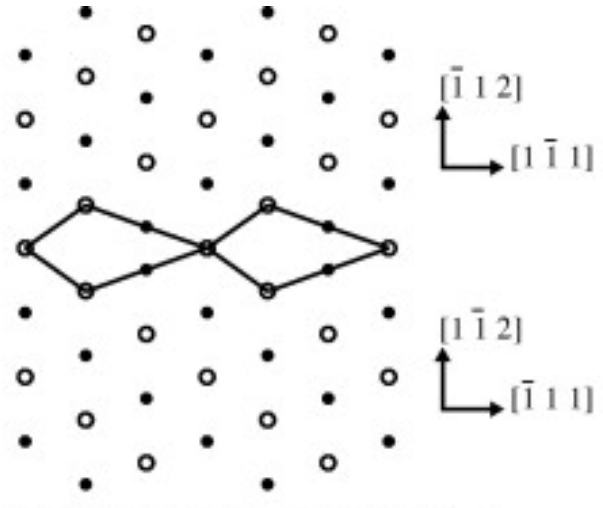


Figure 1.3 Schematic configuration of incoherent twin boundary [5].

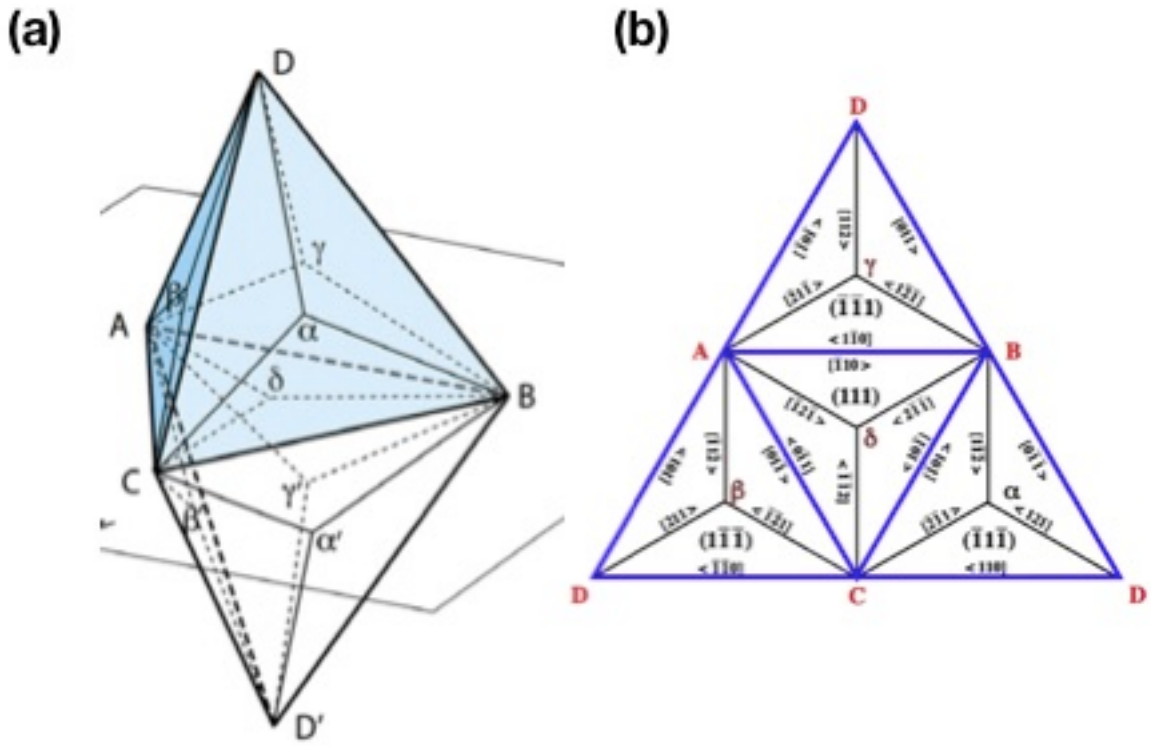


Figure 1.4 Schematic representation of slip planes in fcc lattice. (a) (ABC) plane represents twin boundary, (b) plausible slip planes and partial/full dislocation components [43].

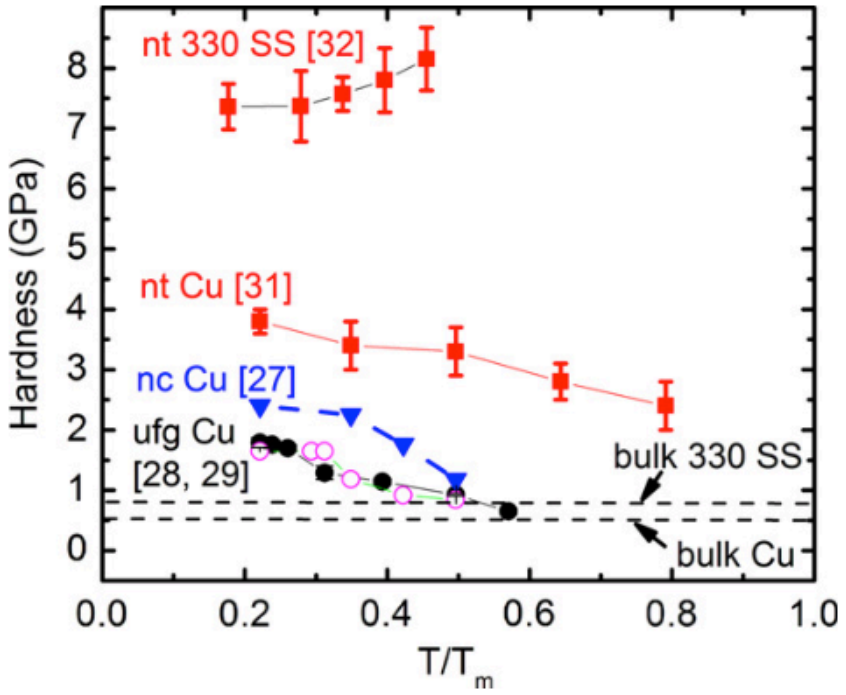


Figure 1.5 Evolution of hardness for 330 stainless steel, NT Cu, nc Cu and ultra-fine grained Cu [49].

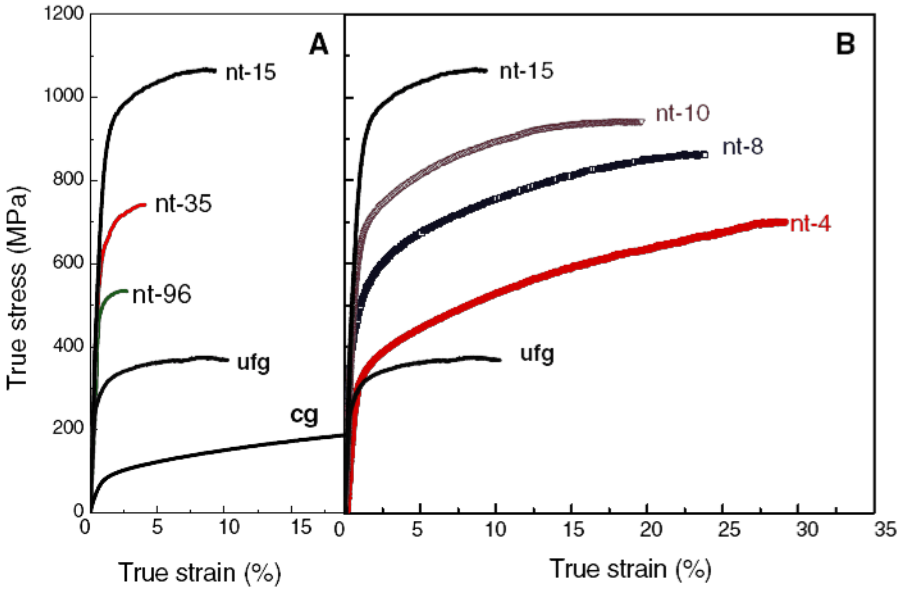


Figure 1.6 Tensile test results for NT, ultra fine-grained and NT Cu with various thin spacing. Maximum strength reached with 15 nm and maximum strain achieved with 4 nm twin spacing [49].

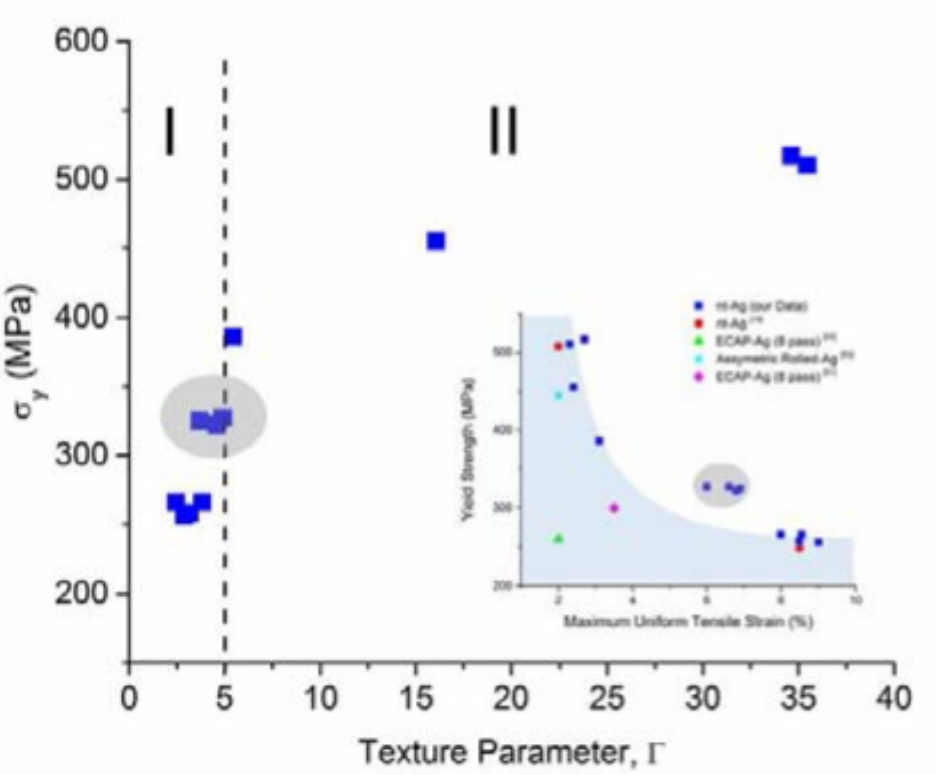


Figure 1.7 tensile yield stress as a function of texture parameter (twin boundary orientation). Blue dots in small graph illustrated the yield strength-maximum tensile strain data points [12].

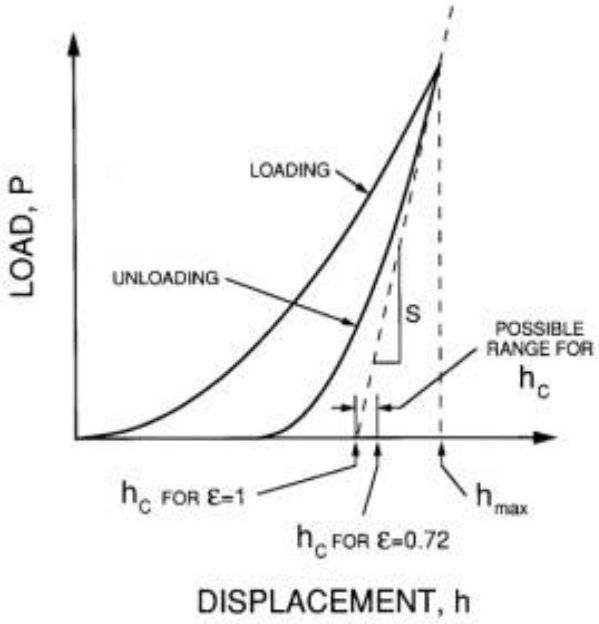


Figure 1.8 Typical nanoindentation load-displacement curve obtained with a Berkovich indenter.

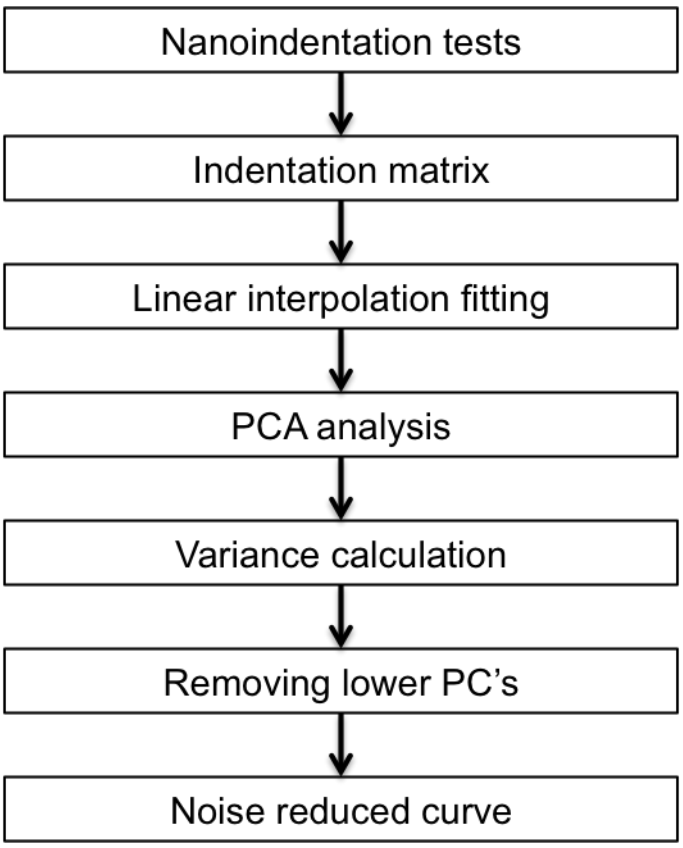


Figure 1.9 The logic of the PCA analysis.

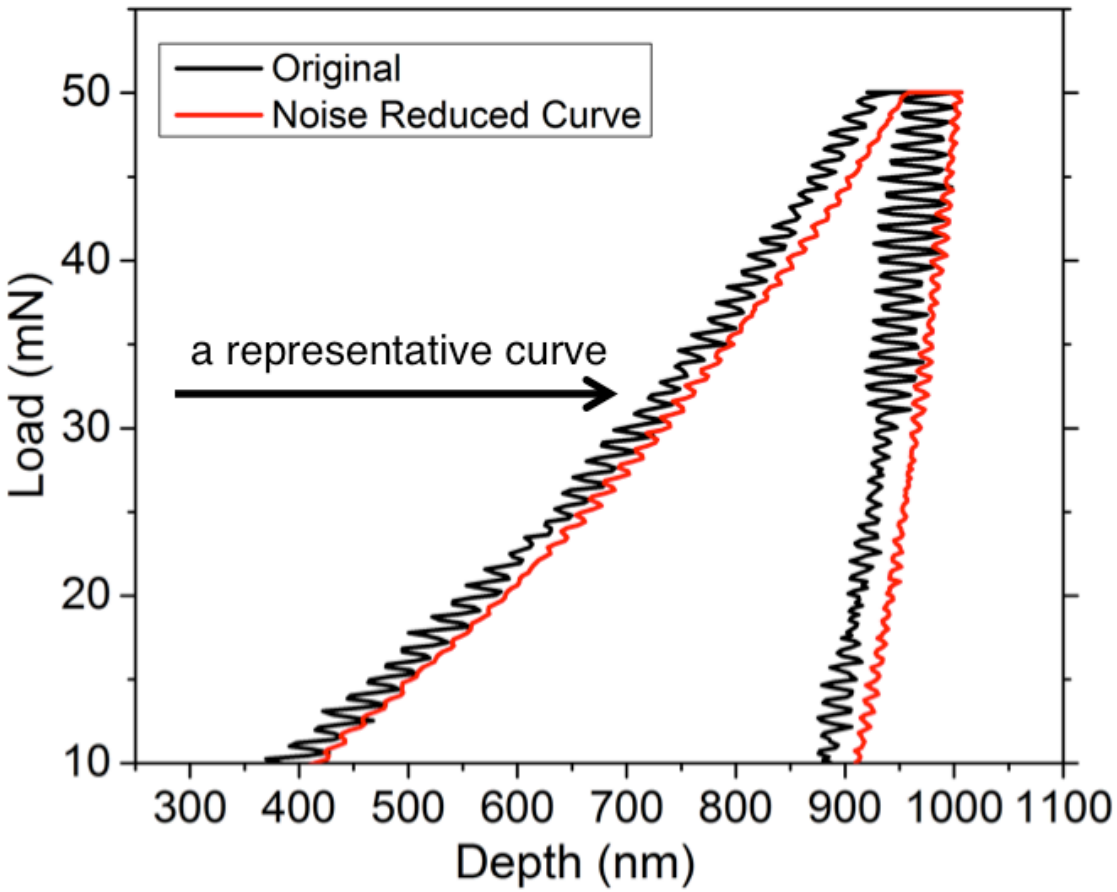


Figure 1.10. Experimental (black) and noise removed (red) load-displacement curves.

# CHAPTER 2. DEPENDENCE OF THE MECHANICAL PROPERTIES OF NANOTWINNED SILVER FILMS ON TEMPERATURE AND TEXTURE

A paper submitted to Scripta Materialia

H. Yavas[1,2], M. F. Besser[1], R. T. Ott[1], J. Geng[1], K. Rajan[4], and R. LeSar*[1,2]

[1] Division of Materials Sciences and Engineering, Ames Laboratory, Ames, IA 50011

[2] Department of Materials Science and Engineering, Iowa State University, Ames, IA 50011

[3] State University of New York at Buffalo, Department of Materials Design and Innovation, Buffalo, NY 14260

* To whom all correspondence should be addressed.

Email: lesar@iastate.edu

## Abstract

In this study, we employed high-temperature (25-400˚C) nanoindentation to study the high-temperature deformation behavior of nanotwinned silver films as a function of their texture. We found that the maximum hardness value (2.7 GPa) was found for samples with strong <111> texture. The hardness decreased to about 0.1 GPa at 400 ˚C for all textures. Room-temperature hardness measurements made on highly textured samples that had been subjected to non-ambient temperatures for long times showed a hardness (2.5 GPa) that approached non-annealed values. Values for the activation energies for the deformation were determined and suggested dislocation nucleation as the dominant deformation mechanism.

Nanotwinned materials are metals that have high densities of parallel coherent twin boundaries with nanoscale separations. These materials have been a topic of some interest in the past few years owing to their excellent strength [1–10], ductility [11–15], and thermal stability [16–21] relative to their nanocrystalline (NC) counterparts [11,22,23]. Despite these efforts, the deformation mechanisms in these materials remain poorly understood. In this paper, we focus on identifying the deformation mechanisms in nanotwinned silver as a function of the microstructure by measuring their mechanical behavior and determining the activation energies for deformation using the temperature dependence of the strain rate.

The most common techniques to prepare nanotwinned (NT) materials are electrodeposition [24–26] and physical vapor deposition (PVD) [6,10,18,24,27]. In this study, we used magnetic sputtering, a PVD process, that allowed us to control the microstructure, and thus the deformation mechanisms, by varying the deposition rate. High sputtering rates typically yield samples with strong <111> texture, i.e., the grains are aligned with (111) planes being largely normal to the growth direction with the twin boundaries lying in those (111) planes, while lower deposition rates result in more random texture [6]. Recently, Ott *et al.* reported that nanotwinned silver films showed strong differences in behavior depending on deposition, with films deposited at high deposition rates (> 5.4 nm/s) showing very strong <111> texture and exhibiting a large increase in yield strength relative to samples prepared at a lower deposition rate. Their results showed that while there was not a significant change in the twin boundary (TB) spacing [20] between high and low deposition rates, lower rates yielded a more random

texture, with non-[111] oriented grains manifesting few twins and smaller mean grain sizes [28–30].

Nanotwinned metals also exhibit outstanding thermal stability. For example, Anderoglu *et al.* reported high hardness and thermal stability for annealed NT Cu films using nanoindentation experiments [18]. They suggested that twin boundaries act as potential barriers to dislocation climb motion at elevated temperatures. Similarly, Bufford *et al.* examined the deformation behavior of annealed NT silver samples and showed the importance of domain orientation and grain coarsening on the reduction of hardness [17]. Zhang *et al.* recently reported studies of nanotwinned Ag using high-temperature in-situ TEM studies combined with ex-situ room-temperature (annealed) nanoindentation and microscopy experiment. They observed changes in structure and deformation properties around 200 ˚C, with stable grain size and twin spacing below that temperature along with little change in mechanical behavior. Above 200 ˚C, however, the tensile strength of the NT Ag films decreased significantly, as did the overall dislocation density [30], indicating a potential change in the dominant formation mechanism with temperature. To address the question of the effects of grain coarsening and orientation [28] arising in that study, here we employ high-temperature nanoindentation to study the plasticity in NT silver systems as a function of temperature. Nanoindentation was chosen not only because of its sensitivity in determining mechanical properties, but also because of its capability to generate high-resolution force data, which can be then used for further deformation analysis.

To address these questions in a systematic way, the mechanical properties of NT silver films with different textures were measured by means of high-temperature

nanoindentation in the temperature range of 25-400 °C. Additional room-temperature nanoindentation measurements were made on samples after undergoing the high-temperature nanoindentation protocol. To understand the deformation kinetics as a function of temperature, the force-displacement curves were analyzed and the activation energies were calculated.

NT silver films (~ 50 μm thick) were fabricated via physical vapor deposition using magnetron sputtering (Kurt J. Lesker CMS-18 System) on liquid nitrogen cooled (100) oriented Si wafers. Details of the magnetron sputtering process and characterization of the textures were previously discussed by Ott *et al*. [28] and Zhang *et al.* [30], in which the degree of texture was delineated by the parameter "**Γ**", which is defined as

$$\Gamma = \frac{\left(\frac{I_{220}}{I_{111}}\right)_{film}}{\left(\frac{I_{220}}{I_{111}}\right)_{random}} \quad . \qquad (1)$$

$I_{ijk}$ is the intensity of the *ijk* x-ray diffraction peak, as discussed by Ott *et al.* Higher values of **Γ** corresponding to higher {111} texture [28].

Cross-sectional samples (i.e., along the growth direction) were prepared for transmission electron microscopy (TEM) studies using polishing and ion milling sequentially at liquid nitrogen temperature. TEM images were obtained using a FEI Tecnai G(2) F20 operated at 200 kV accelerating voltage, for details see Zhang *et al.* [30].

Nanoindentation tests were performed using the Nanotest Platform nanoindenter (MicroMaterials Ltd., UK) with a Berkovich geometry diamond tip. For the high-temperature experiments, the tip and the sample holder were heated separately. The nanoindentation hardness of NT silver films are obtained according to Oliver-Pharr

analysis [31]. The high-temperature nanoindentation testing followed the protocol shown in Figure 1. Experiments were carried out at 25 (RT), 100, 200, 300 and 400 °C. For each 100 °C increment, the sample was retracted from the indenter by around 100 μm, then allowed to thermally stabilized for about an hour. After achieving thermally stabilized contact, the sample was retracted 25 μm away from the indenter. At each test temperature, at least ten indentations spaced a minimum of 50 μm apart were made. A controlled depth of 500 nm was used to avoid effects from the substrate on the mechanical response. The loading and unloading rates were constant at 2 mN/s and the peak load was held constant at ~500 nm for 120 seconds. The dwell period of the nanoindentation test was used for further strain rate and activation energy calculations. The activation energy analysis is done according to Goodall [32]. At the end of the dwell period, the load was gradually reduced to zero with a rate of 2 mN/s. During unloading, the drift was measured by introducing a 60s hold segment at 10% of the maximum load. It should be noted that for each of the four high-temperature target temperatures, the experiments required at least two hours for pre-indentation adjustments and thermal stabilization and another hour between the first and the last indentation. Thus, the samples were at non-ambient temperatures for about 14 hours. For clarity, samples that have undergone the testing protocol shown in Fig 2.1 and then returned to room temperature are referred to as *post-indentation* or *long-annealed* samples.

TEM images of the high and low texture as-deposited NT silver films are shown in Figure 2.2a. The average grain size and average twin spacing are measured and presented in Figure 2.2b. The high texture silver films show clear <111> orientation and a columnar grain structure. The width of these highly textured columnar domains is ~250

nm in diameter. For samples with low texture, the minimum grain size is about 50 nm and has a composite of <111> oriented grains with a high density of twins and randomly oriented untwinned grains. The twin spacing does not depend on the texture parameter, showing an average twin boundary spacing of ~10 nm for all samples. The dependence of the twin density on the film texture (i.e., Γ) was shown previously by Ott et al. [28].

Figure 2.3a shows the average hardness variations of the NT silver films with different texture parameters as a function of temperature. The first and the most obvious observation is the significant dependence of the hardness on texture in NT silver films. At room temperature, for example, the highly <111> textured film shows a hardness (2.71±0.14 GPa) that is over a factor of 2.2 greater than its low texture counterpart (1.25±0.15 GPa). These results are in good agreement with uniaxial tensile tests, which show that Ag films with strong <111> texturing exhibit much higher strengths at room temperature than films with little <111> texturing [28,30]. At temperatures higher than room temperature, however, the hardness versus texture demonstrates two distinct behaviors. *i)* A region up to about 200 ˚C where the hardness of the NT films decreases almost linearly with increasing temperature, which is strongly dependent on the film texture. *ii)* A region for temperatures > 200 ˚C, where the hardness dramatically decreases with increasing temperature (down to 0.2 GPa) essentially independent of the film texture. Using in-situ TEM heating, Zhang et al. [30] found that the dislocation density in NT silver films decreased significantly after annealing to 400 ˚C (0.55 $T_m$). The annihilation of the dislocations at high temperatures will reduce dislocation-dislocation interactions and soften the material. Another source of softening may be related with the increase of the grain size at higher temperatures. The grain size values of

the both low and high texture films increase by a factor of three compared to the measurements at room temperature [30]. Enlarged grains and reduced dislocation density thus may lead to easier slip.

To examine the effects of long-annealing times at elevated temperatures on the mechanical properties of the nt-Ag films, we performed additional nanoindentation experiments at room temperature on the samples that had undergone the nanoindentation protocol from Figure 2.1. Figure 2.3b shows the evolution of the hardness change with Γ. The most striking observation from these long-annealed samples is that the highly textured films show superior hardness even after the long annealing times at high-temperatures, with the hardness of the highly textured film (2.71±0.14) decreasing only slightly to 2.51±0.16 GPa. Meanwhile, the hardness of low-texture films decreased from 1.25 GPa down to about 0.80 GPa or lower. The retention of high hardness in long-annealed high texture NT Ag may be a consequence of thermal stability of nanotwinned structure. Our group reported that the twin boundary spacing mostly showed constant values ~10 nm even after 400 ˚C (0.55 $T_m$) annealing [30]. Specifically, the twin density and twin boundary spacing do not change with increasing temperature (about 200 ˚C); therefore the high density of twin boundaries may effectively resist the transmission of dislocations. Bufford et al. [17] show similar thermal stability for (111) oriented silver films.

A representative stress evolution with time for different testing temperatures is shown in 4a. We find that the effective stress values are approximately 0.8 GPa and 0.1 GPa for indentations below and above 200 ˚C, respectively. Given a constant stress over a range of temperatures, the slope of the $log\,\dot{\varepsilon}$ *vs* $1/T$ curve will be the apparent

activation energy. Our data for the range up to 200 ˚C is shown in Figure 2.4b. The measurements at 300 ˚C and 400 ˚C are excluded here because their effective stress levels did not overlap with the lower temperature data. For better comparisons, only the Ag films with high texture, intermediate texture and low texture are used for this analysis. The deformation activation energy for all texture parameters are found to be between 40 and 50 kJ/mol in the temperature range of 25 – 200 °C. The lowest value of 40±4 kJ/mol is calculated for low texture and the highest one is 48±4 kJ/mol for high texture case.

During high-temperature nanoindentation, multiple deformation processes may be activated. The values of the apparent activation energy give us some insights of temperature-dependent dominant deformation mechanisms. If the deformation takes place in series of steps, the rate-limiting step of the deformation process will be the one with the highest activation energy. In the case of a series of deformation mechanisms acting in parallel, the process having the lowest apparent activation energy will control the deformation. To determine the dominant deformation mechanisms in the room temperature to 200 °C regime, we compared the calculated activation energies with the literature values of activation energies required for specific deformation mechanisms in silver. The reported activation energies for lattice diffusion, boundary diffusion, and core diffusion are 185, 90, and 82 kJ/mol, respectively [33–36]. Given that the activation energies found in our study are considerably less than those values (ranging between 40 and 50 kJ/mol, as described above), we conclude that diffusion is not the dominant deformation mechanism, at least in this temperature regime.

Since diffusion-based mechanisms are ruled out, the most plausible deformation process is dislocation-dependent plasticity. We found good agreement with the activation

energy for plastic flow of silver reported by H. Conrad [36]. Similarly, Filleter et al. calculated energy barriers for partial dislocation nucleation by molecular dynamics simulations and energy barrier calculations for silver nanowires [37]. They found the dislocation nucleation activation energy to be about 0.5 eV (~50 kJ/mol) depending on stress conditions. Liu et al. reported on the sequence of deformation mechanisms in nanotwinned Cu via in-situ nanoindentation and TEM [38]. TEM images of the of the in-situ deformed samples showed deformation starts with detwinning at very low stress levels and then continued by the partial dislocation nucleation and propagation. Moreover, molecular dynamics simulations, by Borovikov et al. show that partial dislocation nucleation governs plasticity for NT Ag films [39].

The agreement with the activation energies determined using high-temperature nanoindentation with previous work suggests that the deformation is dominated by dislocation-dependent (nucleation and propagation) plasticity. That agreement also confirms that high-temperature nanoindentation is a reliable way to determine activation energies for deformation processes [40–42].

In summary, we have employed high-temperature in situ nanoindentation experiments on nanotwinned (NT) ultrafine-grained Ag with different twin densities and grain orientations. From these experiments, we found that the hardness increases significantly (up to 2.71 GPa) as the texture of the films increases, with no change in twin boundary spacing (about 10 nm), indicating that the strengthening is not coming from the blockage of dislocations by the boundaries. Additionally, highly-textured NT Ag films show superior thermal stability up to 200 ˚C and after long hours of annealing at temperatures up to 400 ˚C, which suggests that the microstructural features that control

deformation are thermally stable. Based on activation energy analysis, the apparent activation energy for deformation was determined in the range of 25 ˚C to 200 °C and found to vary between 40 and 50 kJ/mol, depending on texture. The calculated activation energies are consistent with energy barriers associated with dislocation nucleation dependent plasticity and provide, for the first time, a direct measure of the fundamental microscopic deformation processes in the nanoscale materials.

## Acknowledgments

This work was supported by the U.S. Department of Energy (DOE), Office of Science, Basic Energy Sciences, Materials Science and Engineering Division. The research was performed at the Ames Laboratory, which is operated for the U.S. DOE by Iowa State University under contract # DE-AC02-07CH11358. The authors thank Professors Peter Collins and Alexander King from Iowa State University for informative discusions.

## References

[1] O. Anderoglu, A. Misra, J. Wang, R.G. Hoagland, J.P. Hirth, X. Zhang, Int. J. Plast. 26 (2010) 875–886.

[2] L. Lu, Y. Shen, X. Chen, L. Qian, K. Lu, Science 304 (2004) 422–426.

[3] D. Bufford, Y. Liu, J. Wang, H. Wang, X. Zhang, Nat. Commun. 5 (2014) 4864.

[4] D. Jang, X. Li, H. Gao, J.R. Greer, Nat. Nanotechnol. 7 (2012) 594–601.

[5] Y.M. Wang, F. Sansoz, T. LaGrange, R.T. Ott, J. Marian, T.W. Barbee, A. V Hamza, Nat. Mater. 12 (2013) 697–702.

[6] O. Anderoglu, A. Misra, H. Wang, F. Ronning, M.F. Hundley, X. Zhang, Appl. Phys. Lett. 93 (2008) 10–13.

[7] A.M. Hodge, T.A. Furnish, C.J. Shute, Y. Liao, X. Huang, C.S. Hong, Y.T. Zhu, T.W. Barbee Jr., J.R. Weertman, Scr. Mater. 66 (2012) 872–877.

[8] X. Li, Y. Wei, L. Lu, K. Lu, H. Gao, Nature 464 (2010) 877–80.

[9] J. Bezares, S. Jiao, Y. Liu, D. Bufford, L. Lu, X. Zhang, Y. Kulkarni, R.J. Asaro, Acta Mater. 60 (2012) 4623–4635.

[10] D. Bufford, H. Wang, X. Zhang, Acta Mater. 59 (2011) 93–101.

[11] C. Koch, Scr. Mater. 49 (2003) 657–662.

[12] A.M. Hodge, T.A. Furnish, A.A. Navid, T.W. Barbee, Scr. Mater. 65 (2011) 1006–1009.

[13] Z.X. Wu, Y.W. Zhang, D.J. Srolovitz, Acta Mater. 57 (2009) 4508–4518.

[14] M. Dao, L. Lu, Y.F. Shen, S. Suresh, Acta Mater. 54 (2006) 5421–5432.

[15] Z.X. Wu, Y.W. Zhang, D.J. Srolovitz, Acta Mater. 57 (2009) 4508–4518.

[16] X. Zhang, A. Misra, Scr. Mater. 66 (2012) 860–865.

[17] D. Bufford, H. Wang, X. Zhang, J. Mater. Res. 28 (2013) 1729–1739.

[18] O. Anderoglu, A. Misra, H. Wang, X. Zhang, J. Appl. Phys. 103 (2008) 94322.

[19] X. Zhang, A. Misra, Scr. Mater. 66 (2012) 860–865.

[20] Y. Zhao, T.A. Furnish, M.E. Kassner, A.M. Hodge, J. Mater. Res. 27 (2012) 3049–3057.

[21] Y. Wang, A. Hamza, E. Ma, Acta Mater. 54 (2006) 2715–2726.

[22] V. Yamakov, D. Wolf, S.R. Phillpot, A.K. Mukherjee, H. Gleiter, Philos. Mag. Lett. 83 (2003) 385–393.

[23] V. Yamakov, D. Wolf, S.R. Phillpot, A.K. Mukherjee, H. Gleiter, Nat. Mater. 3 (2004) 43–47.

[24] Z.S. You, L. Lu, K. Lu, Acta Mater. 59 (2011) 6927–6937.

[25] L. Lu, R. Schwaiger, Z.W. Shan, M. Dao, K. Lu, S. Suresh, Acta Mater. 53 (2005) 2169–2179.

[26] Y.F. Shen, L. Lu, M. Dao, S. Suresh, Scr. Mater. 55 (2006) 319–322.

[27] A.M. Hodge, Y.M. Wang, T.W. Barbee, Scr. Mater. 59 (2008) 163–166.

[28] R.T. Ott, J. Geng, M.F. Besser, M.J. Kramer, Y.M. Wang, E.S. Park, R. LeSar, A.H. King, Acta Mater. 96 (2015) 378–389.

[29] Y.M. Wang, F. Sansoz, T. LaGrange, R.T. Ott, J. Marian, T.W. Barbee, A. V Hamza, Nat. Mater. 12 (2013) 697–702.

[30] H. Zhang, J. Geng, R.T. Ott, M.F. Besser, M.J. Kramer, Metall. Mater. Trans. A 46 (2015) 4078–4085.

[31] W.C. Oliver, G.M. Pharr, J. Mater. Res. 19 (2004) 3–20.

[32] R. Goodall, T.W. Clyne, Acta Mater. 54 (2006) 5489–5499.

[33] J.P. Poirier, Acta Metall. 26 (1978) 629–637.

[34] L. Klinger, E. Rabkin, Scr. Mater. 48 (2003) 1475–1481.

[35] M.E. Kassner, M.T. Pérez-Prado, Prog. Mater. Sci. 45 (2000) 1–102.

[36] H. Conrad, J. Narayan, Scr. Mater. 42 (2000) 1025–1030.

[37] T. Filleter, S. Ryu, K. Kang, J. Yin, R.A. Bernal, (2012) 1–8.

[38] Y. Liu, N. Li, D. Bufford, J.H. Lee, J. Wang, H. Wang, X. Zhang, Jom 68 (2016) 127–135.

[39] V. Borovikov, M.I. Mendelev, A.H. King, R. LeSar, J. Appl. Phys. 117 (2015) 85302.

[40] A.C. Lund, A.M. Hodge, C. a. Schuh, Appl. Phys. Lett. 85 (2004) 1362.

[41] C.A. Schuh, A.C. Lund, J. Mater. Res. 19 (2011) 2152–2158.

[42] J.R. Trelewicz, C.A. Schuh, Scr. Mater. 61 (2009) 1056–1059.

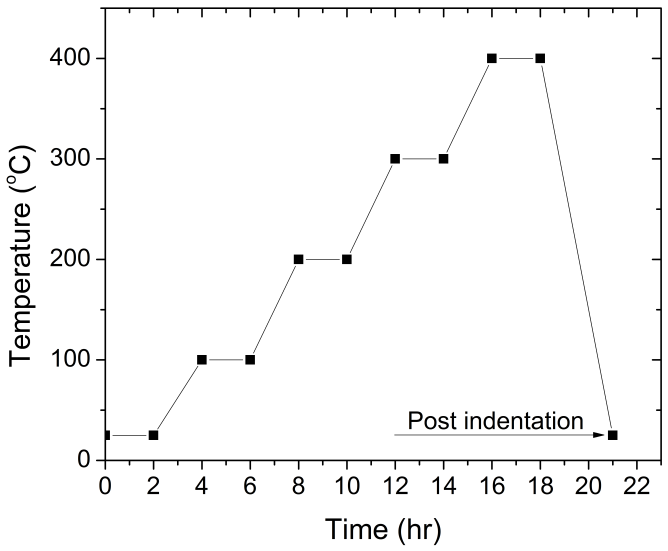


Figure 2.1 High-temperature nanoindentation experiments time and temperature scheme. Last point denotes annealing experiments.

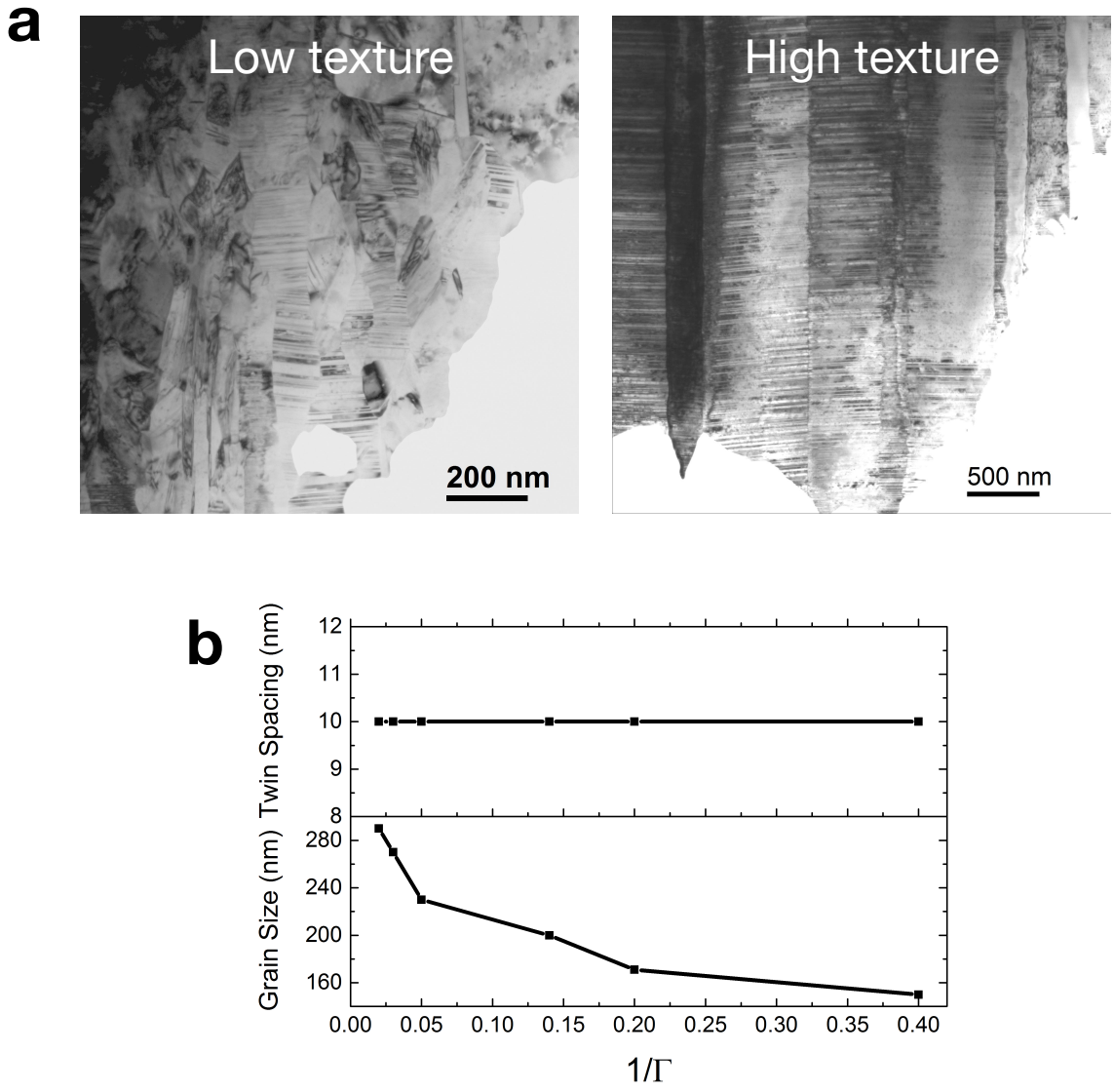


Figure 2.2 (a) TEM images of low and high texture (equation) silver films (b) average *i)* grain size, *ii)* twin spacing, and *iii)* grain size/twin spacing fraction as a function of texture parameter.

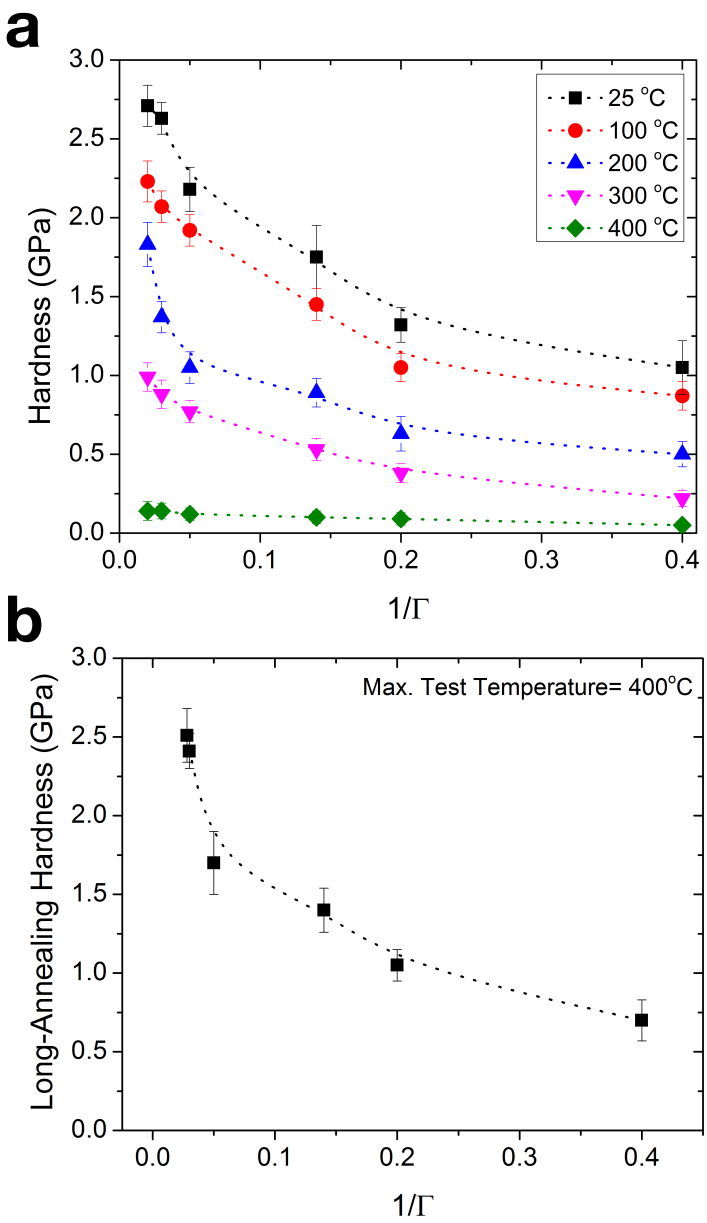


Figure 2.4 (a) stress evolution during dwell period, (b) determination of activation energies for different texture silver films for relatively same stress values.

# CHAPTER 3. EFFECTS OF Cu-SOLUTE ADDITION ON MICROSTRUCTURAL AND MECHANICAL PROPERTIES OF NANOTWINNED SILVER FILMS

A modified version of this paper to be submitted to Acta Materialia

H. Yavas[1,2], R. T. Ott[1], M.F. Besser[1], J. Geng, K. Rajan[3], and R. LeSar*[1,2]

[1] Division of Materials Sciences and Engineering, Ames Laboratory, Ames, IA 50011

[2] Department of Materials Science and Engineering, Iowa State University, Ames, IA 50011

[3] Department of Materials Design and Innovation, State University of New York at Buffalo, Buffalo, NY 14260

* To whom all correspondence should be addressed.

Email: lesar@iastate.edu

## Abstract

A high-temperature nanoindentation study is presented regarding the effect of Cu-solute addition on the microstructural and mechanical properties of nanotwinned Ag films. The high solute content (2.45 at.%) films displayed a hardness 2.47±0.2 GPa, ~20% higher than that of a pure nanotwinned silver. The twin spacing decreased from 10 nm to 5 nm even for the lowest Cu addition. Apparent activation energy for deformation was found to be about 30 kJ/mol, which is comparable to that for dislocation nucleation based plasticity.

**Keywords:** solution hardening, nanotwins, nanoindentation

Nanotwinned (NT) metals have been extensively studied in recent years [1–4]. The high density of twin boundaries may exhibit enhanced strength and thermal stability while maintaining good ductility compared to conventional ultrafine-grained and nano-grained counterparts [5,6]. In similar to nano-grained metals, those superior mechanical properties arise from the resistance of twin boundaries to the dislocation motion, although atomistic mechanisms may differ [7–9]. For instance, the deformation mechanisms of NT metals are mainly dominated by nucleation of the Shockley partial dislocations [9–11]. Recently, atomistic studies predicted the dependence of deformation mechanisms, i.e. Shockley partial nucleation, on stacking fault energy (SFE) [8,9,12–14]. Hence, it is very critical to validate the computational results by the experiments that might shed light on the computationally predicted deformation mechanisms. The conventional protocol to alter the SFE is adding solution elements in base metal [15–20]. The addition of alloying elements may reduce the SFE and hence the twin structure. Moreover, the microstructural properties, such as twin spacing, grain size etc., will be possibly altered, which in turn impact on the final mechanical and thermal performance. Obviously, such solid solution hardening effect is least shocking. However, it is important to quantify such solute effects on microstructural and mechanical behavior and deformation kinetics to examine superior properties of the NT metals as discussed above. In literature, there are few studies focused on solute effects on NT Cu at room temperature [21]. However, in NT Ag films, no works has been reported on the solute addition and its effect on the microstructure and on the resultant both room temperature and high-temperature mechanical properties.

In the present study, we use a high-temperature (25 to 400 ˚C) nanoindentation technique and a transmission electron microscopy to show that how Cu-solute addition

affects the microstructural and mechanical properties of the NT Ag films, by controlling three fundamental operational parameters: i) stress, ii) strain-rate, and iii) temperature. The apparent activation energies are calculated following the constant stress and strain rate conditions that might give insights on determining exact dominant deformation mechanisms of the NT Ag films.

The Ag and Ag-Cu nanotwinned films with a thickness of ~5μm were magnetron sputtered on Si (100) wafers using a sputtering power of 300 W, an Ar pressure of 5 mTorr, and initial base pressure of $1.3\times10^{-8}$ Torr. Varying Cu-solute concentrations of 0, 0.33, 1.37 and 2.45 at.% were prepared by adding a separate Cu- gun into the sputtering chamber. The applied power determined the concentration of solid solutions, which was in the range of 0 to 60 Watt. The maximum solute concentration of 2.45 at.% Cu was reached at 60 Watt.

Nanoindentation experiments were performed under Ar environment using the MicroMaterials NanoTest Platform (Micro Materials Ltd., UK). Prior to the experiments the compliance, load, depth and capacitor spacing calibrations were employed. Experiments were carried out at 25 (RT), 100, 200, 300 and 400 °C with a maximum depth of approximately 500 nm. Each sample and indenter tip was subsequently heated to the target temperature. The fine-tuning was applied to minimize thermal fluctuations between the tip and the hot sample stage. Then, the indenter put in contact with the sample (dummy indent) using a very low load, then contact maintained at least 30 min for thermal stabilization. Dwell time was set as 120 s at maximum load. After the dwell period, the sample was unloaded 20% of the dwell load and 10 seconds of holding period were used to measure thermal drift correction. Indentations were placed at least 100 μm

apart from one another. After finishing the indentation routine, load vs depth curves were analyzed through the Oliver and Pharr method [22–25]. Detailed description and derivations of elastic modulus and hardness calculations are provided elsewhere [26]. Shear modulus was calculated assuming isotropic elasticity through the relation of $\mu = E/2(1+v)$, where $\mu$ is the shear modulus, $E$ is the Young's modulus and the $v$ is the Poisson's ratio for silver. Finally, the activation energy of the samples was calculated using the Goodall's treatment [27]. It is worth to mention that the constant value of stress levels selected to determine strain rates at the temperatures of interest.

Transmission electron microscopy (TEM) images were obtained by a FEI Tecnai G(2) F20 operated at 200 kV accelerating voltage. The TEM cross-sectional samples were prepared using polishing and ion milling sequentially at liquid nitrogen temperature. The details of the TEM studies were published by Zhang et al. [28] and Ott et al. [29].

Representative cross-sectional TEM images of the as-deposited pure NT Ag and NT Ag- 2.45 at.%Cu films are represented in Fig 3.1a. The measured average twin spacing and average grain sizes are shown in Fig 3.1b. It is evident that both films exhibited columnar microstructure and nanotwins lied parallel to <111>-growth direction. The pure silver has a grain size of ~100 nm with average twin spacing of ~10 nm. When the Cu-solute concentration was increased to 2.45 at.%, however, the grain size reduced to ~35 nm where the average refinement of grain size with Cu-concentration was almost 65 %. Interestingly, the twin spacing of the NT Ag-Cu decreased to ~5 nm at the 0.33 at.% Cu alloying and reached a plateau. The very low value of the twin spacing of the NT Ag-Cu alloys, ~5 nm, was far smaller than that of pure Ag. From that end, the room temperature shear modulus and Young's modulus variations are shown in Figure

3.2. It is evident that Cu addition causes an increase in the Young's modulus. For example, the NT Ag film with the highest Cu addition (2.45 at.% Cu) shows a Young's modulus ~100 GPa that is comparably greater than the pure NT Ag ~87 GPa. The similar trend is observed for the shear modulus due to its direct relation with the Young's modulus with the equation that described above. A good description of the dependence of both shear and Young's modulus to solute content can be found in [30].

In connection with the microstructural evolution, hardness of the films has been affected by the Cu addition. Figure 3.3 shows the dependence of hardness on the added Cu concentration and temperature. The primary outcomes are; *i) hardness was found to increase with Cu- solute*. Generally, the strongest twin spacing for NT metals has been suggested [29,31] to be originated from length-scale depended deformation mechanism: from the slip transfer across twin boundaries to the dislocation nucleation depended on either softening mechanisms or twin boundary migration. Many studies suggested an optimum for twin boundary spacing is ~10nm, and below that strengthening effect diminishes and enhancement on the ductility comes into play [29]. In our study, however, the highest hardness observed for 5 nm twin spacing for the 2.47 at.% Cu film. At that concentration level, the hardness increased from 1.90±0.2 GPa (pure NT silver) to 2.47±0.2 GPa. This increase may be explained by the atomistic simulations [13] in such a way that the optimum twin boundary spacing for the onset of softening NT metals and the maximum strength depend on the grain size and the stress fields originating from the added solute atoms: the smaller the grain size, the higher the solute stress fields, the smaller the twin boundary spacing and the harder the material. Similar results have been published for the NT Cu- Al alloys [21]. Furthermore, if we will calculate the yield stress

which is assumed as a fraction of hardness (*H/3*), we can define the yield stress as a combination of the frictional stress and incremental strengthening contributions such as dislocation density, solid solution hardening, precipitation hardening and grain boundary strengthening (Hall-Petch). In this approach, one can easily find that the strengthening can arise from the grain boundary strengthening and solute hardening even for the twin spacings below optimum. *ii) the hardness of the films decreases with increasing temperature*. Above 200 ˚C each film shows a dramatic decrease in hardness comparing to the one at room temperature. Here, we can assume ~200 ˚C is a threshold value of mechanical strength. The reduction in hardness at 400 ˚C is around of 60-80 % for all films regardless of being Cu-solute strengthened or not, which is align with the results reported previously via in situ TEM experiments under compression [12, 28].

Apparent activation energy analysis was applied by following the similar protocol as discussed in our previous work. Figure 3.4 shows temperature-dependent activation energies of the Ag-Cu solute solution strengthened alloys. Owing to the stress dependence of the activation energy, the constant stress approach was applied to calculate activation energies [27]. The stress levels used to calculate strain rate were ~0.75 GPa ~for the temperatures 25 to 200 ˚C and ~0.35 GPa or low for the temperatures 300 and 400 ˚C. Therefore, only the low temperature (25-200 ˚C) values were used in the activation energy analysis. The calculated activation energies lie on between 30-40 kJ/mol, comparable similar to our previous results (Chapter 2). The NT Ag films with high Cu addition show higher activation energy than pure NT Ag. Thus higher energy was required to deform films with high solute content. The detailed solute concentration dependence of activation energy is shown in Figure 4. The activation energy increased

with solute concentration, from 26 kJ/mol to 36 kJ/mol with 2.45 at.% Cu addition. The reports in the literature presenting evidence for diffusion-controlled deformation requires much higher activation energies (~100 kJ/mol) [32] than that of calculated here. Therefore, diffusion-controlled mechanisms have no direct bearing on the deformation behavior of interest here. After ruling out the diffusion-controlled mechanisms as the dominant controlling mechanism in our samples, we consider next the possibility of dislocation activities. Recently, both atomistic [9,10,13] and in-situ indentation experiments [12,33] showed the possible deformation mechanisms in NT metals. Mainly, they reported that the deformation behavior proceeds in the following sequence: (a) detwinning, (b) dislocation nucleation, (c) dislocation propagation and (d) finally grain growth at large strains. Here, the deformation mechanism that has the highest activation energy -with respect to calculated value- becomes the rate controlling mechanism. Since the required stress for detwinning is too low in comparison to that for the partial dislocation nucleation and these mechanisms can be considered to be series, we obtain an apparent activation energy value that matches closely with the dislocation nucleation ~ 50 kJ/mol [34]. These observations are also consistent with our previous experimental and atomistic studies [9, 28].

In summary, a high-temperature nanoindentation study was performed on the NT silver films with various Cu additions. It was found that the Cu addition decreased both grain size and twin boundary spacing, i.e. 5 nm for all NT Ag-Cu alloys. The maximum hardness achieved at the highest solute content (2.45 at.%) film, ~20% higher than the pure NT Ag. Similar to the hardness, shear modulus also increased by Cu addition. The apparent activation energies extracted from the load vs. depth tests at the temperature

range of 25 – 200 ˚C. The calculated activation energies matched well with dislocation-nucleation dependent plasticity for silver inferring it to be the rate-controlling deformation mechanism.

This work was supported by the U.S. Department of Energy (DOE), Office of Science, Basic Energy Sciences, Materials Science and Engineering Division. The research was performed at the Ames Laboratory, which is operated for the U.S. DOE by Iowa State University under contract # DE-AC02-07CH11358

## References

[1] L. Lu, X. Chen, X. Huang, K. Lu, Revealing the maximum strength in nanotwinned copper., Science. 323 (2009) 607–10. doi:10.1126/science.1167641.

[2] J.R. Greer, Nanotwinned metals: It's all about imperfections., Nat. Mater. 12 (2013) 689–90. doi:10.1038/nmat3721.

[3] L. Sun, X. He, L. Zhu, J. Lu, Two softening stages in nanotwinned Cu, (2014). http://www.tandfonline.com/doi/full/10.1080/14786435.2014.977368#tabModule (accessed January 31, 2015).

[4] O. Anderoglu, A. Misra, H. Wang, F. Ronning, M.F. Hundley, X. Zhang, Epitaxial nanotwinned Cu films with high strength and high conductivity, Appl. Phys. Lett. 93 (2008) 10–13. doi:10.1063/1.2969409.

[5] M. A. Meyers, A. Mishra, D.J.J. Benson, Meyers M.A., Mishra A., B. D.J., Mechanical properties of nanocrystalline materials, Prog. Mater. Sci. 51 (2006) 427–556. doi:10.1016/j.pmatsci.2005.08.003.

[6] B. Chen, K. Lutker, S.V. Raju, J. Yan, W. Kanitpanyacharoen, J. Lei, et al., Texture of nanocrystalline nickel: probing the lower size limit of dislocation activity., Science. 338 (2012) 1448–51. doi:10.1126/science.1228211.

[7] K. Lu, L. Lu, S. Suresh, Strengthening materials by engineering coherent internal boundaries at the nanoscale., Science. 324 (2009) 349–52. doi:10.1126/science.1159610.

[8] N. Li, J. Wang, A. Misra, X. Zhang, J.Y. Huang, J.P. Hirth, Twinning dislocation multiplication at a coherent twin boundary, Acta Mater. 59 (2011) 5989–5996. doi:10.1016/j.actamat.2011.06.007.

[9] V. Borovikov, M.I. Mendelev, A.H. King, R. LeSar, Effect of stacking fault energy on mechanism of plastic deformation in nanotwinned FCC metals, Model. Simul. Mater. Sci. Eng. 23 (2015) 055003. doi:10.1088/0965-0393/23/5/055003.

[10] V. Borovikov, M.I. Mendelev, A.H. King, R. LeSar, Effects of Schmid factor and slip nucleation on deformation mechanism in columnar-grained nanotwinned Ag and Cu, J. Appl. Phys. 117 (2015) 085302. doi:10.1063/1.4913381.

[11] D. Jang, X. Li, H. Gao, J.R. Greer, Deformation mechanisms in nanotwinned metal nanopillars., Nat. Nanotechnol. 7 (2012) 594–601. doi:10.1038/nnano.2012.116.

[12] D. Bufford, Y. Liu, J. Wang, H. Wang, X. Zhang, In situ nanoindentation study on plasticity and work hardening in aluminium with incoherent twin boundaries., Nat. Commun. 5 (2014) 4864. doi:10.1038/ncomms5864.

[13] X. Li, Y. Wei, L. Lu, K. Lu, H. Gao, Dislocation nucleation governed softening and maximum strength in nano-twinned metals., Nature. 464 (2010) 877–80. doi:10.1038/nature08929.

[14] L. Sun, X. He, L. Zhu, J. Lu, Two softening stages in nanotwinned Cu, Philos. Mag. 94 (2014) 4037–4052. doi:10.1080/14786435.2014.977368.

[15] K. Edalati, D. Akama, A. Nishio, S. Lee, Y. Yonenaga, ScienceDirect Influence of dislocation – solute atom interactions and stacking fault energy on grain size of single-phase alloys after severe plastic deformation using high-pressure torsion, Acta Mater. 69 (2014) 68–77. doi:10.1016/j.actamat.2014.01.036.

[16] G.P.M. Leyson, W. Curtin, L.G. Hector, C.F. Woodward, Quantitative prediction of solute strengthening in aluminium alloys., Nat. Mater. 9 (2010) 750–755. doi:10.1038/nmat2813.

[17] T.J. Rupert, J.C. Trenkle, C. A. Schuh, Enhanced solid solution effects on the strength of nanocrystalline alloys, Acta Mater. 59 (2011) 1619–1631. doi:10.1016/j.actamat.2010.11.026.

[18] R.L. Fleischer, Substitutional solution hardening of copper, Acta Metall. 14 (1966) 1867–1868. doi:10.1016/0001-6160(66)90045-9.

[19] P. Jax, P. Kratochvil, P. Haasen, Solid solution hardening of gold and other f.c.c. single crystals, Acta Metall. 18 (1970) 237–245. doi:10.1016/0001-6160(70)90029-5.

[20] A. Varschavsky, E. Donoso, Order strengthening in α-Cu-Al alloys as influenced by grain size and solute content, Mater. Sci. Eng. A. 101 (1988) 231–240. doi:10.1016/0921-5093(88)90070-6.

[21] P. Zhang, J.Y. Zhang, J. Li, G. Liu, K. Wu, Y.Q. Wang, et al., Combined effect of texture and nanotwins on mechanical properties of the nanostructured Cu and Cu–Al films prepared by magnetron sputtering, J. Mater. Sci. 50 (2014) 1901–1907. doi:10.1007/s10853-014-8753-7.

[22] W.C. Oliver, G.M. Pharr, experiments, (1992).

[23] G.M. Pharr, D.L. Callahan, S.D. McAdams, T.Y. Tsui, S. Anders, A. Anders, et al., Hardness, elastic modulus, and structure of very hard carbon films produced by cathodic-arc deposition with substrate pulse biasing, Appl. Phys. Lett. 68 (1996) 779. doi:10.1063/1.116530.

[24] G.M. Pharr, Measurement of mechanical properties by ultra-low load indentation, Mater. Sci. Eng. A. 253 (1998) 151–159. doi:10.1016/S0921-5093(98)00724-2.

[25] W.C. Oliver, G.M. Pharr, Measurement of hardness and elastic modulus by instrumented indentation: Advances in understanding and refinements to methodology, J. Mater. Res. 19 (2004) 3–20. doi:10.1557/jmr.2004.19.1.3.

[26] J.R. Trelewicz, C. A. Schuh, Hot nanoindentation of nanocrystalline Ni–W alloys, Scr. Mater. 61 (2009) 1056–1059. doi:10.1016/j.scriptamat.2009.08.026.

[27] R. Goodall, T.W. Clyne, A critical appraisal of the extraction of creep parameters from nanoindentation data obtained at room temperature, Acta Mater. 54 (2006) 5489–5499. doi:10.1016/j.actamat.2006.07.020.

[28] H. Zhang, J. Geng, R.T. Ott, M.F. Besser, M.J. Kramer, Effect of Temperature on the Nano/Microstructure and Mechanical Behavior of Nanotwinned Ag Films, Metall. Mater. Trans. A. 46 (2015) 4078–4085. doi:10.1007/s11661-015-3028-8.

[29] R.T. Ott, J. Geng, M.F. Besser, M.J. Kramer, Y.M. Wang, E.S. Park, et al., Optimization of strength and ductility in nanotwinned ultra-fine grained Ag: Twin density and grain orientations, Acta Mater. 96 (2015) 378–389. doi:10.1016/j.actamat.2015.06.030.

[30] Z. Wu, H. Bei, G.M. Pharr, E.P. George, ScienceDirect Temperature dependence of the mechanical properties of equiatomic solid solution alloys with face-centered cubic crystal structures, 81 (2014) 428–441. doi:10.1016/j.actamat.2014.08.026.

[31] Y. Kulkarni, R.J. Asaro, Are some nanotwinned fcc metals optimal for strength, ductility and grain stability?, Acta Mater. 57 (2009) 4835–4844. doi:10.1016/j.actamat.2009.06.047.

[32] H. Conrad, J. Narayan, On the grain size softening in nanocrystalline materials, Scr. Mater. 42 (2000) 1025–1030. doi:10.1016/S1359-6462(00)00320-1.

[33] D. Bufford, H. Wang, X. Zhang, High strength, epitaxial nanotwinned Ag films, Acta Mater. 59 (2011) 93–101. doi:10.1016/j.actamat.2010.09.011.

[34] T. Filleter, S. Ryu, K. Kang, J. Yin, R.A. Bernal, Nucleation-Controlled Distributed Plasticity in Penta-twinned Silver Nanowires, (2012) 1–8. doi:10.1002/smll.201200522.

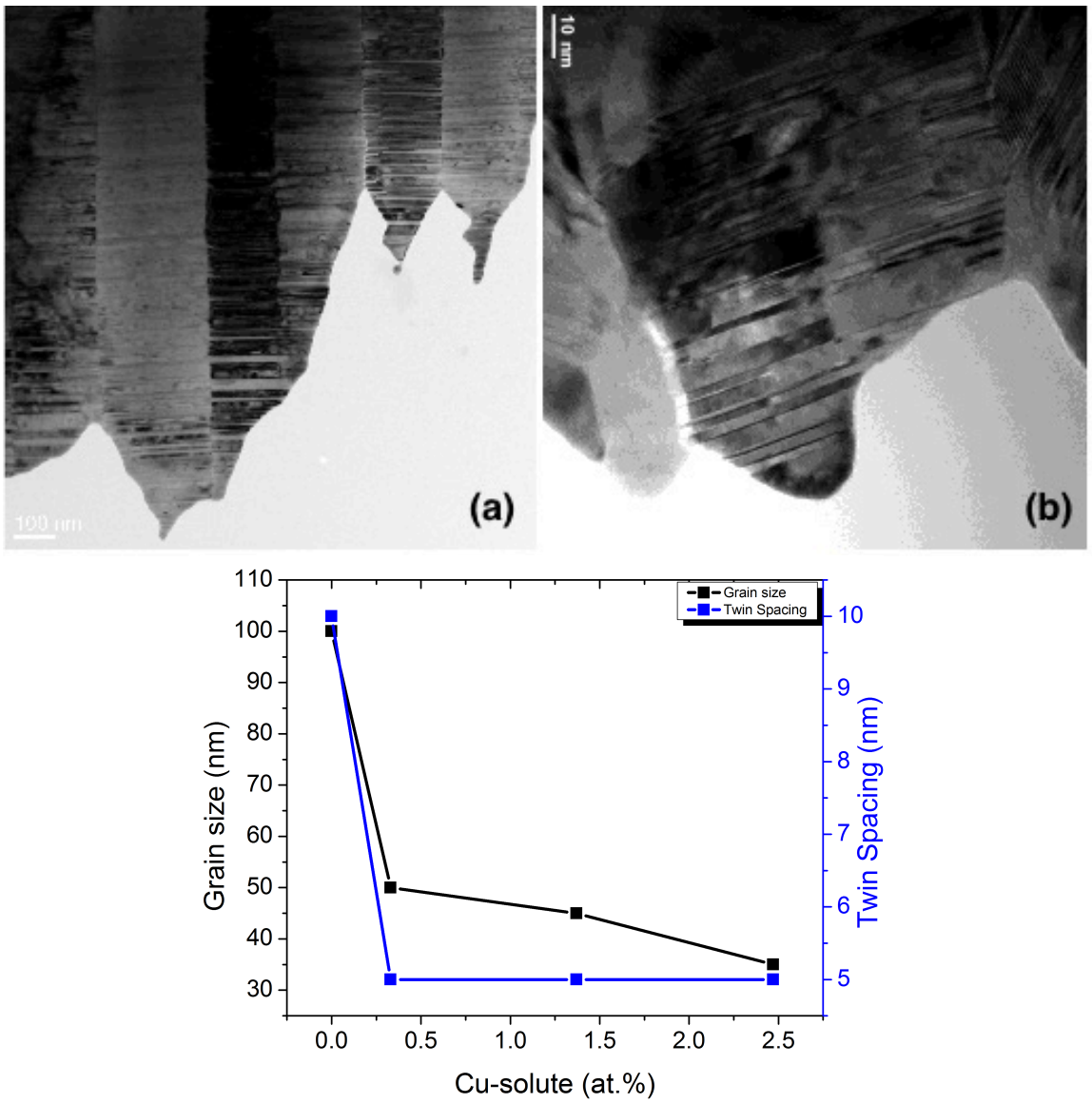


Figure 3.1. Cross sectional TEM images of (a) pure nanotwinned silver, (b) Ag- 2.45 at.% Cu alloy, and (c) variations of grain size and twin spacing with respect to Cu solute concentration.

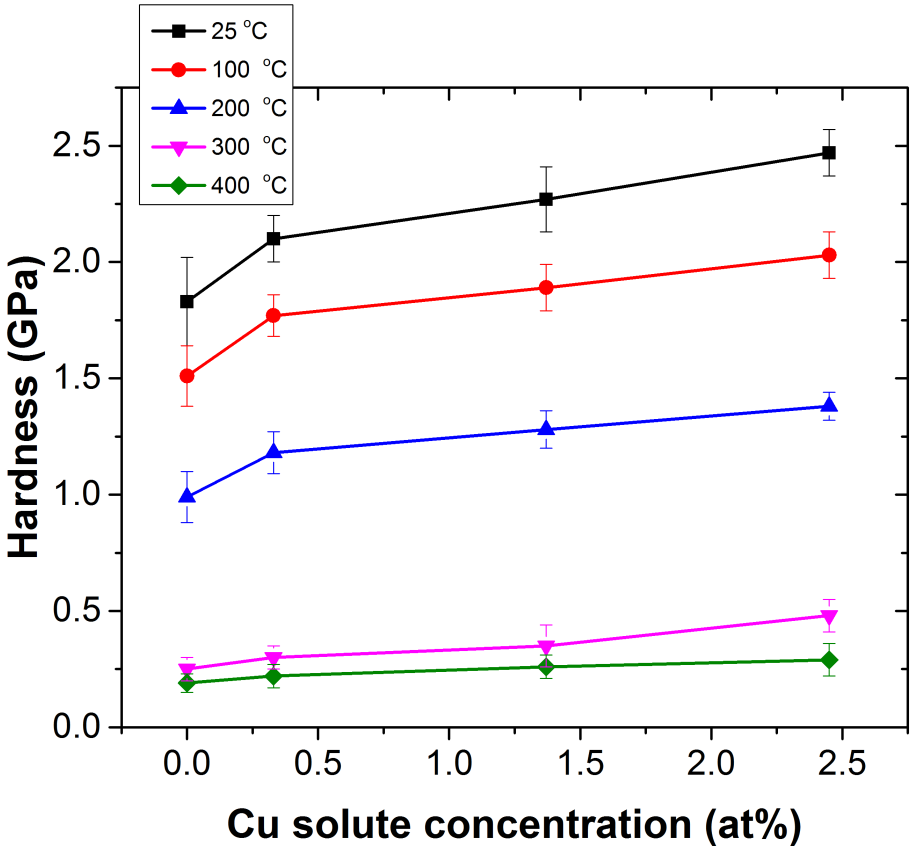


Figure 3.2. Hardness evolution of nanotwinned Ag films with different solute concentrations at various temperatures.

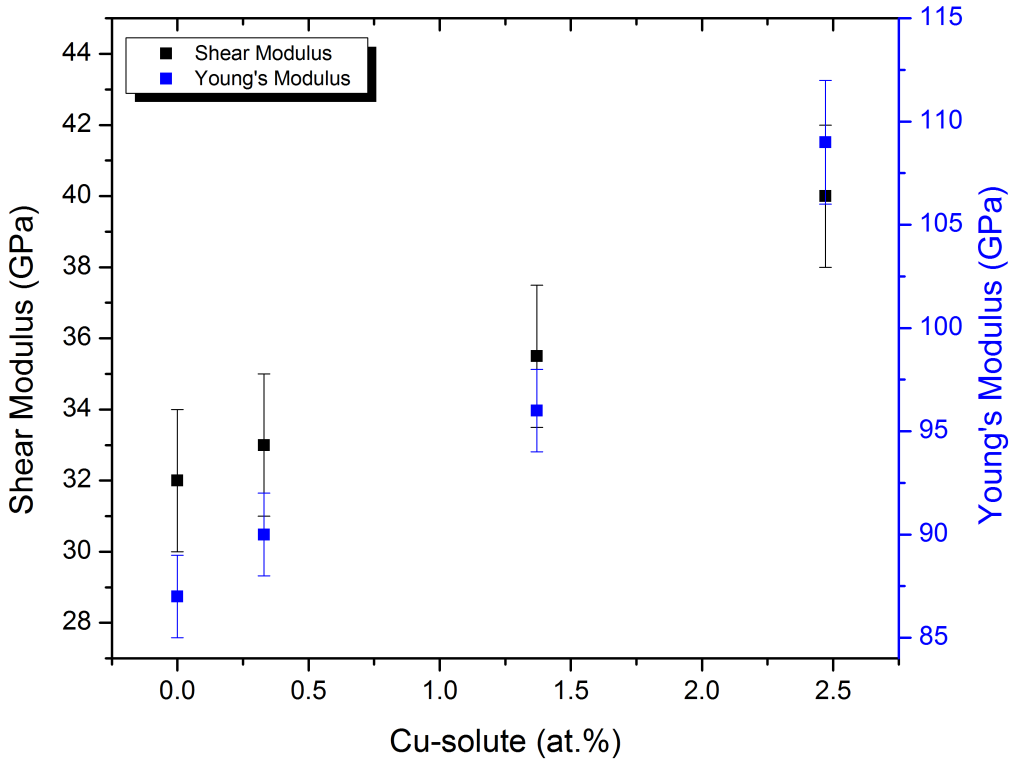


Figure 3.3. Change on shear and Young's modulus with Cu-solute concentration at room temperature.

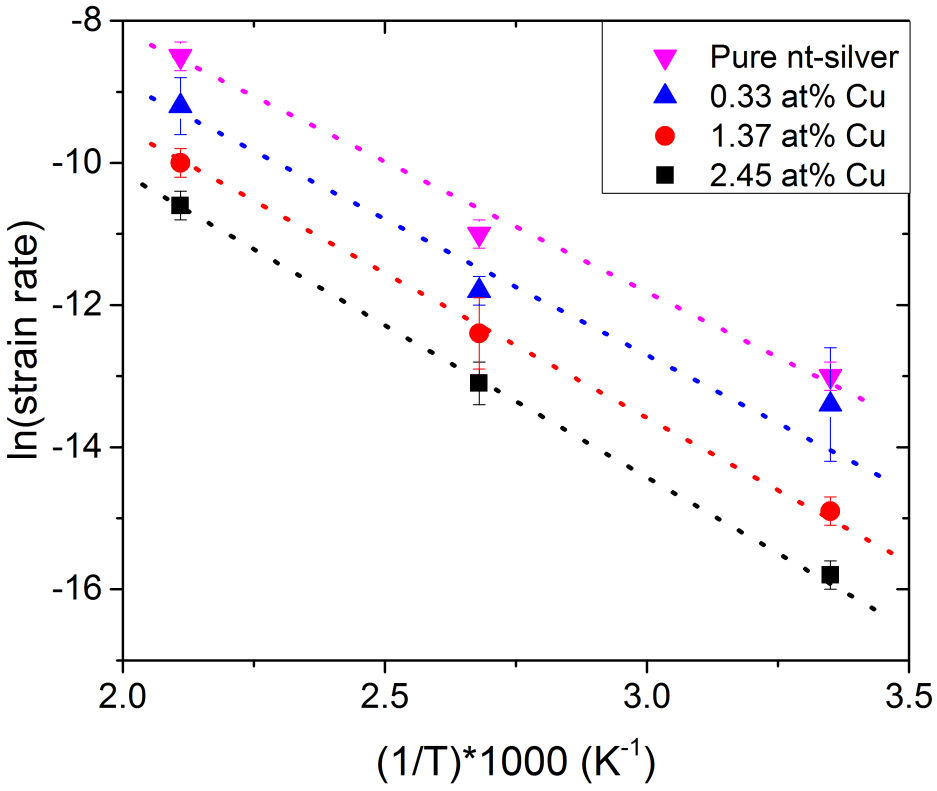


Figure 3.4a. Calculation of activation energies for Ag-Cu alloys at various temperatures

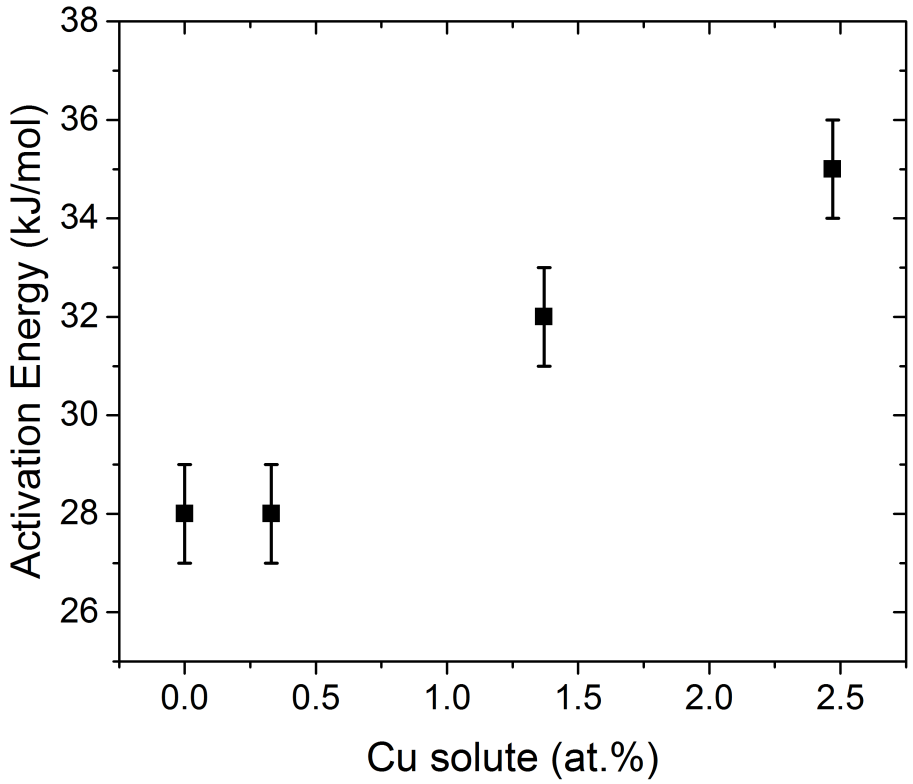


Figure 3.4b. The change of activation energies with Cu solute concentration.

# CHAPTER 4. STRAIN RATE SENSITIVITY AND ACTIVATION VOLUME ANALYSIS OF NANOTWINNED Ag-Al FILMS VIA NANOINDENTATION

A paper to be submitted to Scripta Materialia

H. Yavas[1,2], J. Geng, R. T. Ott[1], M.F. Besser[1], K. Rajan[3], and R. LeSar*[1,2]

[1] Division of Materials Sciences and Engineering, Ames Laboratory, Ames, IA 50011

[2] Department of Materials Science and Engineering, Iowa State University, Ames, IA 50011

[3] Department of Materials Design and Innovation, State University of New York at Buffalo, Buffalo, NY 14260

* To whom all correspondence should be addressed.

Email: lesar@iastate.edu

## Abstract

In this study, nanoindentation tests were conducted on nanotwinned Ag-0.68 at.% Al under different strain rates at room temperature. Results show that the nanomechanical properties of nanotwinned films depend remarkably on the strain rate and twin density. Highly twinned samples showed enhanced strain rate sensitivity, which increases mildly with an activation volume of approximately $15b^3$. The strain rate sensitivity and activation volume analysis suggest that the Shockley partial dislocation nucleation/emission from twin or grain boundaries are the dominant mechanisms, whereas the dislocation forest interactions were ruled out.

Nanotwinned (NT) metals have been widely studied in recent years due to their superior thermal/mechanical properties and unusual deformation behavior. The observed strength can exceed that estimated with a Hall-Petch model, and it reflects the ability of additional barriers in the nanostructure, i.e. twin boundaries, which act to stop or slow down the motion of dislocations [1,2]. Conventional dislocation pile-up mechanisms cannot explain the deformation behavior of the NT metals. Instead, twin boundary and partial dislocation-mediated mechanisms become more important at that length scale [3–6]. As twin spacing and grain size reach the nanometer range, deformation becomes dominated by alternative processes such as Shockley partial nucleation and emission [7–9], twin boundary migration or detwinning [10]. Moreover, recent computational [4,11] and experimental [12–14] studies revealed that the twin/grain orientation and texture [14,15] has a significant effect on both mechanical and thermal performance. Our previous study showed that mechanical properties of the NT silver films exhibited strong {111}-texture dependency, in which highly textured films showed nearly two times the improved hardness values compared to low texture (randomly oriented films) films [12,14]. Obviously, one can expect such a texture effect, but it is highly relevant to quantify its influence on mechanical performance and deformation physics to design materials for critical applications. From that perspective, the loading or strain rate sensitivity, and the activation volume are quantitative fingerprints for revealing dominant deformation mechanisms [16–18]. There are only a few experimental results indicating that the strain rate sensitivity of NT metals shows behavior to nanocrystalline metals, in which they show elevated m compared to coarse-grained and ultrafine-grained counterparts [19,20]. Furthermore, experimental studies suggest that the activation

volume of conventional coarse-grained materials is on the order of approximately $1000b^3$, where b is the magnitude of the perfect dislocation Burgers vector; while the corresponding value for nanocrystalline metals is nearly two orders of magnitude lower than that [17,21]. Although experiments employing loading/strain rate changes are very beneficial in revealing dominant deformation mechanisms, there is very limited data on both strain rate sensitivity and the activation volume of NT metals. A systematic study from low to high twin density would, therefore, be particularly useful not only for extracting activation parameters but also for revealing the effect of the twin structure on deformation kinetics. In this study, we quantitatively report the twin density and orientation effects on the hardness, strain rate sensitivity and activation volume of NT Ag-0.68 at.% Al films using a depth-sensing nanoindentation technique.

NT Ag films with 0.68 at.% Al solute (NT Ag-Al) content of various twin densities were prepared by physical vapor deposition using magnetron sputtering (Kurt J. Lesker CMS-18 System) on a liquid nitrogen cooled (100) oriented Si wafers. The operation power was arranged to 300 W for Ag target and to 60 W for Al target. Due to the non-uniform deposition rate of the target materials onto the Si substrate, various films can be prepared with different microstructures. A representative image that shows how the position of the substrate affected the microstructure of the prepared films is shown in Figure 4.1a. The locations of the samples are designated by the circles (Circle 1-C1, Circle 2- C2, Circle 3-C3 and Circle 4- C4) that indicate the change of the deposition rate in the sputtering chamber where the C1-circle indicates highest twin density (also highest deposition rate), while the C4-circle corresponds to lowest twin density (lowest deposition rate). The details of the sample preparation step were previously explained

elsewhere [12,14]. The thin cross-sectional specimens were examined using an FEI Tecnai G(2) transmission electron microscopy (TEM). The samples were prepared by wedge-polishing followed by dual-ion-beam milling. The TEM images of the as-deposited highly twinned (C1) NT Ag-Al film are shown in Figure 4.1b and Figure 4.1c. In Figure 4.1b, the cross-sectional TEM image indicates a high-density of parallel twin boundaries aligned parallel to the growth direction (which is normal to the Si wafer) with average twin boundary spacing of approximately 5 nm. Figure 4.1c shows the planar view of the same C1 sample. The average columnar grain size is 55 nm, which is far smaller than that of pure NT Ag.

In preparation for the nanoindentation experiments, the samples were glued onto stainless steel sample holders using standard cyanoacrylate super glue. Indentation experiments were conducted at room temperature using a MicroMaterials Nanotest Platform (MicroMaterials Ltd., UK) using a Berkovich diamond tip. A continuous stiffness measurement technique was used during indentation. A quartz calibration sample was used to calibrate the equipment. Upon calibration, the apex of the Berkovich tip was estimated to have a radius of ~50 nm. A wide range of constant loading rate indentations was performed: 0.01, 0.05, 0.1, 0.3, 0.5, 0.8 and 1 mN/s. The loading sequence was as follows; first, a tip was brought into contact with the sample and indented at a constant loading rate until the force level reached a maximum force of 20 mN. Then, the load was held constant at that maximum value for 20 s. Finally, the applied load was decreased sequentially to 10% of the maximum load. Here, the load was held constant again for 60 s, and the fluctuation on the depth was recorded for further drift calculation. Thermal drift maintained to $<0.1$ nm $s^{-1}$ in all experiments; assuming a

constant drift rate throughout one indentation experiment as well as for machine compliance. The Oliver-Pharr method [22] was used to calculate hardness (H) and Young's modulus from load-depth hysteresis. The strain rates were calculated using the following equation:

$$\dot{\varepsilon} = \frac{1}{h}\frac{\partial h}{\partial t} = \frac{1}{2}\left(\frac{1}{P}\frac{\partial P}{\partial t}\right) \quad , \tag{4.1}$$

where h is the indentation depth, t is time and P is applied load. Therefore, the strain rate values can easily be calculated from displacements, which is typically equal to half of the loading rates. For each strain rate, at least ten indents were made with a spacing of 200 μm between one another. Using the strain rate and hardness, the strain rate sensitivity, *m,* is defined by the slope of the double logarithmic plot of hardness and strain rate under isothermal conditions [23]:

$$m = \frac{\partial \ln H}{\partial \ln \dot{\varepsilon}} \quad , \tag{4.2}$$

Before analyzing the activation volume and strain rate sensitivity, Young's modulus values were examined to check their consistency with literature values to validate the indentation procedure. From the nanoindentation load-displacement hysteresis, the Young's modulus values are calculated from the reduced modulus. The reduced modulus, $E_R$, can be extracted from the unloading portion of the hysteresis that is a composite value of the elastic properties of the NT Ag-Al samples and the diamond indenter tip:

$$\frac{1}{E_R} = \frac{(1+\nu_d^2)}{E_d} + \frac{(1+\nu_f^2)}{E_f} \quad , \tag{4.3}$$

where $E_d$ is the Young's modulus of the diamond indenter (1138 GPa), $E_f$ is the Young's modulus of the sample (film), $\nu_d^2$ is the square of Poisson's ratio of the diamond indenter tip (0.08) and $\nu_f^2$ is the square of the Poisson's ratio of the sample (assumed as 0.35). Figure 4.2 shows the representative Young's modulus values of NT Ag-Al of C1 samples at all strain rates. The data point shows the mean value of at least 10 indentations and the error bar represents the standard deviation. The modulus values are independent of the strain rates. Therefore we can exclude experimental uncertainties or errors related to strain rates. The average Young's modulus values for C1 samples is 110 ±7 GPa for all strain rates. The similar trend is also observed for C2, C3 and C4 samples and we thus conclude that the experimental error is significant in hardness measurements.

To eliminate indentation size and substrate effects on measured mechanical properties, we first determine the depth dependence of the hardness. Figure 4.3a shows the hardness variation at different indentation penetration depths. The hardness values reach a plateau around ~400 nm, therefore, in the rest of the experiments we keep the indentation depth at least ~500 nm to eliminate possible substrate effects while maintaining depth size to be at least 10% of the total thickness of the samples which is ~50 μm. Figure 4.3b shows the average hardness of the NT Ag-Al samples for the constant loading rate of 0.5 mN/s, and the hardness increases with increasing twin density. This observation agrees with our previous study on the effect of texture on mechanical properties in which highly twinned samples show higher hardness [14]. For the highly twinned samples (C1) the hardness is 2.45 ±0.2 GPa, which is a factor of 1.3 greater than the samples with lower twin density (C4). Figure 4.4a shows the hardness variations as a function of loading rate. The hardness values increase with increasing twin

density at every loading rate, indicating the strengthening effect with a maximum hardness of 2.54±0.15 GPa for the highly twinned C1 sample. From these results, it can be suggested that the high hardness of highly twinned NT Ag-Al films originates from the effective blockage of dislocation motion by a high density of <111>-oriented films.

To reveal the rate controlling mechanisms, an activation volume V* of the thermally activated mechanisms is given by:

$$V^* = \sqrt{3}kT\left(\frac{\partial \ln \dot{\varepsilon}}{\partial \sigma}\right) = 3\sqrt{3}kT\left(\frac{\partial \ln \dot{\varepsilon}}{\partial H}\right) \quad , \tag{4.4}$$

where k is the Boltzman constant, T is the temperature, $\dot{\varepsilon}$ is the strain rate, $\sigma$ is the flow stress and H is the hardness- here assuming $H=3\sigma$. Using the above equation (Eq.4.4), the activation volume for the NT Ag-Al alloys are calculated and then normalized by the magnitude of the Burgers vector of perfect dislocation in Ag (0.289 nm) to compare with the literature values. The calculated m and activation volumes of the samples are given in Figure 4.4b. By fitting the experimental data (hardness vs. strain rate), the calculated activation volumes are $11b^3$ for highly twinned C1 samples and $18b^3$ for lower twin density C4 samples, respectively. The rest of the data (C2 and C3) lies between these two extreme values, which are $13b^3$ for C2 samples and $15b^3$ for C3 samples, which are essentially similar. For all cases, it is clear that the calculated activation volumes are very small compared to bulk FCC metals ($100\text{-}1000b^3$) where forest dislocation interactions control the deformation. In nano-grained materials, the activation volume is known to be decreased as a result of the changes in dislocation nucleation sources: from conventional Frank-Read sources to grain boundary mediated deformation mechanisms [17,24]. Here,

the plasticity is accommodated by the dislocation grain boundary interactions. For NT materials, plasticity is governed by twin boundaries, and thus it is expected to observe a reduced V*. The decrease on the activation volumes from ~1000$b^3$ to ~10$b^3$ indicates that intra-granular dislocation interactions are suppressed through grain refinement and the presence of the twin boundaries. Such small activation volumes suggest that the rate determining or the dislocation nucleation controls dominant deformation mechanism in NT Ag-Al films. Similar to the activation volume, V*, *m* is another important parameter, which enables an understanding of thermally activated plastic deformation. In Figure 4b, it is shown that the values of *m* estimated in the present work (~ 0.03) for all samples are within the range reported in the literature for Ag nanowires [8] and different NT films, such as NT Cu [21,25]. Additionally, *m* is sensitive to the twin density; with increasing twin density the m value slightly increases from 0.023±0.005 to 0.03±0.004. In light of the calculated activation volume and *m* values, several different deformation mechanisms can be proposed, which are: Shockley partial dislocation nucleation from twin boundaries or twin/grain boundary triple junctions [18], channeling of dislocations within twins and detwinning [26,27]. Since the triaxial stress state is active beneath the indenter tip, it is expected that all of the deformation mechanism as mentioned earlier can activate during the indentation.

In conclusion, hardness, strain rate sensitivity, activation volume and related deformation mechanisms of NT Ag- 0.68 at.%Al films were evaluated by controlled load nanoindentation experiments. The highly twinned samples showed higher hardness and strain rate sensitivity than that of samples with lower twin density. The activation volume was also found to be ~15$b^3$ for nearly all samples, which is consistent with experiments

and previously reported activation volumes of partial dislocation nucleation and emission mediated plasticity.

This work was supported by the U.S. Department of Energy (DOE), Office of Science, Basic Energy Sciences, Materials Science and Engineering Division. The research was performed at the Ames Laboratory, which is operated for the U.S. DOE by Iowa State University under contract # DE-AC02-07CH11358.

## References

[1] X. Li, Y. Wei, L. Lu, K. Lu, H. Gao, Dislocation nucleation governed softening and maximum strength in nano-twinned metals., Nature. 464 (2010) 877–880. doi:10.1038/nature08929.

[2] C. Xie, Q.H. Fang, L.X. Li, J.K. Chen, Y.W. Liu, Y.N. Wang, The impact of twin lamella thickness distribution on strength and endurance limit in nanotwinned copper, Mech. Mater. 84 (2015) 91–99. doi:10.1016/j.mechmat.2015.01.017.

[3] Z.X. Wu, Y.W. Zhang, D.J. Srolovitz, Dislocation–twin interaction mechanisms for ultrahigh strength and ductility in nanotwinned metals, Acta Mater. 57 (2009) 4508–4518. doi:10.1016/j.actamat.2009.06.015.

[4] N. Li, J. Wang, A. Misra, X. Zhang, J.Y. Huang, J.P. Hirth, Twinning dislocation multiplication at a coherent twin boundary, Acta Mater. 59 (2011) 5989–5996. doi:10.1016/j.actamat.2011.06.007.

[5] V. Borovikov, M.I. Mendelev, A.H. King, R. LeSar, Effects of Schmid factor and slip nucleation on deformation mechanism in columnar-grained nanotwinned Ag and Cu, J. Appl. Phys. 117 (2015) 085302. doi:10.1063/1.4913381.

[6] T. Zhu, H. Gao, Plastic deformation mechanism in nanotwinned metals: An insight from molecular dynamics and mechanistic modeling, Scr. Mater. 66 (2012) 843–848. doi:10.1016/j.scriptamat.2012.01.031.

[7] D. Bufford, Y. Liu, J. Wang, H. Wang, X. Zhang, In situ nanoindentation study on plasticity and work hardening in aluminium with incoherent twin boundaries., Nat. Commun. 5 (2014) 4864. doi:10.1038/ncomms5864.

[8] T. Filleter, S. Ryu, K. Kang, J. Yin, R.A. Bernal, Nucleation-Controlled Distributed Plasticity in Penta-twinned Silver Nanowires, (2012) 1–8. doi:10.1002/smll.201200522.

[9] R.J. Wagner, L. Ma, F. Tavazza, L.E. Levine, Dislocation nucleation during nanoindentation of aluminum, J. Appl. Phys. 104 (2008) 114311. doi:10.1063/1.3021305.

[10] Y. Liu, N. Li, D. Bufford, J.H. Lee, J. Wang, H. Wang, et al., In Situ Nanoindentation Studies on Detwinning and Work Hardening in Nanotwinned Monolithic Metals, Jom. 68 (2016) 127–135. doi:10.1007/s11837-015-1518-1.

[11] L. Sun, X. He, L. Zhu, J. Lu, Two softening stages in nanotwinned Cu, (2014). http://www.tandfonline.com/doi/full/10.1080/14786435.2014.977368#tabModule (accessed January 31, 2015).

[12] H. Zhang, J. Geng, R.T. Ott, M.F. Besser, M.J. Kramer, Effect of Temperature on the Nano/Microstructure and Mechanical Behavior of Nanotwinned Ag Films, Metall. Mater. Trans. A. 46 (2015) 4078–4085. doi:10.1007/s11661-015-3028-8.

[13] Y.M. Wang, F. Sansoz, T. LaGrange, R.T. Ott, J. Marian, T.W. Barbee, et al., Defective twin boundaries in nanotwinned metals., Nat. Mater. 12 (2013) 697–702. doi:10.1038/nmat3646.

[14] R.T. Ott, J. Geng, M.F. Besser, M.J. Kramer, Y.M. Wang, E.S. Park, et al., Optimization of strength and ductility in nanotwinned ultra-fine grained Ag: Twin density and grain orientations, Acta Mater. 96 (2015) 378–389. doi:10.1016/j.actamat.2015.06.030.

[15] J.C. Ye, Y.M. Wang, T.W. Barbee, a. V. Hamza, Orientation-dependent hardness and strain rate sensitivity in nanotwin copper, Appl. Phys. Lett. 100 (2012) 261912. doi:10.1063/1.4731242.

[16] L. Lu, R. Schwaiger, Z.W. Shan, M. Dao, K. Lu, S. Suresh, Nano-sized twins induce high rate sensitivity of flow stress in pure copper, Acta Mater. 53 (2005) 2169–2179. doi:10.1016/j.actamat.2005.01.031.

[17] Y. Wang, A. Hamza, E. Ma, Temperature-dependent strain rate sensitivity and activation volume of nanocrystalline Ni, Acta Mater. 54 (2006) 2715–2726. doi:10.1016/j.actamat.2006.02.013.

[18] R.J. Asaro, S. Suresh, Mechanistic models for the activation volume and rate sensitivity in metals with nanocrystalline grains and nano-scale twins, Acta Mater. 53 (2005) 3369–3382. doi:10.1016/j.actamat.2005.03.047.

[19] L. Lu, X. Chen, X. Huang, K. Lu, Revealing the maximum strength in nanotwinned copper., Science. 323 (2009) 607–10. doi:10.1126/science.1167641.

[20] Q. Wei, S. Cheng, K.T. Ramesh, E. Ma, Effect of nanocrystalline and ultrafine grain sizes on the strain rate sensitivity and activation volume: Fcc versus bcc metals, Mater. Sci. Eng. A. 381 (2004) 71–79. doi:10.1016/j.msea.2004.03.064.

[21] M. Dao, L. Lu, Y.F. Shen, S. Suresh, Strength, strain-rate sensitivity and ductility of copper with nanoscale twins, Acta Mater. 54 (2006) 5421–5432. doi:10.1016/j.actamat.2006.06.062.

[22] W.C. Oliver, G.M. Pharr, Measurement of hardness and elastic modulus by instrumented indentation: Advances in understanding and refinements to methodology, J. Mater. Res. 19 (2004) 3–20. doi:10.1557/jmr.2004.19.1.3.

[23] B.J. Diak, S. Saimoto, The determination of solute clusters in dilute aluminum alloys using strain rate sensitivity, Mater. Sci. Eng. A. 234-236 (1997) 1019–1022. doi:10.1016/S0921-5093(97)00342-0.

[24] X. Wu, Y.T. Zhu, M.W. Chen, E. Ma, Twinning and stacking fault formation during tensile deformation of nanocrystalline Ni, Scr. Mater. 54 (2006) 1685–1690. doi:10.1016/j.scriptamat.2005.12.045.

[25] Y.F. Shen, L. Lu, M. Dao, S. Suresh, Strain rate sensitivity of Cu with nanoscale twins, Scr. Mater. 55 (2006) 319–322. doi:10.1016/j.scriptamat.2006.04.046.

[26] D. Bufford, Y. Liu, J. Wang, H. Wang, X. Zhang, In situ nanoindentation study on plasticity and work hardening in aluminium with incoherent twin boundaries., Nat. Commun. 5 (2014) 4864. doi:10.1038/ncomms5864.

[27] K.Y. Yu, D. Bufford, C. Sun, Y. Liu, H. Wang, M.A. Kirk, et al., Removal of stacking-fault tetrahedra by twin boundaries in nanotwinned metals., Nat. Commun.4(2013)1377.

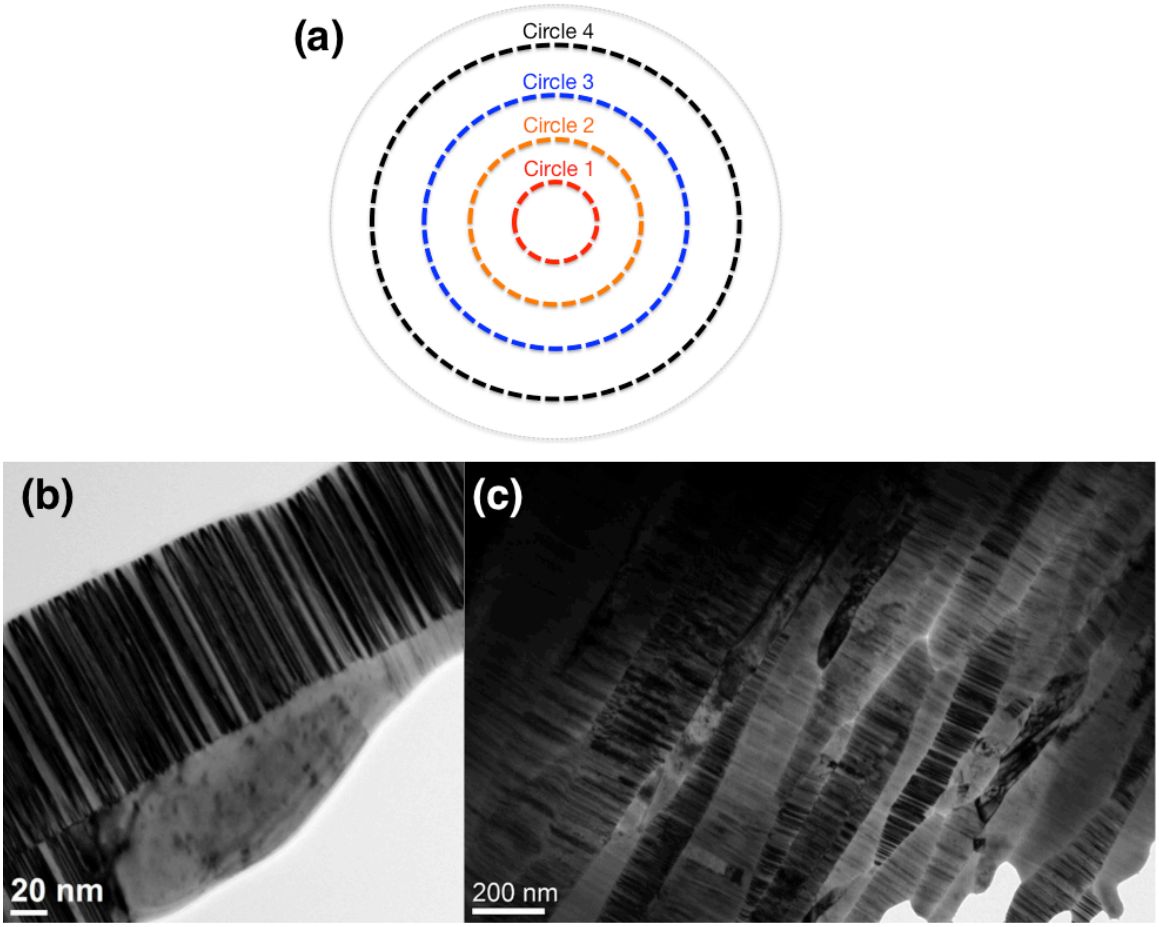


Figure 4.1. (a) Schematic respresentation of the sputtering circles (C1, C2, C3 and C4) ahows the different deposition rates along the sample. (b) and (c) are cross-sectional TEM images of the NT Ag-Al films.

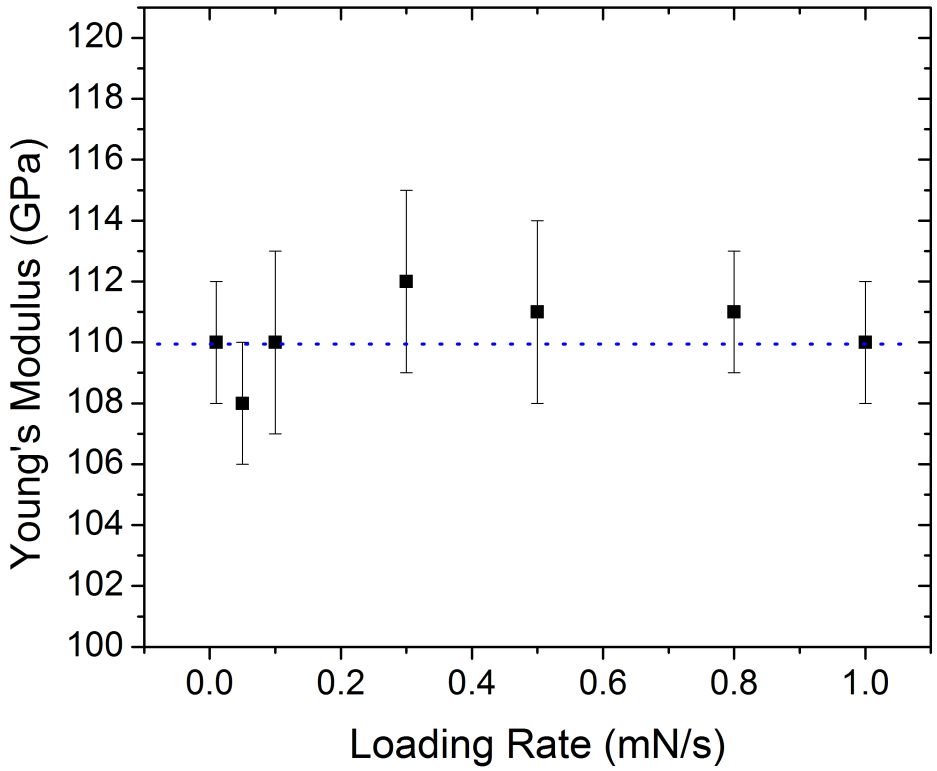


Figure 4.2 Average Young's modulus evolution as a function of deposition rate.

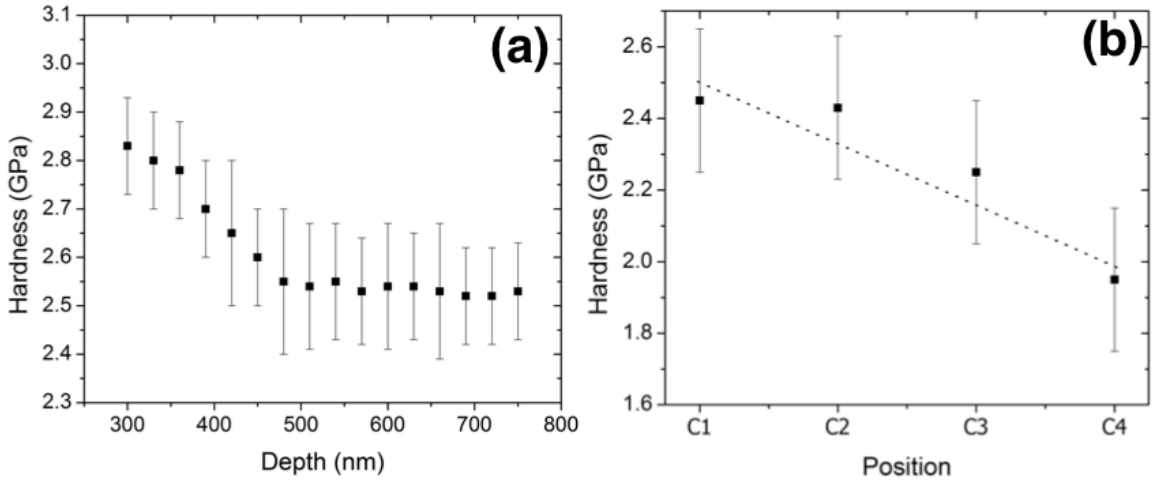


Figure 4.3 (a) Indentation depth dependence of the hardness, (b) Hardness variations of different deposition circles C1, C2, C3 and C4.

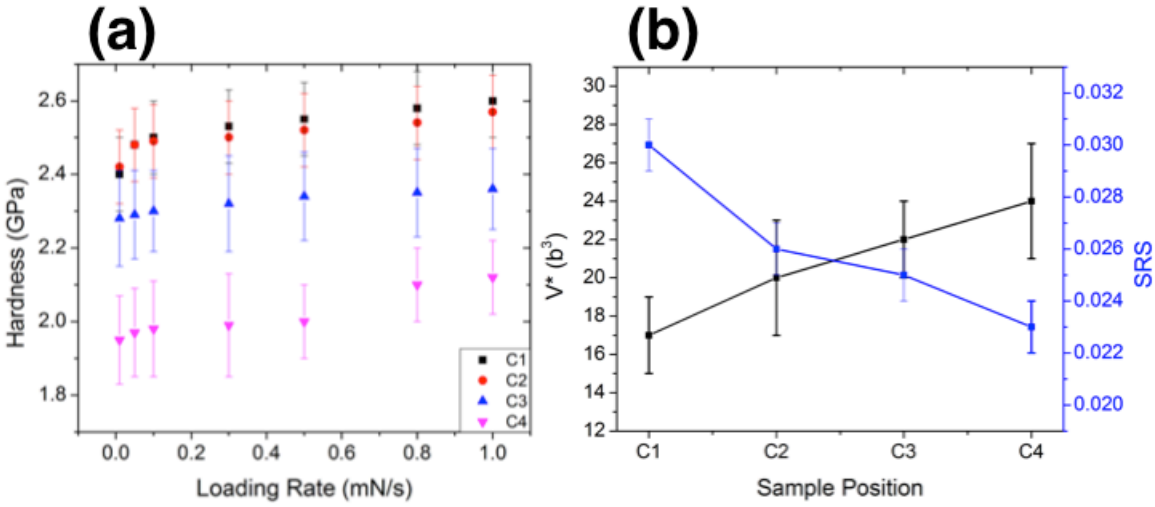


Figure 4.4 (a) Hardness variations deposition circles as a function of loading rate, (b) the strain rate sensitivity (m) and activation volume, V*, calculated as under the assumption that hardness and loading rate are equivalent to stress and strain rate.

# CHAPTER 5. INVESTIGATING THE EFFECT OF NANOTWIN BOUNDARIES ON DISLOCATION NUCLEATION AND PROPAGATION USING PHASE FIELD DISLOCATION DYNAMICS

A paper to be submitted to Scripta Materialia

H. Yavas[1,2], R. LeSar*[1,2]

[1] Division of Materials Sciences and Engineering, Ames Laboratory, Ames, IA 50011

[2] Department of Materials Science and Engineering, Iowa State University, Ames, IA 50011

* To whom all correspondence should be addressed.

Email: lesar@iastate.edu

## Abstract

We present the effects of grain size and twin spacing on partial dislocation nucleation/emission of nanotwinned materials using a phase field dislocation dynamics model that incorporates γ-surface, which is informed by density functional theory. We show that the twin spacing has an influence on the partial dislocation emission. We also revealed that the grain size and twin spacing dependence of the partial dislocation nucleation and emission behavior of NT Ag metals. The nucleation behavior depends heavily on the twin spacing rather than grain size.

**Keywords:** twinning; twin spacing; phase field dislocation dynamics

Due to their superior thermal and mechanical properties and unusual deformation behavior, nanotwinned (NT) metals are one of the leading topics in materials research. Experimental and computational studies have shown that unlike their coarse-grained counterparts, twin boundary [1–10] and partial dislocation-mediated mechanisms [11–16] become dominated at nano-scale twin spacings, i.e. <10 nm [10,17]. Recently, the *in situ* nanoindentation study reported visual deformation steps via transmission electron microscopy [5,18,19]. They observed that deformation starts with detwinning at very low loads and follows by a partial dislocation nucleation as the applied load is reached to some critical value. Additionally, in our previous study, we reported a critical temperature regime regarding microstructural stability of NT Ag films [17]. The mechanical properties of the NT Ag films show a slight decrease (which is unusual compared to nanocrystalline films) for the temperatures up to ~200 ˚C. Interestingly, while grain size increases on order ~1.5, the twin spacing remain constant at 10 nm. This twin boundary dependent microstructural stability raised many questions to elucidate the microstructural aspects of the deformation.

Despite the progress made in determining the deformation mechanisms of NT metals, many questions are still unanswered. For example, first, what approaches to the twin boundary- is it a leading partial or a full dislocation? A full dislocation could result if the grain boundary ledge pops out the trailing partial before the leading partial reaches the twin boundary. Second, how is this interaction affected by grain size? Third, how twin boundary spacing affects the partial dislocation nucleation event?

Molecular dynamics (MD) and density functional theory (DFT) studies have shown that when twinned grains are deformed, the twins itself and grain boundaries can

nucleate partial dislocations and this nucleation event is connected to the stacking fault energy [1,2,20–24]. These computational efforts, however, are known to be limited by very small length and time scales. For instance, in MD the most commonly used grain sizes are below 100 nm and strain rates are very high (~$10^9$/s) compared to real laboratory experiments. On the other hand, some mesoscopic models, such as continuum models or dislocation dynamics, is suitable for larger length scales and time scales than MD or DFT; however, they are not capable of modeling partial dislocation and stacking faults [25,26].

In this study, we suggest using phase field dislocation dynamics (PFDD) model to observe the effect of twin boundary spacing and grain size on the partial dislocation nucleation and emission events in the NT metals. PFDD model predicts the motion and configuration of a dislocation by energy minimization [22,26–30]. To describe the atomistic variables, such as γ-surface parameters and the core energy, the model incorporates the full 3D γ-surface from external DFT calculations into the free energy functional in phase field formulation. The outcome of this model is to predict the most energetically favorable defect and its nucleation and emission for a given material and grain/twin size; which involves strain energy, dislocation core energy and externally applied energy to deform the material. The most significant benefit of the PFDD simulations is to count the dislocation motion for large crystals (model allowed up to micron size grains) over large time scales (1 to several 1000 s). The details of the PFDD formulation can be found in elsewhere [29–31].

In this study, we first examine the partial dislocation nucleation and emission events using the room temperature material constants of Ag, with a grain size of 36.97

nm, containing a single ledge (a perfect dislocation located near the grain boundary). The applied external shear stress is assumed to be 1 GPa, which was suggested as a critical nucleation stress for Ag [23,26,32]. After that, we studied various grain sizes and twin spacing values to observe possible microstructural effects on partial dislocation and stacking fault width evolution.

A schematic illustration of the PFDD simulation cell is shown in Figure 1. We construct a cubic crystal having grain boundaries on all sides, and applied full periodic boundary conditions. Grain boundaries are modeled as impenetrable obstacles. In other words, grain boundaries are not be evolved in the Ginzburg-Landau Equation. A ledge, the red shaded area in Fig 1, is embedded as a partial dislocation nucleation source and has a Burgers vector equal to a perfect edge dislocation. The simulation cell is oriented along [111] slip plane normal and the slip plane is parallel to the z-axis, the slip direction aligns with the x-axis. As discussed in [23,26,32], $x_i$ is the phase field variable. There is one (or more depending on the number of active slip systems) phase field at each grid point in the simulation cell. Each of these phase fields has a real and imaginary component to it. This is because of using a Fourier transform to calculate the elastic strain energy. When we are at the beginning and end of the simulation (or even time step) we are in real space, not Fourier space, and the imaginary component should be zero. However, there is still need to have this imaginary component for transformation into Fourier space. The real and imaginary components of the phase field at each point are all contained in one array, $x_i$. That is because each point has two values: real and imaginary. For example, if we are at the origin (0,0,0), there we have $x_i[0]$ = real component, and $x_i[1]$=imaginary component, both $x_i[0]$ and $x_i[1]$ go with (0,0,0). If we

move one point over, say (1,0,0) then $x_i[2]$ = real component and $x_i[3]$ = imaginary component for (1,0,0). Keeping this model structure in mind, we assign a twin boundary in PFDD simulation by orienting its slip plane of 70.53˚ along the first slip plane, as seen in Fig 1. Since the partial dislocations are linear combinations of the three phase field variables on the active plane, to create a twin boundary we set one phase field variable to be 0.5 or set all three to 1/3. Here, it is worth to mention that when a partial dislocation faces with a twin boundary, it can only energetically interact with the twin boundary. In other words, cross slip or climb mechanisms are not allowed.

During initial steps of the simulation, when nucleation stress is reached to a critical value [23], the leading partial dislocation expands until reaches an energetically favorable state and leaving behind a stacking fault. As the leading partial dislocation evolves in grain interior, the stacking fault width shaded in green color in Figure 2. If the stress level reaches an adequate value and/or grain is large enough [23] a trailing partial dislocation should nucleate with a separate color (red). Figure 2 demonstrates the effect of twin boundary on the evolution of the stacking fault width. It is clearly seen that a twin boundary effectively blocks the dislocation movement. The maximum traveling distance of the partial dislocation is considerably larger than the twinned grains.

In Figure 3, the stacking fault width is showed for NT Ag with different twin boundary spacing values in the range of 4,62 nm to 27.73 nm. To compare the results, we use a metric of $w_{max}$. $w_{max}$ is equal to the maximum size of the stacking fault width and calculated by drawing a straight line from the center of the ledge to the highest point of the extended stacking fault width (maximum point of the green shaded area). The calculated $w_{max}$ values are listed in Table 1.

It should be noted here that the results in the Table 1 are remarkably consistent with the previously reported experimental studies [10,17]. For example, nanoindentation experiments show that above the twin spacing of 10 nm, the hardness of the NT metals (Ag) shows a slight decrease, as seen in the previous chapter. The reduction in the hardness can be considered as resistance against the dislocation motion; therefore, PFDD results are in line with the strengthening trend observed in *in-situ* experiments- where the lowest twin spacing creates higher resistance to the dislocation motion, which lead to strengthening of the material. To observe the net effect of the position of the twin boundary/twin boundary spacing, we normalize the twin spacings (TBS) with the $w_{max}$ $(TBS/w_{max})$: 2.48, 2.09, 1.98 and 1.73, respectively. The smallest normalization factor is found for the largest TBS and increases for the smaller TBS. Indicating that at smaller TBS's evolution of a partial dislocation highly affected by the presence of the twin boundaries, i.e. stress field and backstresses originating from twin boundary. The similar trend is also reported by Hunter et al. [23].

Figure 4 shows the progression of partial dislocations traversing an Ag grain (36.97 nm) while keeping the twin spacing constant. This simulation is inspired by our previous *in-situ* high-temperature TEM study, where we found that at high temperatures (~200 ˚C), twin spacing stays constant regardless of the change of the grain size. Furthermore, we also revealed that in addition to twin stability, the mechanical properties of the NT Ag films showed a slight decrease at similar temperatures. The reduction on the mechanical properties can be related to several factors, such as reduction in the dislocation density, required force dependence on the possible thermally activated processes, change in the activation energy for deformation, etc. To investigate the

isolated net effects of the twin boundaries we created simulation cells with the same twin spacing, i.e. 9.24 nm and changed the grain size. Studied grain sizes are 18.48 nm and 36.97 nm. The energetically favorable positions of the partial dislocations on both grain sizes indicate that the expansion of stacking fault width is independent from the grain size. In both cases, partial dislocations are glide for 3.50 nm. These results can shed light into our previous high-temperature nanoindentation studies that we showed a superior thermal stability and retention in hardness after long annealing. We found that twin spacing of the NT Ag films did not change significantly after annealing which might be the reason of the thermal stability of nanotwins.

In summary, a PFDD model is used to study the effect of twin boundaries on the partial dislocation nucleation and emission in nanoscale crystals under ambient conditions. The results showed that a distance of the closest twin boundary controls the nucleation and emission of a partial dislocation. The twin boundaries impose a backstress, which is, affected the partial dislocation motion. The region $w_{max}$ increases with a twin spacing. Furthermore, we observed that if a partial dislocation nucleated in twinned region, its emission towards to the opposite twin boundary is only dependent on the twin spacing; independent from grain size. These finding may provide valuable insight for explaining superior thermal stability and strength of the nanotwinned metals.

This work was supported by the U.S. Department of Energy (DOE), Office of Science, Basic Energy Sciences, Materials Science and Engineering Division. The research was performed at the Ames Laboratory, which is operated for the U.S. DOE by Iowa State University under contract # DE-AC02-07CH11358. The authors thank Dr.

Irene Beyerlein (UCSB, Dept. of Mechanical Engineering) and Dr. Abigail Hunter (Los Alamos National Laboratory) from Iowa State University for informative discussions.

## References

[1] V. Borovikov, M.I. Mendelev, A.H. King, R. LeSar, Effects of Schmid factor and slip nucleation on deformation mechanism in columnar-grained nanotwinned Ag and Cu, J. Appl. Phys. 117 (2015) 085302. doi:10.1063/1.4913381.

[2] V. Borovikov, M.I. Mendelev, A.H. King, R. LeSar, Effect of stacking fault energy on mechanism of plastic deformation in nanotwinned FCC metals, Model. Simul. Mater. Sci. Eng. 23 (2015) 055003. doi:10.1088/0965-0393/23/5/055003.

[3] Y. Zhu, Z. Li, M. Huang, Y. Liu, Strengthening mechanisms of the nanolayered polycrystalline metallic multilayers assisted by twins, Int. J. Plast. 72 (2015) 168–184. doi:10.1016/j.ijplas.2015.05.014.

[4] N.K. Kumar, B. Roy, J. Das, Effect of twin spacing, dislocation density and crystallite size on the strength of nanostructured α-brass, J. Alloys Compd. 618 (2015) 139–145. doi:10.1016/j.jallcom.2014.08.131.

[5] D. Bufford, Y. Liu, J. Wang, H. Wang, X. Zhang, In situ nanoindentation study on plasticity and work hardening in aluminium with incoherent twin boundaries., Nat. Commun. 5 (2014) 4864. doi:10.1038/ncomms5864.

[6] V. Yamakov, D. Wolf, S.R. Phillpot, H. Gleiter, Dislocation-dislocation and dislocation-twin reactions in nanocrystalline Al by molecular dynamics simulation, Acta Mater. 51 (2003) 4135–4147. doi:10.1016/S1359-6454(03)00232-5.

[7] J. Wang, X. Zhang, Twinning effects on strength and plasticity of metallic materials, MRS Bull. 41 (2016) 274–281. doi:10.1557/mrs.2016.67.

[8] N. Li, J. Wang, A. Misra, X. Zhang, J.Y. Huang, J.P. Hirth, Twinning dislocation multiplication at a coherent twin boundary, Acta Mater. 59 (2011) 5989–5996. doi:10.1016/j.actamat.2011.06.007.

[9] N.M. Heckman, L. Velasco, A.M. Hodge, Influence of Twin Thickness and Grain Size on the Tensile Behavior of Fully Nanotwinned CuAl Alloys , Adv. Eng. Mater. 18 (2016) 918–922. doi:10.1002/adem.201500496.

[10] R.T. Ott, J. Geng, M.F. Besser, M.J. Kramer, Y.M. Wang, E.S. Park, et al., Optimization of strength and ductility in nanotwinned ultra-fine grained Ag: Twin density and grain orientations, Acta Mater. 96 (2015) 378–389. doi:10.1016/j.actamat.2015.06.030.

[11] N.P. Daphalapurkar, K.T. Ramesh, Orientation dependence of the nucleation and growth of partial dislocations and possible twinning mechanisms in aluminum, J. Mech. Phys. Solids. 60 (2012) 277–294. doi:10.1016/j.jmps.2011.10.009.

[12] X. Li, Y. Wei, L. Lu, K. Lu, H. Gao, Dislocation nucleation governed softening and maximum strength in nano-twinned metals., Nature. 464 (2010) 877–880. doi:10.1038/nature08929.

[13] Z.X. Wu, Y.W. Zhang, D.J. Srolovitz, Dislocation–twin interaction mechanisms for ultrahigh strength and ductility in nanotwinned metals, Acta Mater. 57 (2009) 4508–4518. doi:10.1016/j.actamat.2009.06.015.

[14] Y.M. Wang, F. Sansoz, T. LaGrange, R.T. Ott, J. Marian, T.W. Barbee, et al., Defective twin boundaries in nanotwinned metals., Nat. Mater. 12 (2013) 697–702. doi:10.1038/nmat3646.

[15] X. Li, Y. Wei, L. Lu, K. Lu, H. Gao, Dislocation nucleation governed softening and maximum strength in nano-twinned metals., Nature. 464 (2010) 877–80. doi:10.1038/nature08929.

[16] L. Sun, X. He, L. Zhu, J. Lu, Two softening stages in nanotwinned Cu, (2014). http://www.tandfonline.com/doi/full/10.1080/14786435.2014.977368#tabModule (accessed January 31, 2015).

[17] H. Zhang, J. Geng, R.T. Ott, M.F. Besser, M.J. Kramer, Effect of Temperature on the Nano/Microstructure and Mechanical Behavior of Nanotwinned Ag Films, Metall. Mater. Trans. A. 46 (2015) 4078–4085. doi:10.1007/s11661-015-3028-8.

[18] D. Bufford, H. Wang, X. Zhang, Thermal stability of twins and strengthening mechanisms in differently oriented epitaxial nanotwinned Ag films, J. Mater. Res. 28 (2013) 1729–1739. doi:10.1557/jmr.2013.50.

[19] J. Bezares, S. Jiao, Y. Liu, D. Bufford, L. Lu, X. Zhang, et al., Indentation of nanotwinned fcc metals: Implications for nanotwin stability, Acta Mater. 60 (2012) 4623–4635. doi:10.1016/j.actamat.2012.03.020.

[20] Z.W. Wang, Y.B. Wang, X.Z. Liao, Y.H. Zhao, E.J. Lavernia, Y.T. Zhu, et al., Influence of stacking fault energy on deformation mechanism and dislocation storage capacity in ultrafine-grained materials, Scr. Mater. 60 (2009) 52–55. doi:10.1016/j.scriptamat.2008.08.032.

[21] A. Hunter, I.J. Beyerlein, Relationship between monolayer stacking faults and twins in nanocrystals, Acta Mater. 88 (2015) 207–217. doi:10.1016/j.actamat.2014.12.045.

[22] L. Cao, A. Hunter, I.J. Beyerlein, M. Koslowski, The role of partial mediated slip during quasi-static deformation of 3D nanocrystalline metals, J. Mech. Phys. Solids. 78 (2015) 415–426. doi:10.1016/j.jmps.2015.02.019.

[23] A. Hunter, I.J. Beyerlein, Stacking fault emission from grain boundaries : Material dependencies and grain size effects, Mater. Sci. Eng. A. 600 (2014) 200–210.

[24] M. Chassagne, M. Legros, D. Rodney, Atomic-scale simulation of screw dislocation/coherent twin boundary interaction in Al, Au, Cu and Ni, Acta Mater. 59 (2011) 1456–1463. doi:10.1016/j.actamat.2010.11.007.

[25] E. Martínez, J. Marian, A. Arsenlis, M. Victoria, J.M. Perlado, Atomistically informed dislocation dynamics in fcc crystals, J. Mech. Phys. Solids. 56 (2008) 869–895. doi:10.1016/j.jmps.2007.06.014.

[26] A. Hunter, R.F. Zhang, I.J. Beyerlein, T.C. Germann, M. Koslowski, Dependence of equilibrium stacking fault width in fcc metals on the $\gamma$ -surface, Model. Simul. Mater. Sci. Eng. 21 (2013) 25015. doi:10.1088/0965-0393/21/2/025015.

[27] A. Hunter, I.J. Beyerlein, T.C. Germann, M. Koslowski, Influence of the stacking fault energy surface on partial dislocations in fcc metals with a three-dimensional phase field dislocations dynamics model, Phys. Rev. B - Condens. Matter Mater. Phys. 84 (2011) 1–10. doi:10.1103/PhysRevB.84.144108.

[28] A. Hunter, F. Saied, C. Le, M. Koslowski, Large-Scale 3D Phase Field Dislocation Dynamics Simulations On High-Performance Architectures, Int. J. High Perform. Comput. Appl. 25 (2011) 223–235. doi:10.1177/1094342010382534.

[29] A Hunter, M. Koslowski, Direct calculations of material parameters for gradient plasticity, J. Mech. Phys. Solids. 56 (2008) 3181–3190. doi:10.1016/j.jmps.2008.08.002.

[30] M. Koslowski, A.M. Cuitiño, M. Ortiz, A phase-field theory of dislocation dynamics, strain hardening and hysteresis in ductile single crystals, J. Mech. Phys. Solids. 50 (2002) 2597–2635. doi:http://dx.doi.org/10.1016/S0022-5096(02)00037-6.

[31] Y. Zeng, A. Hunter, I.J. Beyerlein, M. Koslowski, A phase field dislocation dynamics model for a bicrystal interface system: An investigation into dislocation slip transmission across cube-on-cube interfaces, Int. J. Plast. 79 (2016) 293–313. doi:10.1016/j.ijplas.2015.09.001.

[32] A. Hunter, I.J. Beyerlein, Unprecedented grain size effect on stacking fault width, APL Mater. 1 (2013). doi:10.1063/1.4820427.

Table 1. $w_{max}$ for NT Ag for various twin spacings.

| Grain size (nm) | Twin Boundary Spacing (nm) | $w_{max}$ (nm) |
|---|---|---|
| 36.97 | 4.62 | 1.86 |
| 36.97 | 9.24 | 4.42 |
| 36.97 | 18.88 | 9.53 |
| 36.97 | 27.73 | 15.97 |

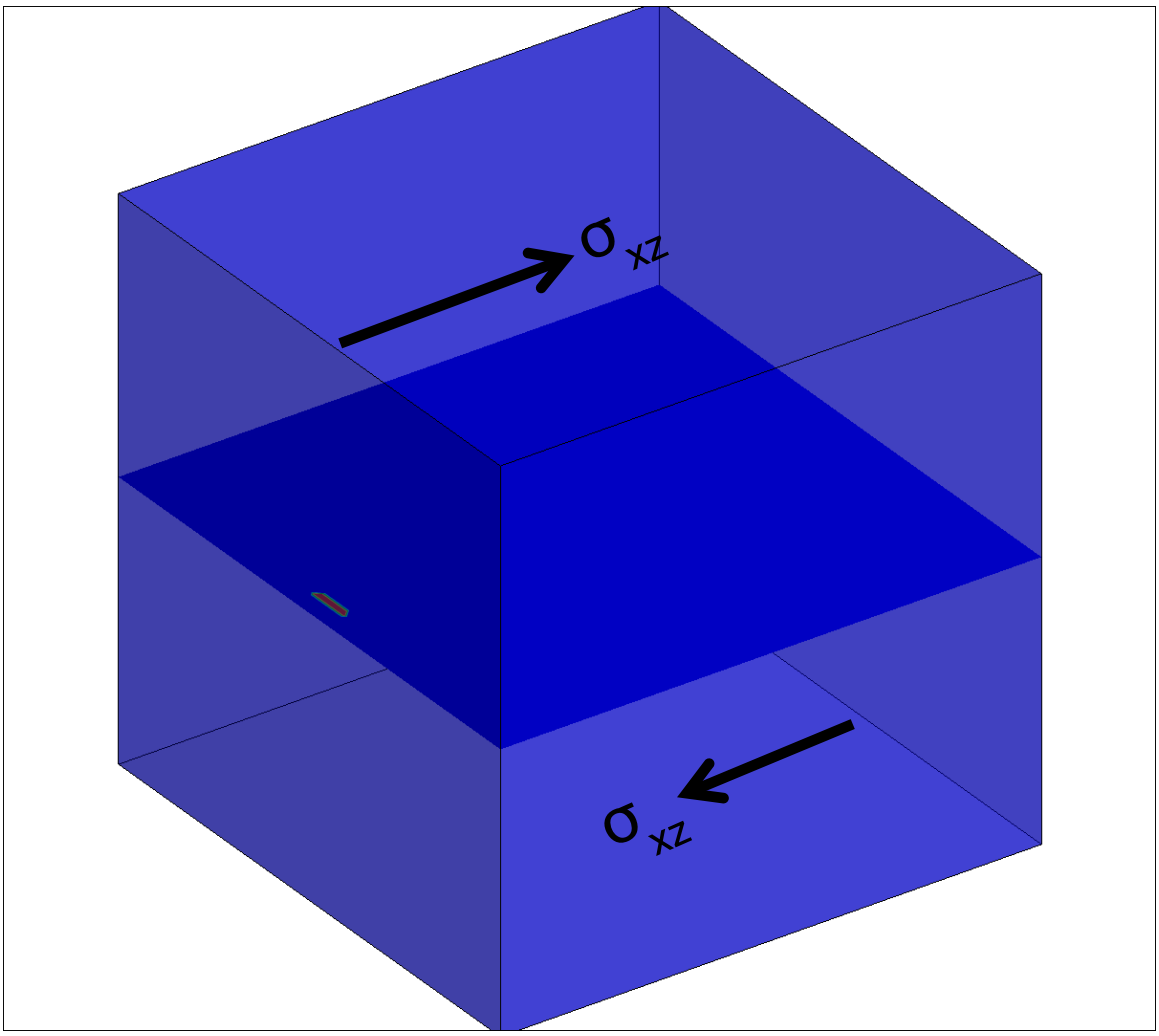


Figure 5.1. Initial configuration of the PFDD simulation cell. Arrows indicating the applied external stress.

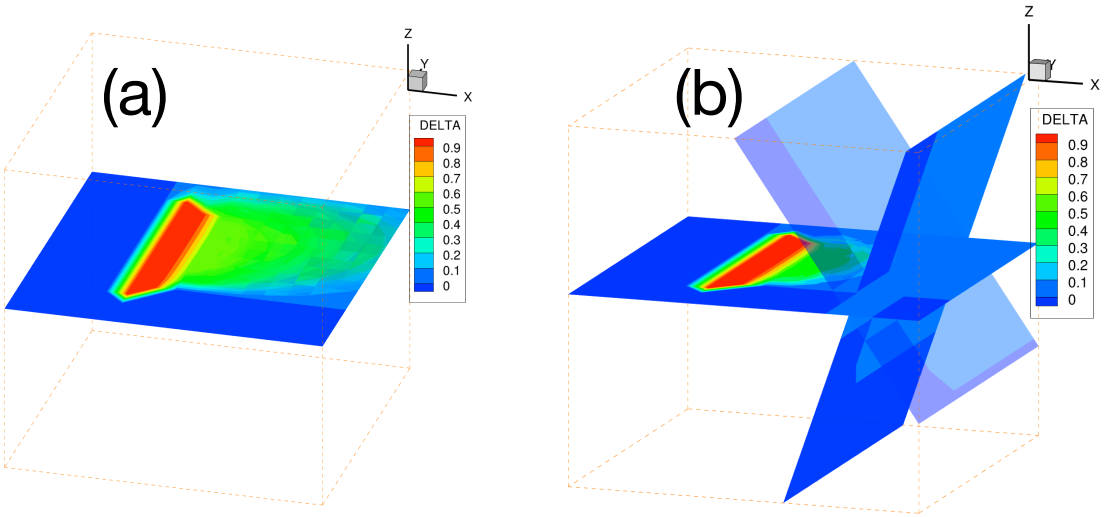


Figure 5.2 Evolution of a partial dislocation in a representative 5 nm grain (a) without, (b) with a twin boundary.

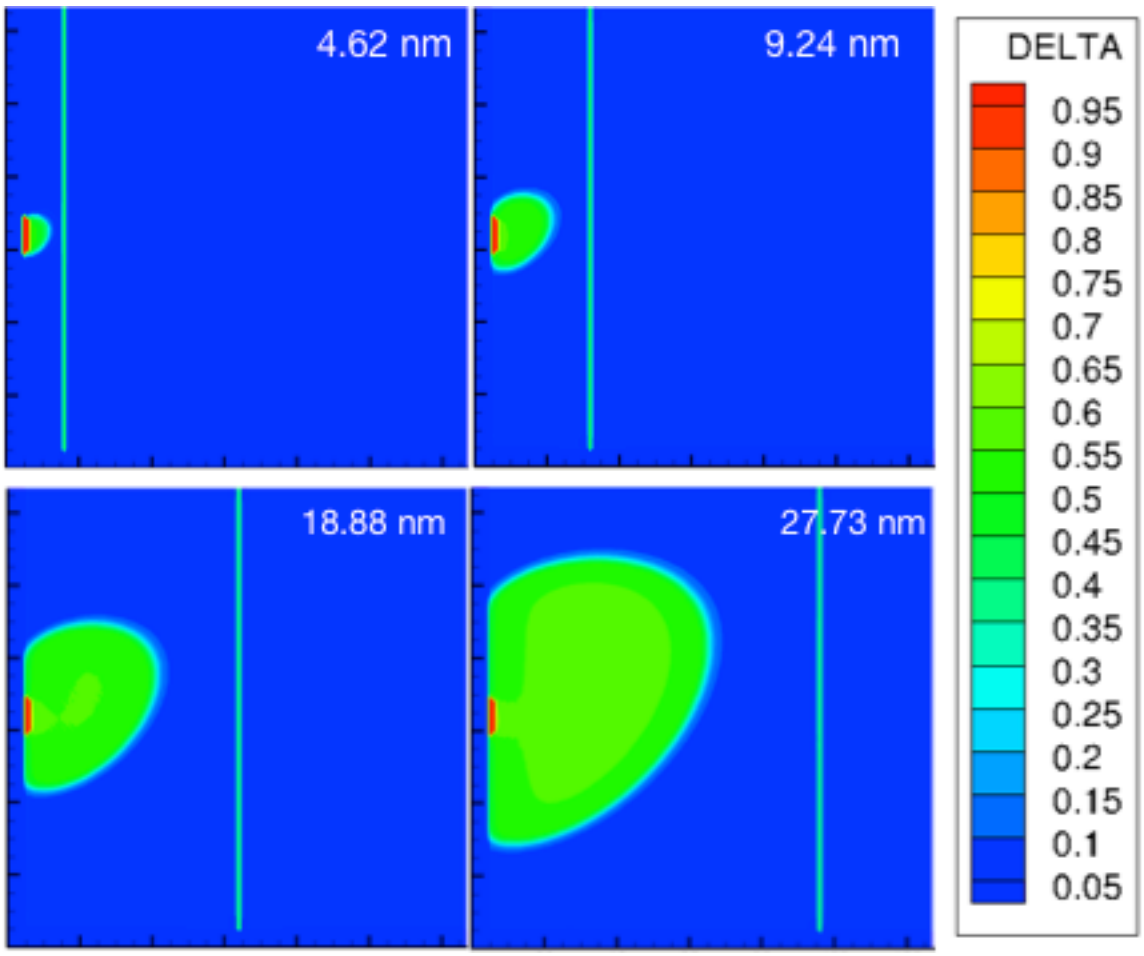


Figure 5.3 Evolution of the extended dislocation structure during the emission of the leading partial dislocation in grains (36.97 nm) with different twin spacing, 4.62 nm, 9.24 nm, 18.88 nm and 27.73nm, respectively.

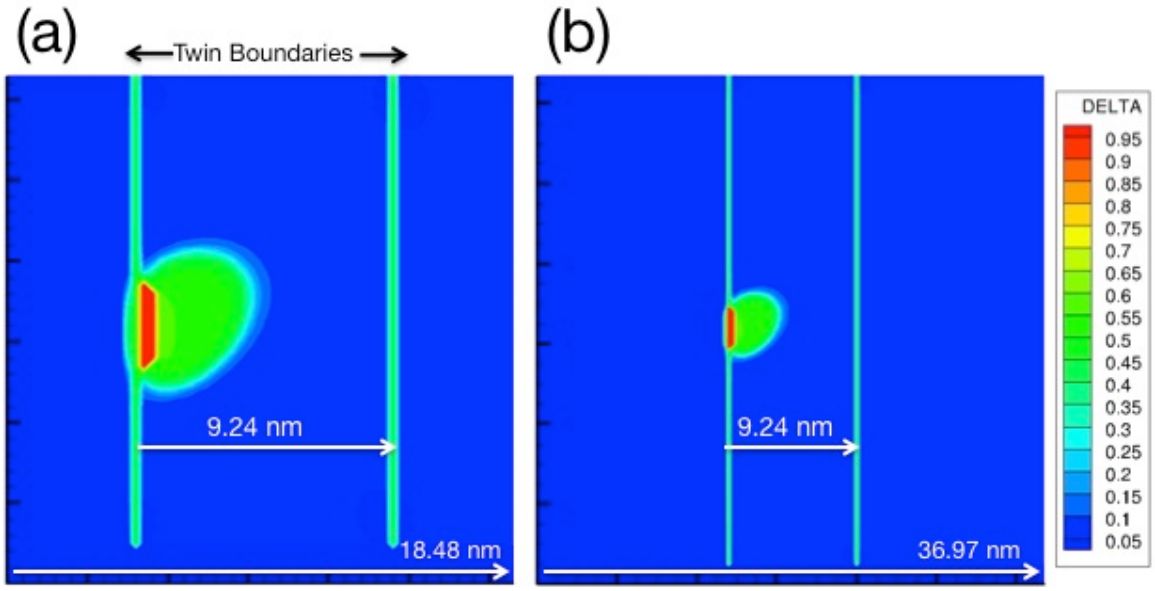


Figure 5.4 Evolution of the leading partial dislocation in a twinned region (a) 18.48 nm, (b) 36.97 nm grain.

# CHAPTER 6. CONCLUSION

Nanotwinned materials show unexpectedly superior mechanical and thermal properties compared to their nanocrystalline counterparts. This thesis addressed the questions regarding the mechanical properties of these materials at various temperatures and aimed to understand their deformation mechanisms by experimental and computational approaches. First, nanotwinned films with different texture parameter and composition were successfully fabricated by magnetron sputtering and the film microstructures were characterized by transmission electron microscopy. *In-situ* high-temperature nanoindentation tests were performed by systematically controlled three fundamental operational parameters: i) stress, ii) strain-rate, and iii) temperature. The films showed strong texture dependence of hardness and thermal stability even after long hours annealing at 400 ˚C. Additionally, it was found that hardness of the films could be increased with Cu-solute addition (2.45 at.%) - approximately 20% higher hardness comparing to the pure nanotwinned silver. To identify the rate-controlling deformation mechanisms, further activation energy and activation volume analyzes were performed. The calculated activation parameters were consistent with the previously reported values of partial dislocation nucleation mediated plasticity. Finally, to better understand the physical phenomena leading to the high strength, we have used the phase field dislocation dynamics (PFDD) model to study the effect of twin boundary spacing, grain size, applied stress on the stress driven emission and interaction of leading/trailing partial dislocations from grain boundary. It was found that twin boundaries impose a backstress that controls the nucleation and motion of the partial dislocation. This thesis has enhanced the

knowledge and understanding of the mechanical properties and deformation behavior of nanotwinned metals at room and elevated temperatures. These metals have shown great potential as a reliable solution for designing strong, ductile and thermally stable metals to be used in many advanced engineering applications.

# APPENDIX. DISSIPATION OF INTERFACIAL STRESS AS SURFACE REORGANIZATION IN METAL THIN FILMS

A modified version of this paper to be submitted to the Nature Materials

Jiahao Chen,[1,2] Ian D. Tevis, [1] Hakan Yavas, Stephanie Oyola-Reynoso,[1] Richard Lesar,[1] Martin M. Thuo[1,2,3]*`

[1]Department of Materials Science & Engineering, Iowa State University, Ames, IA 50011 USA.

[2] Micro-electronics Research Center, Iowa State University, Ames, IA 50011 USA.

[3] Center for bio-plastics and bio-renewables, Iowa State University, Ames, IA 50011 USA.

## Abstract

We report the effect of interfacial stress due to deposition of an adlayer on a host thin metal film. Interfacial stress can increase defects in the host leading to; i) energy dissipation and reorganization to minimize surface energy, ii) increased material hardness. We observed that resultant bimetallic films have reduced surface roughness, and concomitant increase in material hardness, with increasing lattice mismatch between the host and the adlayer. We infer that dissipation of interfacial stress induces defect migration, hence surface reconstruction, leading to lower surface roughness as captured by the surface roughness and grain size. We support our inferences through a combination of empirical and theoretical simulation.

## Introduction

Co-deposited multi-metal thin films have been used in plasmonics [1-3], thermocopules [4], actuation [5], catalysis [6] and materials synthesis [7,8] These applications often assumes that the properties of the first deposited film do not significantly change upon deposition of a second layer, despite the generation of a new interface. Interfacial stress on co-evaporated films, however, is well documented especially in epitaxial film growth [9, 10]. Growth of bimetallic films (hetero-epitaxy) involves deposition of a thin layer of metal ($M_1$) on a host substrate, often silicon (111), followed by the growth or deposition of a second metal ($M_2$) to create three interfaces, *viz*; $M_1$/substrate, $M_1/M_2$, $M_2$/air interfaces. In bimetallic film growth involving non-reactive metals, the strain in the plane of the hetero-interface ($M_1/M_2$) can be estimated from the lattice mismatch, but the magnitude of the shear component of the strain depends on the faceting of $M_1$, inter-diffusion and propensity to reorganize [11-14]. Studies on the resulting strain at the hetero-interface has, however, mostly focused on its effect on the growth/evolution of the $M_2$ film structure with no reports on its effect on the $M_1$/substrate interface [15-20].

We hypothesized that, assuming a perfect lattice at $M_1/M_2$ interface, the morphology of the $M_1$/substrate interface and the bulk properties of $M_1$ film can be affected, and therefore tuned, by misfit stress on the $M_1/M_2$ interface (either as point, $s_z$, or plane, $s_{x-y}$, stress). The misfit stress can lead to either plastic deformation (due to defect migration) or an increase in dislocation (or other defects) density in the material. Increase in dislocations as the material accommodates the resultant strain can lead to a decrease in the grain size on $M_1$ with concomitant decrease in grain boundaries hence

lowering the overall surface energy of $M_1$ along the $M_1$/substrate (Fig. 1a). Plastic deformation due to dislocation migration, however, can also lead to surface step-edge defects, or if the strain predominantly dissipates at high energy points (e.g. grain boundaries and other surface asperities) thermodynamically-favorable reorganization would lead to their annihilation. We hypothesized that plane-stress can be controllably introduced on the surface of a thin film through lattice constant mismatch (misfit stress). Since thin films (lamina) cannot bear significant load in the Z-direction without damage ($s_z \approx 0$) [21. 22] the adlayer ($M_2$) has to be slowly sputtered onto the surface to avoid damage. Template-stripping would subsequently reveal a surface with different surface morphology relative to that of a similar film without the adlayer (Fig. 1b). For a material like Au, with high mobility of atoms at the surface, the proposed reorganization would manifest as a change in surface roughness on the template-stripped film. Increase in defect density would also lead to hardening of the film hence a change in its elastic modulus.

To test our hypothesis, we deposited 200 nm films of Au ($M_1$, lattice constant 407.82 pm) on an ultra-flat Si (100) wafer with its native oxide (substrate). A thin film $M_2$, either Fe (lattice constant 286.65 pm) or Al ($M_2$, lattice constant 404.95 pm), was then sputtered on two different samples. The films were then template-stripped as previously described [23-26] to expose the $M_1$-substrate interface, with or without an adlayer (abbreviated $Au^{M\text{-}TS}$ and $Au^{TS}$ respectively, $m$ = metal making up the adlayer). Characterization of the resultant surfaces by atomic force microscopy (AFM) showed significant differences in surface morphology (Fig. 1c-1e and supporting information Fig. S1a-S1i). The observed root-mean-square roughness ($R_{RMS}$) of the template-stripped

surfaces were; $Au^{TS}$, = 0.39±0.05 nm, $Au^{Al\text{-}TS}$ = 0.44±0.06 nm, $Au^{Fe\text{-}TS}$ = 0.21±0.03 nm. Analysis of the surfaces using scanning electron microscopy (SEM), using the energy selective back scatter (EsB) detector, indicated polycrystallinity with or without the adlayer (supporting information Fig. S1j- S1l). Characterization by X-ray diffraction (XRD) showed that, as expected, the thermodynamically favorable Au (111) orientation was dominant for both $Au^{TS}$ and $Au^{Fe\text{-}TS}$ (Fig. 1f and supporting information Fig S3). A close look at the XRD patterns, however, reveals that the $Au^{Fe\text{-}TS}$ surface get slightly reorganized as capture by the relative decrease in intensity of the (200) and (311) peaks (Fig 1f). We confirmed differences in surface roughness using scanning tunneling microscopy (STM) and found $R_{RMS}$ = 0.22 nm for $Au^{Fe\text{-}TS}$ irrespective of the size of the scanned area (Fig. 1g and supporting information Fig. S2). These results indicate that deposition of the adlayers leads to uniform reorganization of the surface, with concomitant increase ($Au^{Al\text{-}TS}$) or decrease ($Au^{Fe\text{-}TS}$) in surface roughness (as captured by the $R_{RMS}$). The difference in $R_{RMS}$ indicates that the adlayer or the process of depositing $M_2$, had an effect on the $M_1$ film.

*Interfacial stress or kinetic energy transfer*: Since the host Au film is evaporated using e-beam evaporation but the adlayer is deposited using sputtering, we investigated whether the change in deposition technique was the cause of the observed decrease in surface roughness. When 10 nm Au was sputtered onto an e-beam evaporated 200 nm thick Au, the $R_{RMS}$ increased from $Au^{TS}$ = 0.39±0.05 nm to $Au^{Au\text{-}TS}$ = 0.61±0.04 nm (supporting information Fig. S4), suggesting that in absence of misfit stress, as expected, the sputtering process ($s_z$) damages the film.

*Effect of properties of the metal making up the adlayer:* To delineate the origin of the reorganization, several metals – with different chemical (standard redox potentials), solid-state (crystal structures) and surface (lattice parameters) properties were used to create the adlayer. Adlayers of Ti (lattice constant 295.08 pm), Cu (lattice constant 361.49 pm), and, Pd (lattice constant 389.07 pm) were deposited on 200 nm Au films. The reorganized surfaces had $R_{RMS}$ in decreasing order; $Au^{Ti\text{-}TS}$ (0.23±0.01 nm) < $Au^{Cu\text{-}TS}$ (0.26±0.03 nm) < $Au^{Pd\text{-}TS}$ (0.32±0.02 nm), indicating smoother surfaces than the $Au^{TS}$ (Fig. 2a and supporting information Fig. S5 for AFM and Table S1 for comparative summary). We observe that the variation in surface roughness correlates with the identity of the metal and, except for Al, all adlayers gave surfaces with lower $R_{RMS}$ than $Au^{TS}$ (Fig. 2a). We observe that $Au^{TS}$ had the smaller grain areas (0.025 $mm^2$) while $Au^{Al\text{-}TS}$ (0.046 $mm^2$) and $Au^{Fe\text{-}TS}$ (0.052 $mm^2$) had the largest grain areas (Fig. 2b).

*Effect of sputtering rate:* To understand the extent of the influence of $s_z$ we investigated the effect of sputtering rate by depositing Ti adlayers at different rates (0.1, 0.2, 0.3 nm/s) and evaluating the resultant $R_{RMS}$ (Fig. 2c and supporting information Fig. S6). We observed a minima in the mean and variance of surface $R_{RMS}$ (Mean, $\bar{x}_{RMS}$ = 0.23 nm, and standard deviation, $s_{RMS}$, = 0.01 nm) when the sputtering rate was 0.2 nm/s (Fig. 2c). When the deposition rate was less or greater than 0.2 nm/s, the films had higher $R_{RMS}$ (0.29±0.02nm and 0.35±0.03 for 0.08 nm/s and 0.4 nm/s respectively). From these results, we infer that there could be multiple processes occurring simultaneously, resulting in a minimum in roughness at a deposition rate of 0.2 nm/s (Fig. 2c).

*Effect of adlayer thickness:* Having established that the reduction in roughness is dependent on the rate of deposition, the effect of the adlayer thickness was investigated

by sputtering 10-80 nm Ti on 200 nm Au films. Fig. 2d shows that $R_{RMS}$ is more dependent on the rate of metal deposition than on the thickness of the film. When the sputtering rate was set at 0.2 nm/s, slight but statistically insignificant differences in $R_{RMS}$ were observed over different thicknesses (supporting information Fig. S6). We observed the reorganization both on the $M_1$/substrate interface as discussed above, and also on the 'as-deposited' adlayer (supporting information Fig. S7). Correlating the effect of deposition rate and film thickness indicates that evaporating Ti at 0.2 nm/s for a 10 nm thick film is sufficient to achieve maximum reorganization.

*Surface reorganization is independent of location on the wafer*: Since the films are fabricated on an atomically flat Si (111) wafer (with its native oxide), the effect of the position on the wafer was investigated. A sample of $Au^{Fe\text{-}TS}$ from the edge, middle, and, central region of the same wafer was prepared and $R_{RMS}$ measured (**Fig. 2e**). All samples were observed to have similar $R_{RMS}$ values (0.19 ± 0.01 nm) suggesting that the Au film across the whole wafer reorganized evenly on deposition of the adlayer. These results suggest the reported approach to thin film smoothening described here can be used at any scale as long as the material forming the adlayer is uniformly deposited at the same rate across the Au film sitting on an atomically smooth substrate.

*Effect of thermal annealing on $Au^{m\text{-}TS}$:* Thermal annealing creates large grains on metal surfaces albeit with concomitant increase in the size of the grain boundaries – that is; on a large film as grains get larger, the spaces between two large grains increases.[27, 28, 29, 30] Success of thermal annealing depends on several factors, one of which is the quality of the film being annealed.[29, 30] Thermal annealing followed by template-stripping of $Au^{Fe\text{-}TS}$ led to growth of significantly larger grains, with concomitant creation of

atomically flat regions, albeit with increase in the size of the grain boundaries (Fig. 2f). Thermal treatment led to an increase in $R_{RMS}$ from 0.22 nm to 0.68 nm, in part due to increase in the size of grain boundaries. We are, however, aware that differences in the coefficient of thermal expansion, a, between the Fe ($12 \times 10^{-6}$ m/(mk)) and Au ($14.2 \times 10^{-6}$ m/(mk)), may have a major effect on the morphology of the annealed surfaces.

*Simulating the $M_1/M_2$ interface:* Having empirically shown that deposition of another metal on Au leads to significant reorganization of the opposite surface, we desired to understand the mechanism behind this reorganization. The extent of metal penetration upon sputtering can be a source of significant internal stress. We employed Ziegler's SRIM (stopping and range of Ions in Matter) technique[31, 32, 33, 34, 35] to simulate implantation and distribution of the adlayer atoms. The SRIM platform is built on the Bethe-Bloch and Lindhard, Scharff, and Schiott (LSS) theories (as opposed to Tilinin theory).[36, 37] We interpret our simulation results in light of the limitation of this theory, and therefore, these data are not considered in isolation but is used to inform experimental data. We used it to simulate implantation of deposited atoms, ion distribution, and, Kinchin-Pease damage on Au thin films at different kinetic energy of the respective adlayer atoms — assuming that all generated defects are localized (Fig. 3a-3f, and supporting information Fig. S8-S11). For comparison purposes, Fig. 3a-f shows simulation of atom implantation on Au by Fe and Al, metals that gave smoother and rougher surfaces respectively. Fig. 3a and Fig. 3b shows that Al penetrated slightly deeper (peaked at 0.7 nm, Tailed off at 1.4 nm) into the Au film than Fe (peaked at 0.5 nm, tailed off at 1 nm) when the atoms were accelerated at 100 eV — which is significantly larger than would be observed in our sputtering system (~ 400 meV).[38, 39, 40]

For other adlayers, no significant variation in the penetration depth was observed despite differences in atomic properties (supporting information Fig. S9 and Fig. S10). Although the penetration (Fig. 3a and Fig. 3b) and ion/atom range (Fig. 3e and Fig. 3f) seems to be limited according to these simulations, we calculated the recoil energy, which would inform us on the extent of stress due to mechanical implantation of the atoms (Fig. 3c and Fig. 3d). For neutral atoms, however, it is safe to assume that all energy dissipation is localized and only the ensuing strain, or its effect, can propagate into the bulk of the film. Kinchin-Pease damage – due to transfer of energy by an implanted atom/ion into the substrate, leads to point defects near the site of energy transfer.[35, 41, 42, 43] This energy transfer can lead to local atom migration creating a vacancy, or generate Frenkel pairs (vacancy-interstitials pairs) due to secondary recoils at higher energies.[4445] In our case, however, since all atoms have no charge, the number of Frenkel pairs are predicted to be low.[45] Calculating the primary recoil energy, and hence extent of Kinchin-Pease damage across the depth of the substrate film, we observe that Fe gave higher primary recoil energy (7.2 eV) compared to Al (2.4 eV) albeit with a lower propagation depth (Fig. 3c and Fig. 3d). These data concurs with our hypothesis that Kinchin-Pease and Frenkel pair damages will be low in the $Au^{M\text{-}TS}$ films. From these simulation, we observe that there is low penetration of the substrate by the adlayer (≤ 15 %) and there is a low possibility to form Frenkel pairs. Correlation of the simulated data with experiments is, however, needed to further delineate the mechanism of the observed reorganization.

*Experimental characterization of the $M_1/M_2$ interface:* To support the simulation results, X-ray photoelectron spectroscopy (XPS) was used to develop a composition depth profile for the surface by etching small layers and analyzing the elemental composition of the

remaining surface. We adopt this technique acknowledging limitations due to differences in etchability and atomic quantification with XPS. We, however, infer that in a comparative study, obtained data can give insert to the nature of the interface especially when that is in agreement with other techniques. Fig. 3g gives the elemental composition across the thickness of the film for $Au^{Fe\text{-}TS}$. As expected, Fe forms a thin (<15 nm thick) passivating oxide layer upon exposure to ambient conditions. This layer was found to be primarily $Fe_2O_3$ on the surface but rapidly turns into mixed oxides and sub-oxides with depth (Fig 3g). Beneath the oxide layer, the fraction of Fe metal gradually increases to a depth maxima ~ 10 nm then gradually decreases up to ~ 36 nm (Fig. 3g). The general trend in these results concur with our simulations (Fig. 3e vs Fig. 3g), albeit with the oxide layer present in the experimental data and a difference in the degree of interpenetration (2 nm vs ~35 nm respectively). This difference is due to inherent limitations in each method *viz*; i) inability to create atomically smooth interfaces in our experiments, ii) assumption of atomically flat surfaces and an orthogonal deposition of the adlayer in the simulations, iii) presence of defects and polycrystallinity in real material as opposed to the singular faceting and defect free materials in the simulation.

Further depth profiling shows that Au gradually increases and becomes the only element at depths of ~ 35 nm (18 % penetration of the Au film by Fe), indicating small mixing of the two metals at the interface. Similar observations were made for Al, whose penetration is about 18 nm (supporting information). As predicted in Fig. 3a and Fig. 3b, we observed that the penetration of the sputtered adlayer (Fe) into the host substrate (Au) is low (simulation ~15% and experiment ~20%), hence confirming that reorganization is not due to metal interpenetration. Although the small (~20 %) interpenetration can

generate internal stress in the host substrate leading to re-organization. Since the surface of the as-deposited Au prior to deposition of the adlayer is significantly rough (2.3 ± 0.2 nm), the packing of the second metal cannot be expected to form an ultra- smooth interface and, as such, in the depth profile experiment Au will appear to be closer to the surface while Fe will appear to be deeper than would be expected.[46] An asymmetric distribution of Fe is observed both in the simulation (Fig. 3e) and experimental (Fig. 3g) data. Similar observations were made for other metals, even with Al where $R_{RMS}$ for $Au^{Al\text{-}TS} > Au^{TS}$ (Supporting information Figure S12) Comparison of $Au^{Al\text{-}TS}$, $Au^{Fe\text{-}TS}$ and $Au^{TS}$ shows no correlation between penetration depth and changes in $R_{RMS}$ suggesting that the penetration depth is not a significant contributor to the observed reorganization.

To understand the underlying mechanism to the surface reorganization at the $M_1$-substrate interface, the association between Au surface properties and properties of the atoms was investigated. Under the current experimental conditions Au, with its low reactivity, is unlikely to form intermetallic compounds, however, diffusion bonding cannot be ruled out although this is dependent on interatomic forces that are only effective over ~ 1 nm.[47] We therefore sought to investigate other material properties that can help explain the reorganization. Fig. 3h shows the correlation of the $Au^{m\text{-}TS}$ and lattice constant mismatch between the Au and the metal used for the adlayer. We observe that the larger the lattice mismatch the lower the surface roughness, indicating that the lattice constant is an important parameter in tuning degree of surface reorganization. Although a decay is observed, the plot is analogous to that of interfacial stress in hetero-epitaxy film growth in that,[48] it asymptotes at $R_{RMS}$ = 0.2 nm suggesting a maximum limit in reorganization at the interface.

In addition to the simulation and depth profile XPS analysis, we further confirmed the nature of the interface using scanning transmission electron microscopy (STEM).[49] A thin cross-sectional slice of the composite film – supported by a thick Pt layer, was prepared (see supporting information) and, from the STEM image (Fig. 4a), elemental mapping (Fig. 4b) and elemental line analysis (Fig. 4c), we observe that, as predicted by SRIM simulation and XPS, the Fe layer is localized on the surface of Au and does not significantly penetrate into the Au. Through the energy dispersive spectroscopy (EDS) elemental line analysis, the penetration of Fe into Au is estimated about 75 nm. Considering the spatial resolution of EDS and alignment of detector and sample, the actual thickness is expected to be less from the reading. The EDS agrees with XPS depth profile (Fig. 4c and supporting information Fig. S13) when we align EDS at maximum signal with most Fe-rich region from XPS. The effect of the deposited Pt layer can also lead to a slight reorganization at the Fe-Au interface, hence this STEM characterization should be interpreted as a compliment to the simulation and XPS depth profile analysis. The results, even with the limitation in resolution, confirm that the re-organization on the opposite face of the Au film is likely to arise from the interfacial stress generated upon deposition of an adlayer (kinetic energy transfer and associated damage) and from the penetration of the film by atoms making up the adlayer (physical disruption of the crystal lattice).

*Mechanistic understanding of surface reorganization:* We hypothesize that the mechanism of surface reorganization could be a manifestation of thermodynamic equilibration, in which an increase in internal stress due to the introduction of the adlayer leads to surface reorganization and reduced surface energy. This reorganization entails

minimizing the size of the grain and the grain boundaries, a process that induces surface re-organization, albeit on the parallel (opposite) surface of the film from one where the adlayer is deposited. Such a coupled process would require a concomitant increase in defect density upon deposition of the adlayer, followed by dislocation migration leading to dissipation of some of the generated strain. Increased density of defects would consequently lead to an increase in the materials hardness.

To test this hypothesis, we characterized the mechanical properties by nano-indentation.[50, 51, 52] Fig. 5a shows the correlation between the peak load (usually interpreted as the hardness of the material) and surface roughness of the $Au^{M\text{-}TS}$ films. The $Au^{Al\text{-}TS}$ shows comparable hardness with the control sample—$Au^{TS}$, while the rest are harder than the original film. As the material gets harder, the surface roughness decreases following a trend analogous to that observed with the lattice mismatch (Fig. 5b). These results therefore support our hypothesis that there is an increase in defect density upon deposition of the adlayer and, therefore, any associated defect migration leads to the observed reorganization.

In summary, we investigate the effect of interfacial stress in co-deposited metal thin films as captured by surface reorganization, change in mechanical strength, and surface roughness. We hypothesize that the observed changes in thin film properties upon deposition of a second layer is, in part, due to defect migration, that allows for strain relaxation/energy dissipation across the thin film. A minima, in both the mean and standard deviation of $R_{RMS}$ with varying sputtering rates (hence kinetic energy of adlayer atoms), we infer that the reorganization process has an energy barrier to overcome for optimal reorganization. As expected higher sputtering rates (high kinetic energy) led to

film damage. Through nano-indentation, we observe that the thin films became harder which we infer to be due to an increase in defect density. A correlation between hardness, lattice mismatch, and degree of surface reorganization (decrease in roughness) is observed. We, therefore, believe that larger lattice mismatch leads to higher stress and more defects, inducing more surface reorganization, which concomitantly leads to a decrease in size of grain boundaries and, hence, a decrease in surface roughness.

## Methods

*Materials:* All metals were purchased from Ames National Labs or Sigma-Aldrich and were used as received. Some $Au^{m\text{-}TS}$ (m= Fe, Ti, Cu, Pd, Al) substrates were independently custom prepared by Substrata Thin Film Inc. and used as received.

*E-beam evaporation of Au:* 99.99% pure Au was evaporated onto silicon wafer (*Temescal BJD-1800*). Silicon wafers were purchased from university wafer and used as received. The chamber was evacuated to high vacuum ($<10^{-6}$ Torr) before the electron beam was turned on. The evaporation rate was dne at ~1 nm per sec.

*Example of adlayer sputtering procedure (Ti)*: The Ti ad-layer was magnetron-sputtered onto 200 nm Au film on silicon (111) substrates. The chamber was evacuated until the vacuum reached $3x10^{-6}$ Torr. Sputtering was conducted at different rate, where depositing rate was calibrated by measuring thickness of a film using a contact profilometer. The Au ad-layer was sputter coated onto Au-silicon substrates using Quorum sputter coater. The chamber was evacuated and purged with Ar for plenty of times to minimize the amount of air. Deposition rate was estimated as 0.2 nm/s.

*SRIM:* The ion (atoms) penetration into gold film and the energy absorbed by gold film were simulated using the *SRIM software*. The ions were simulated at the given energy of

either 100eV or 10keV. All data and figures were generated automatically by the software.

*Characterization:* The thin film surface was characterized and analyzed by Atomic force microscopy (AFM), Scanning electron microscopy (SEM), Transmission electron microscopy (TEM), X-ray photoelectron microscopy (XPS), X-ray diffraction (XRD) and nano-indetation.

## Acknowledgements

This work was supported by the Iowa State University through start-up funds. MT acknowledges support from a 'Black and Veatch building a world of difference faculty fellowship', MT and JC were supported in part by a Catron fellowship from the Catron Center for Solar Energy Research. The work of HY and RL was supported by the U.S. Department of Energy (DOE), Office of Science, Basic Energy Sciences, Materials Science and Engineering Division through the Ames Laboratory, which is operated for the U.S. DOE by Iowa State University under contract # DE-AC02-07CH11358. We thank Lucas Newcomb and Emma Kwolek for technical assistance. This work was carried in part at the Center for Nanoscale Systems (CNS), a member of the National Nanotechnology Infrastructure Network (NNIN), which is supported by the National Science Foundation under NSF award no. ECS-0335765. CNS is part of Harvard University.

Supporting Information is available online from Nature.com.

## References


1. Sharma, A. K., Gupta, B. On the performance of different bimetallic combinations in surface plasmon resonance based fiber optic sensors. *J. Appl. Phys.* **101**, 093111 (2007).

2. Gupta, B., Sharma, A. K. Sensitivity evaluation of a multi-layered surface plasmon resonance-based fiber optic sensor: a theoretical study. *Sensor Actuat. B* **107**, 40-46 (2005).

3. Ehler, T. T., Noe, L. J. Surface plasmon studies of thin silver/gold bimetallic films. *Langmuir* **11**, 4177-4179 (1995).

4. Varrenti, A. R.*, et al.* Thermal sensing with lithographically patterned bimetallic thin-film thermocouples. *Electron Devic. Lett.* **32**, 818-820 (2011).

5. Randhawa, J. S., Keung, M. D., Tyagi, P., Gracias, D. H. Reversible Actuation of Microstructures by Surface-Chemical Modification of Thin-Film Bilayers. *Adv. Mater.* **22**, 407-410 (2010).

6. Wang, H., Ishihara, S., Ariga, K., Yamauchi, Y. All-metal layer-by-layer films: bimetallic alternate layers with accessible mesopores for enhanced electrocatalysis. *J. Am. Chem. Soc.* **134**, 10819-10821 (2012).

7. Ye, S., Carroll, R. L. Design and fabrication of bimetallic colloidal "Janus" particles. *ACS Applied Materials & Interfaces* **2**, 616-620 (2010).

8. Wadayama, T.*, et al.* Outermost Surface Structures and Oxygen Reduction Reaction Activities of Co/Pt (111) Bimetallic Systems Fabricated Using Molecular Beam Epitaxy. *J. Phys. Chem. C* **115**, 18589-18596 (2011).

9. Hull, R., Stach, E. A. Strain Accommodation and Relief in GeSi/Si Heteroepitaxy. In: *Thin Films: Heteroepitaxial Systems* (Liu WK, Santos, M. B.). World Scientific (1999).

10. Ratsch, C., Ruggerone, P., Scheffler, M. Study of Strain and Temperature Dependence of Metal Epitaxy. In: *Morphological Organization in Epitaxial Growth and Removal* (Zhang Z, Lagally MG). World Scientific (1998).

11. Thurmer, K., Hwang, R. Q., Bartelt, N. C. Surface Self-Organization Caused by Dislocation Networks. *Science* **311**, 1272-1274 (2006).

12. Schmid, A. K., Bartelt, N. C., Hamilton, C. B., Carter, C. B., Hwang, R. Q. Brownian Motion of Dislocations in Thin Films. *Phys. Rev. Lett.* **78**, 3507-3510 (1997).

13. Guo, X., Maier, J. Ionically Conducting Two-Dimensional Heterostructures. *Adv. Mater.* **21**, 2619-2631 (2009).

14. Hong, Y. J., Yang, J. W., Lee, W. H., Ruoff, R. S., Kim, K. S., Fukui, T. Van der Waals Epitaxial Double Heterostructure: InAs/Single-Layer Graphene/InAs. *Adv. Mater.* **25**, 6847-6853 (2013).

15. Cullis, A. G. The morphology and misfit dislocation formation characteristics of strained heteroepitaxial layers: ex situ and in situ growth studies. *Scanning Microsc.* **8**, 957-967 (1994).

16. Fischer, A., Kühne, H., Eichler, M., Holländer, F., Richter, H. Strain and surface phenomena in SiGe structures. *Phys. Rev. B* **54**, 8761 (1996).

17. Harding, J. H., Harker, A. H., Shluger, A. L., Stoneham, A. M. Making connection between atomistic modeling of interfaces and real materials. *Ceramic Microstructures: Control at the Atomic Level, [Proceedings of the International Materials Symposium on Ceramic Microstructures: Control at the Atomic Level], Berkeley, Calif., June* 13-22 (1998).

18. Romanov, A. E.*, et al.* Basal plane misfit dislocations and stress relaxation in III-nitride semipolar heteroepitaxy. *J. Appl. Phys.* **109**, 103522/103521-103522/103512 (2011).

19. Stepanyuk, V. S., Bazhanov, D. I., Baranov, A. N., Hergert, W., Dederichs, P. H., Kirschner, J. Strain relief and island shape evolution in heteroepitaxial metal growth. *Phys. Rev. B* **62**, 15398-15401 (2000).

20. Wu, K-A., Voorhees, P. W. Stress-induced morphological instabilities at the nanoscale examined using the phase field crystal approach. *Phys. Rev. B* **80**, 125408/125401-125408/125408 (2009).

21. Adams, D. F., Carlsson, L. A., Pipes, R. B. *Experimental Characterization of Advanced Composite Materials*. CRC press (2003).

22. Kaw, A. K. *Mechanics of Composite Materials*. CRC press (1997).

23. Weiss, E. A., Kaufman, G. K., Kriebel, J. K., Li, Z., Schalek, R., Whitesides, G. M. Si/SiO2-Templated Formation of Ultraflat Metal Surfaces on Glass, Polymer, and Solder Supports: Their Use as Substrates for Self-Assembled Monolayers. *Langmuir* **23**, 9686-9694 (2007).

24. Chen, J., Wang, Z., Oyola-Reynoso, S., Gathiaka, S. M., Thuo, M. Limits to the Effect of Substrate Roughness or Smoothness on the Odd-Even Effect in Wetting Properties of n-Alkanethiolate Monolayers. *Langmuir* **31**, 7047-7054 (2015).

25. Newcomb, L. B., Tevis, I. D., Atkinson, M. B. J., Gathiaka, S. M. , Luna, R. E., Thuo, M. Odd-Even Effect in the Hydrophobicity of n-Alkanethiolate Self-Assembled Monolayers Depends upon the Roughness of the Substrate and the Orientation of the Terminal Moiety. *Langmuir* **30**, 11985-11992 (2014).

26. Thuo, M. M.*, et al.* Odd-Even Effects in Charge Transport across Self-Assembled Monolayers. *J. Am. Chem. Soc.* **133**, 2962-2975 (2011).

27. Yuan, L., Jiang, L., Zhang, B., Nijhuis, C. A. Dependency of the tunneling decay coefficient in molecular tunneling junctions on the topography of the bottom electrodes. *Angew. Chem., Int. Ed.* **53**, 3377-3381 (2014).

28. Yuan, L., Jiang, L., Thompson, D., Nijhuis, C. A. On the Remarkable Role of Surface Topography of the Bottom Electrodes in Blocking Leakage Currents in Molecular Diodes. *J. Am. Chem. Soc.* **136**, 6554-6557 (2014).

29. De Los Santos, V. L.*, et al.* Crystallization and surface morphology of Au/SiO2 thin films following furnace and flame annealing. *Surf. Sci.* **603**, 2978-2985 (2009).

30. Banner, L. T., Richter, A., Pinkhassik, E. Pinhole-free large-grained atomically smooth Au(111) substrates prepared by flame-annealed template stripping. *Surf. Interface Anal.* **41**, 49-55 (2009).

31. Ziegler, J. F., Ziegler, M. D., Biersack, J. P. SRIM - The stopping and range of ions in matter (2010). *Nucl. Instr. Meth. Phys. Res. B* **268**, 1818-1823 (2010).

32. Ziegler, J. F., Biersack, J. P., Littmark, U. *The Stopping and Ranges of Ions in Matter, Vol. 1: The Stopping and Range of Ions in Solids* (1985).

33. Ziegler, J. F., Editor. *The Stopping and Ranges of Ions in Matter, Vol. 5: Handbook of Stopping Cross Sections for Energetic Ions in all Elements* (1980).

34. Ziegler, J. F. Stopping of energetic light ions in elemental matter. *J. Appl. Phys.* **85**, 1249-1272 (1999).

35. Stoller, R. E., Toloczko, M. B., Was, G. S., Certain, A. G., Dwaraknath, S., Garner, F. A. On the use of SRIM for computing radiation damage exposure. *Nucl. Instr. Meth. Phys. Res. B* **310**, 75-80 (2013).

36. Mangiarotti, A.*, et al.* A survey of energy loss calculations for heavy ions between 1 and 100 keV. *Nucl. Instr. Meth. Phys. Res. A* **580**, 114-117 (2007).

37. Yarkulov, U. Ranges of heavy ions in solids. *Radiat. Eff.* **83**, 233-239 (1984).

38. Berg, S., Nyberg, T., Kubart, T. Reactive Sputter Deposition. In: *Springer Series in Materials Science*. Springer Berlin Heidelberg (2008).

39. Rahmati, A. Reactive magnetron sputter deposition of (Ti,Cu)N nano-crystalline thin films: modeling of particle and energy flux toward the substrate. *Phys. Scr.* **86**, 025301/025301-025301/025310 (2012).

40. Seeger, S., Harbauer, K., Ellmer, K. Ion-energy distributions at a substrate in reactive magnetron sputtering discharges in Ar/H2S from copper, indium, and tungsten targets. *J. Appl. Phys.* **105**, 053305/053301-053305/053308 (2009).

41. Hernandez-Mangas, J. M., Lazaro, J., Enriquez, L., Bailon, L., Barbolla, J., Jaraiz, M. Statistical 3D damage accumulation model for ion implant simulators. *Nucl. Instr. Meth. Phys. Res. B* **202**, 138-142 (2003).

42. Pazsit, I. Interstitial and vacancy distributions in a simple model of radiation damage. *Physica Status Solidi B: Basic Research* **104**, 119-131 (1981).

43. Zhang, Z. L. Revised formula of the average number of Frenkel-pairs. *Radiat. Eff. Defects Solids* **154**, 135-140 (2001).

44. According to Norget's modification of the Kinchin-Pease expression, the energy required to remove an atom from its lattice position, Ed, is directly proportional to the charge, Zm, and mass, m, of the atoms involved in the collision. Based on this model, we infer that with neutral species, the primary recoil energy will be low, hence cannot meet the limit: E<25 KeV.m.Z4/3 needed to generate Frenkel pairs

45. Norgett, M. J., Robinson, M. T., Torrens, I. M. A Proposed Method of Calculating Displacement Dose Rates. *Nucl. Eng. Des.* **33**, 50-54 (1975).

46. Holloway, P. H., Vaidyanathan PN. *Characterization of metals and alloys (Materials characterization series)*. Momentum Press (1993).

47. Ibach, H., Grossmann, A. Surface and interface stress in epitaxial growth. *Mater. Res. Soc. Symp. P.* **440**, 15-24 (1997).

48. Kern, R. Introduction. In: *Stress and Strain in Epitaxy: Theoretical Concepts, Measurements and applications* (J.-P. Deville MH). Elsevier (2001).

49. Brundle, C. R., Evans, C. A., Wilson, S. *Encyclopedia of Materials Characterization: Surfaces, Interfaces, Thin Films*. Butterworth-Heinemann (1992).

50. Chinh, N. Q., Szommer, P., Horita, Z., Langdon, T. G. Experimental Evidence for Grain-Boundary Sliding in Ultrafine-Grained Aluminum Processed by Severe Plastic Deformation. *Adv. Mater.* **18**, 34-39 (2006).

51. Jarausch, K., Kiely, J., Houston, J. E., Russell, P. Defect-dependent elasticity: nanoindentation as a probe of stress state. *J. Mater. Res.* **15**, 1693-1701 (2000).

52. Hosemann, P., Kiener, D., Wang, Y., Maloy, S. A.. Issues to consider using nano indentation on shallow ion beam irradiated materials. *J. Nucl. Mater.* **425**, 136-139 (2012).

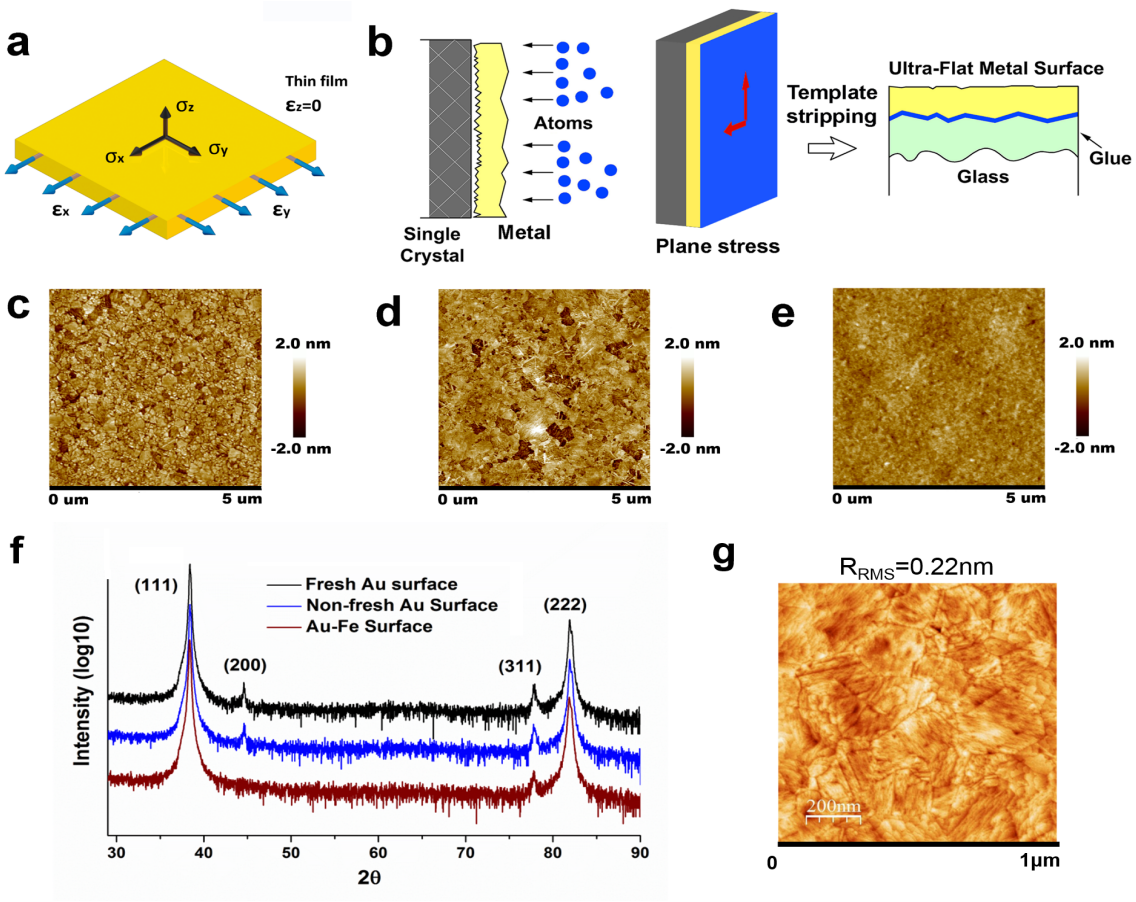


Figure 1. a) Schematic representation of the distribution of stress and strain on a thin film, b) Potential effect of deposition of a second layer of material to generate point stress (Kinetic energy transfer) or plane stress (lattice mismatch) due to interface lattice constant mismatch that leads to improved surface topography upon template stripping. Comparative analysis of resultant surface topography by AFM for; c) $Au^{TS}$ ($R_{RMS}$ 0.39±0.05 nm), d) $Au^{Al\text{-}TS}$ ($R_{RMS}$ 0.44±0.06 nm), and, e) $Au^{Fe\text{-}TS}$ ($R_{RMS}$ 0.21±0.03 nm). f) Normalized XRD patterns for $Au^{TS}$ and $Au^{Fe\text{-}TS}$ indicate surface reorganization as exemplified by diminished intensity in (200) and (311) orientation, g) surface roughness analysis by STM concurs with that derived from AFM for $Au^{Fe\text{-}TS}$.

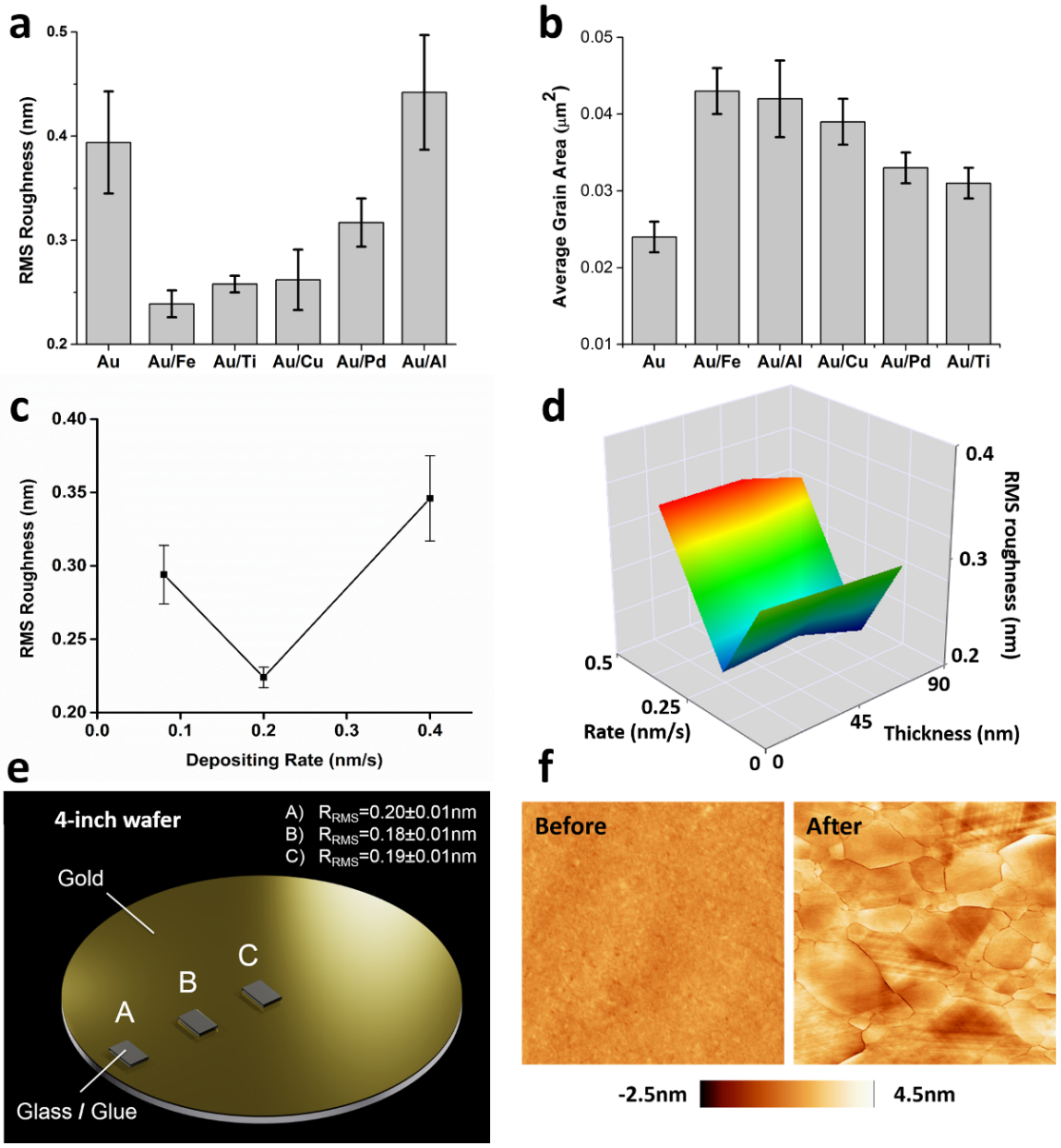


Figure 2. Data derived from multiple samples that were collected randomly from at least three wafers of each surface. a). RMS roughness from all metals, except Al, were lower than those of $Au^{TS}$. b) Average grain areas were larger for all surfaces compared to the $Au^{TS}$. The size of defects, however, were larger for $Au^{Al\text{-}TS}$ while they were very small in $Au^{Fe\text{-}TS}$. c) Analysis of the effect of deposition rate of the adlayer on the $R_{RMS}$ indicated a minima at 0.2 nm/s, while d) comparison of effect of both deposition rate and film thickness shows no statistically significant change in the $R_{RMS}$ with increase in adlayer thickness. e) Sampling different regions of the Si wafer template showed that the surface reorganization occurs evenly across the whole wafer. No significant differences in $R_{RMS}$ were observed irrespective of the region of the wafer sampled. f) Post fabrication thermal annealing of the surfaces leads to an increase in $R_{RMS}$, but with increase in grain boundaries.

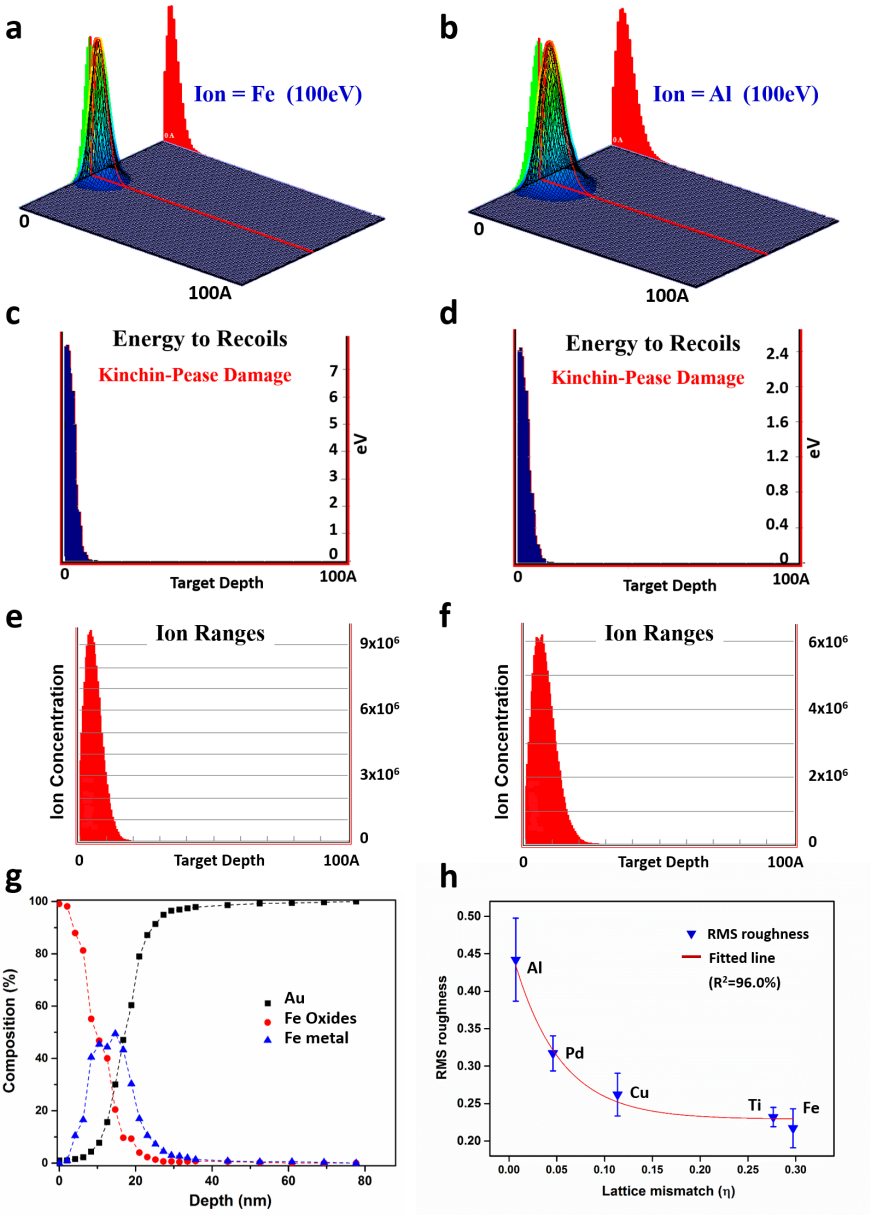


Figure 3. Simulation of interaction of adlayer atoms with Au using the SRIM method. a-b) extent to which deposited atoms penetrate into the Au film albeit at higher energies than expected in a sputter system. c-d) Extent of Kinchin-Pease damage due to primary recoil. Number of Frenken-pairs is predicted to be zero since all elements forming the adlayer have $Z_m = 0$ (no charge). e-f) the ion/atom range showing a penetration depth of ≤. 15 nm. g) Depth profiling of elemental composition of the film using XPS confirms the theoretical predictions and shows little interpenetration. h) The surface roughness correlates well with the differences in lattice parameters (lattice mismatch) between the element making up the adlayer and Au.

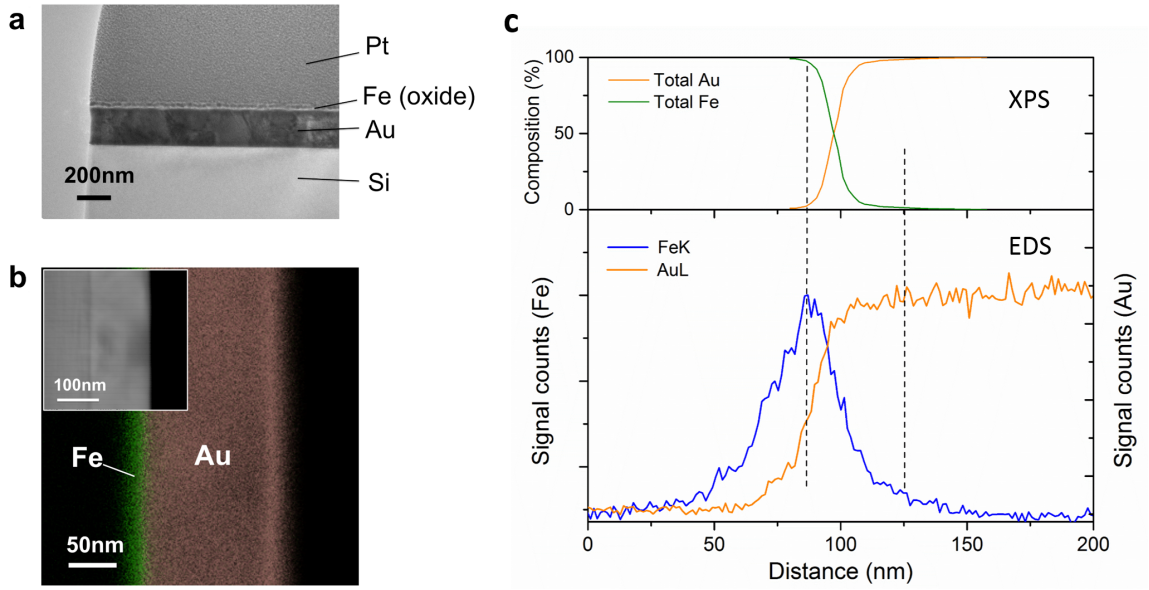


Figure 4. STEM characterization of the as-prepared thin films. a) A thick layer of Pt is deposited on the $Au^{Fe\text{-}TS}$ film and a thin cross-sectional slice, of the three metals and the silicon substrate, is prepared to expose the interfaces. b) Elemental mapping of the Fe-Au interface shows that the adlayer is localized on top of the Au, and does into significantly penetrate or diffuse into the Au film. c) Elemental analysis across the bimetallic interface shows the penetration of Fe into Au layer by both XPS and EDS analysis.

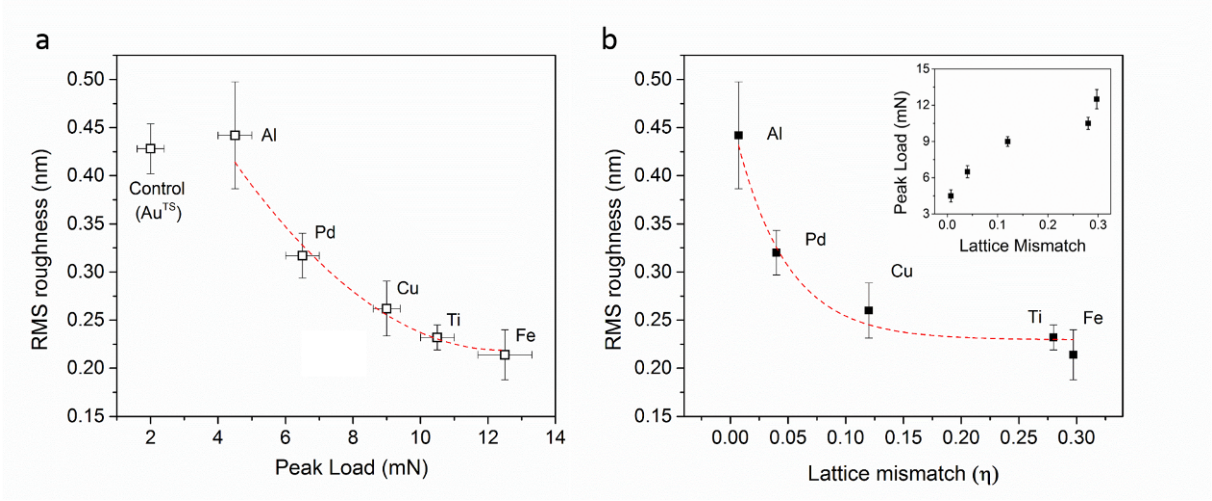


Figure 5. a) The roughness of the template stripped surface is correlated to the mechanical hardness of the material, which is captured by the peak load in nano-indentation. b) The relation between lattice mismatch and the corresponding film surface roughness as well as the peak load (inset). Both peak load and lattice mismatch follow analog relations to the surface roughness.